

**Observation of the Transition from Thomson to Compton
Scattering in Optical Multiphoton Interactions with Electrons**

by

Christopher Ivan Moore

Submitted in Partial Fulfillment

of the

Requirements for the Degree

Doctor of Philosophy

Supervised by

David D. Meyerhofer,

James P. Knauer,

and

Joseph H. Eberly

Department of Physics and Astronomy

The College

Arts and Sciences

University of Rochester

Rochester, New York

1995

CURRICULUM VITAE

The author was born in Detroit, Michigan on March 19, 1966. He attended Clarkson University for his freshman year from the fall semester of 1984 to the spring semester of 1985. He transferred to the University of Rochester in the fall of 1985 and graduated Cum Laude with a Bachelor of Science degree in Physics and Astronomy in 1988. His graduate studies began in the fall of 1988. His research work was performed under the direction of Dr. James P. Knauer and Dr. David D. Meyerhofer at the Laboratory for Laser Energetics.

PUBLICATIONS

- “Observation of the transition from Thomson to Compton scattering in multiphoton interactions with low-energy electrons”, C.I. Moore, J.P. Knauer, D.D. Meyerhofer, *Phys. Rev. Lett.* 74, 2439 (1995).
- “Confinement of electrons to the centre of a laser focus via the ponderomotive potential,” C.I. Moore, *Journal of Modern Optics* 39, 2171-2178 (1992).
- “Theoretical experiments on multiphoton-assisted electron-atom scattering”, R. Grobe, C.I. Moore, Q. Su, W.G. Greenwood, and J.H. Eberly, *Annalen der Physik* 48, 87-96 (1991).
- “Angular distribution of high-order harmonics generated in the tunneling regime”, D.D. Meyerhofer, S. Augst, C.I. Moore, J. Peatross, in *Ultrashort-Wavelength Lasers: SPIE Proceedings 1551*, pp. 246-251, (SPIE, Bellingham, WA, 1991).

- “Spatial distribution of high-order harmonics generated in the tunneling regime,” S. Augst, C.I. Moore, J. Peatross, D.D. Meyerhofer, in *Short Wavelength Coherent Radiation: Generation and Applications*, edited by P. H. Bucksbaum and N. M. Ceglio, 11, pp. 23-27, (OSA, Washington D.C., 1991).
- “Barrier suppression ionization and high-order harmonic generation in noble gases at laser intensities of 1 atomic unit and above,” D.D. Meyerhofer, S. Augst, C. Moore, J. Peatross, J.H. Eberly, and S.L. Chin, in *Multiphoton Processes*, edited by G. Mainfray and P. Agostini, , pp. 317-323, (CEA, Paris, 1990).
- “Tunneling ionization and harmonic generation in Krypton gas using a high-intensity, 1 μm , 1 ps laser”, S. Augst, D.D. Meyerhofer, C.I. Moore, J. Peatross, in *Femtosecond to Nanosecond High-Intensity Lasers and Applications: Proceedings of SPIE 1229*, pp. 152-158, (SPIE, Bellingham, WA, 1990).

ACKNOWLEDGMENTS

I wish to thank Dr. David Meyerhofer and Dr. James Knauer for their excellent guidance during my tenure at the Laboratory for Laser Energetics (LLE). I would also like to thank my academic advisor, Dr. Joseph Eberly, for providing many theoretical insights throughout the course of these experiments, and for his help in the preparation of this thesis.

Among those graduate students in our group at the LLE, I particularly wish to thank: Dr. Steven Augst for sharing much of his knowledge of our laser and vacuum systems; Brian Buerke for being a sounding board for many of my ideas; Yoram Fisher, Lily Li Zheng, and Dr. Justin Peatross for help with the laser system, and Stuart McNaught who measured the electron energy spectrum at 92.5° from \vec{k} .

I am also grateful to the entire staff of the LLE, and would especially like to thank: Richard Fellows for his advice and help during construction of the spectrometer; Dr. Robert Kremens, Dr. Samuel Letzring, and Dr. Paul Jaanimagi for their advice on experimental techniques and troubleshooting; Dr. Oscar Lopez-Raffo for his assistance in a wide range of areas; Giuseppe Raffaele-Addamo for his assistance with electronics, Dr. Robert Keck and Rosemary Leary for their assistance with computer hardware and software, and Richard Whiteman for his help with the 30-mm laser amplifier.

This work was supported by the U.S. Department of Energy Office of Basic Energy Sciences, Division of Chemical Sciences. Additional support was provided by the U.S. Department of Energy Office of Inertial Confinement Fusion under Cooperative Agreement No. DE-FC03-92SF19460, the University of Rochester, and the New York State Energy Research and Development Authority.

ABSTRACT

The energy and angular distribution of electrons ionized from neon and subsequently ejected from a high-intensity optical-frequency laser focus has been measured. The effects of the ionized electrons' interaction with high-intensity optical-frequency radiation are the focus of these studies.

An electron in a relatively low-intensity optical-frequency ($\hbar\omega \sim 1$ eV) plane wave oscillates at the field frequency about a constant average position. The acceleration of the electron during the oscillations causes the electron to radiate at the field frequency in a dipole radiation pattern. This scattering process, known as Thomson scattering in low-frequency fields ($\hbar\omega \ll mc^2$, where mc^2 is the electron's rest energy of 511 keV), becomes Compton scattering as electron recoil becomes important at higher frequencies ($\hbar\omega \sim mc^2$ or greater).

If spatial variations are present in the incident field, the average position of the electron migrates from high- to low-intensity regions. The motion of the electron's average position is the same as the motion of a particle in an effective "ponderomotive" potential. Following ionization in a Gaussian laser focus, the force resulting from the ponderomotive potential causes electron ejection at 90° with respect to the laser \vec{k} if the intensity is relatively low.

At high field intensities, the standard description of Thomson scattering in an optical-frequency field breaks down. As an electron's motion becomes relativistic, Compton-like effects cause the electron to drift in the \vec{k} -direction or recoil. This "high-intensity Compton scattering" results in electron ejection at an angle less than 90° from \vec{k} .

The experiments described in this thesis show a transition from the Thomson regime to the high-intensity Compton scattering regime at high laser intensities. Electrons interacting with relatively low laser intensities are observed at approximately 90° from \vec{k} , as expected. Electrons interacting with high laser intensities are ejected with a significant component of momentum in the \vec{k} -direction (25% of total momentum or 75° from \vec{k}). The observed ejection angles are in excellent agreement with the predictions of high-intensity Compton scattering.

TABLE OF CONTENTS

CHAPTER 1: INTRODUCTION	1
References	11
CHAPTER 2: RELATIVISTIC ELECTRON TRAJECTORIES IN A HIGH-INTENSITY PLANE WAVE	14
2.1 Electron's equation of motion in a high-intensity plane wave	15
2.2 Electron trajectories in linear and circular polarization	20
2.3 The longitudinal drift	31
References	36
CHAPTER 3: SPATIAL AND TEMPORAL EFFECTS IN A LASER FOCUS	40
3.1 The ponderomotive potential	40
3.2 Electron ejection from a low-intensity laser focus	46
3.3 Electron ejection from a high-intensity laser focus	51
3.4 The effects of a time-dependent pulse	52
References	56
CHAPTER 4: NUMERICAL SIMULATION OF ELECTRON DYNAMICS IN A FOCUSED LASER FIELD	59
4.1 The paraxial approximation for a Gaussian laser focus	60
4.2 The longitudinal field of a Gaussian focus	62
4.3 Monte Carlo simulation of electron ejection from a high- intensity, Gaussian laser focus	63
References	76

CHAPTER 5: EXPERIMENTAL SETUP	77
5.1 Laser system	77
5.2 Magnetic electron spectrometer	83
5.3 The energy calibration of the spectrometer	101
5.4 Measurement of the angular distribution of the electrons	105
5.5 Energy spectrum of helium	108
References	111
CHAPTER 6: EXPERIMENTAL OBSERVATIONS OF THE ELECTRON DISTRIBUTIONS	112
6.1 Acquisition	112
6.2 Analysis	113
6.3 The observed angular distributions of electrons ejected from neon	123
References	126
CHAPTER 7: CONCLUSIONS	127
APPENDIX A: MONTE CARLO SIMULATION PROGRAM OF ELECTRON TRAJECTORIES IN A LASER FOCUS	131
APPENDIX B: SCHEMATICS OF THE MAGNETIC ELECTRON SPECTROMETER	141
APPENDIX C: COMPUTER CODE FOR PROPAGATION OF ELECTRONS THROUGH THE SPECTROMETER	145
APPENDIX D: ENERGY SPECTRA OF NEON AS A FUNCTION OF THE ANGLE FROM THE BEAM AXIS	152
APPENDIX E: ANGULAR DISTRIBUTIONS OF ELECTRONS FROM NEON RELATIVE TO THE LASER BEAM AXIS	157

LIST OF TABLES

Table 1	Ionization potentials, E_{ion} , BSI threshold intensities, I_{th} in lin., and ejection energies, E_{lin} , for laser pulses much longer than τ_{lin} in linear polarization.	66
Table 2	Ionization potentials, E_{ion} , BSI threshold intensities, I_{th} in circ., and ejection energies, E_{circ} , in laser pulses much longer than τ_{circ} in circular polarization.	66
Table 3	Ionization threshold intensities, I_{thresh} , and expected ejection energies, $2\Phi_p$, of the neon charge states studied in the experiments.	118
Table 4	A table of the expected and observed energies and widths of the electron peaks for neon...	122
Table 5	Predicted BSI threshold intensities in circular polarization, $I_{\text{thresh}}(\text{Circ.})$, electron ejection energies, $2\Phi_p$, and ejection angle from \vec{k} , θ_{eject} , of a few charge states of Krypton...	129

LIST OF FIGURES

- | | | |
|-------|---|----|
| 1.1 | A high-frequency photon ($\hbar\omega_2 \sim mc^2$ or greater) scatters from an electron via Compton scattering. The photon's high frequency and corresponding large momentum requires the electron recoil to conserve energy and momentum following the scattering. | 2 |
| 1.2 | The Kapitza-Dirac effect. A particle with initial momentum \vec{p}_0 is incident on a standing light wave. Virtual absorption and stimulated emission of photons between the counter-propagating traveling waves of the standing wave causes a momentum transfer to the particle in units of $2\hbar k$. | 4 |
| 1.3 | An electron travels towards the center of a laser beam with a Gaussian intensity profile. The intensity distribution in a plane perpendicular to the field's propagation direction (the z-direction) is shown on the right. The ponderomotive potential deflects the electron from the intense central portions of the field. | 6 |
| 1.4 | The kinetic energy of electrons versus their angle from \vec{k} following ejection from the laser focus. A forward component of the electrons' momentum that "pushes" the electrons toward \vec{k} is evident... | 9 |
| 2.2.1 | A conceptual picture of tunneling ionization. The normal Coulomb potential (left) is distorted by the addition of the electric field of the laser (right). The electron can tunnel through the Coulomb barrier and ionize from the atom (or ion). | 22 |
| 2.2.2 | Coulomb barrier suppression ionization (BSI). The left figure shows an electron in a bound state of the Coulomb potential. The right figure shows the distortion of the potential when an electric field is added... | 22 |
| 2.2.3 | The "figure-8" motion of an electron oscillating in a high-intensity linearly polarized field in the electron's average rest frame. The axes are in units of the inverse of the wave number. | 26 |
| 2.2.4 | A highly relativistic electron trajectory, $q=100$. Both axes are in units of the inverse of the wave number. The maximum amplitude of the oscillations in z is given by $k z - v_d t < 1/2$ while the amplitude of the oscillation in x is much larger... | 27 |

2.2.5	An electron's trajectory in its average rest frame in circular polarization for varying values of q . All axes are in units of the inverse of the wave number...	30
3.1.1	An example of the effects of the ponderomotive potential. Darker regions represent higher intensities. A beam of electrons (arrows) is scattered by the high-intensity light at the focus of a high-power laser beam.	45
3.2.1	The canonical drift is approximately radial far from the laser focus. The difference between the radial and actual trajectory is greatly exaggerated in this picture.	49
3.3.1	The definition of the angle θ .	52
4.3.1	The Monte Carlo simulation of the ionization of neon with a linearly polarized laser of peak intensity $I=10^{18}$ W/cm ² . (a) The energy spectrum for a long pulse (1-ns FWHM). (b) The energy spectrum for a short pulse (50-fs FWHM).	68
4.3.2	The Monte Carlo simulation of the ionization of neon with a circularly polarized laser of peak intensity 10^{18} W/cm ² . (a) The energy spectrum for a long pulse (1-ns FWHM). (b) The energy spectrum for a short pulse (50-fsec).	70
4.3.3	The Monte Carlo simulation of the ionization of neon with a laser of peak intensity 10^{18} W/cm ² and a pulse width of 1.5 psec. (a) The energy spectrum for linear polarization. (b) The energy spectrum for circular polarization.	73
4.3.4	The angular distribution of Ne ¹⁺ electrons ejected with 186 eV of energy. The solid line is the Monte Carlo simulation prediction for the angular distribution. The dashed line is the angle of ejection calculated with equation (3.3.3) using an energy of 186 eV ($\gamma = 1.000364$).	74
4.3.5	The angular distribution of Ne ⁸⁺ electrons ejected with 84.2 keV of energy. The solid line is the Monte Carlo prediction of the ejected electron distribution. The dashed line is the angle of ejection calculated using equation (3.3.3) and the ejected energy of 84.2 keV ($\gamma = 1.165$).	75
5.0.1	The general layout of the experiment.	77

5.1.1	The Nd:YLF/Glass CPA laser system used for generation of approximately 1 TW pulses.	78
5.1.2	A glass wedge extracts 2% of the incident laser for energy and pulse width measurements.	79
5.1.3	The temporal intensity distribution of the laser pulse.	79
5.1.4	The near-field intensity distribution of the laser. On the left is a contour plot of the laser's intensity distribution. On the right is the intensity distribution along the dashed line in the contour plot.	80
5.1.5	The far-field intensity distribution of the laser. On the left is the laser's intensity distribution. On the right is the intensity profile along the dashed line.	81
5.2.1	The magnetic spectrometer layout. A few electrons ejected from the laser focus enter the gap of the magnet in the spectrometer. The electrons are curved by the magnet field in the gap of the magnet...	84
5.2.2	Trajectory of the electron through the magnet gap for a constant magnetic field within the gap. The direction of \vec{p}_{initial} and \vec{p}_{final} required for propagation from the focus to the scintillator are fixed by the geometry of the spectrometer and its position relative to the focus...	85
5.2.3	The magnetic flux lines of the c-shaped magnet in the spectrometer. The dark region is the iron core of the magnet. The high permeability ($\mu \sim 1000\mu_0$) of the iron confines 97% of the magnetic field to the magnetic circuit created by the iron and the gap. 3% of the magnetic flux leaks from the iron through the hollow center of the magnet.	86
5.2.4	The "hysteresis" loop of the magnet in the spectrometer before degaussing the iron core. The arrows represent the direction the loop was generated.	88
5.2.5	Effect of a slowly decaying sinusoidal current on the magnetic field of a solenoid with a ferromagnetic core. The time dependence of the current is shown in the inset.	89
5.2.6	A circuit for degaussing magnetic materials.	90

5.2.7	Temperature versus resistance curve for a typical PTC thermistor.	90
5.2.8	Circuit diagram of the power supply to fire and degauss the magnet in the electron spectrometer.	91
5.2.9	The magnetic field generated in the gap of the magnet as a function of current through the coil after degaussing. Six measurements were taken at a series of current settings...	92
5.2.10	The measured relative strength of the magnetic field as a function of position. The two scans are through the center of the gap along perpendicular axis as shown in the inset of the top figure...	97
5.3.1	Calibration of the magnetic electron spectrometer. The electron gun is centered on the laser focus and aimed toward the gap in the magnet of the spectrometer. The lower picture shows the production of secondary electrons from the collision of the ions with the cathode.	102
5.3.2	A scan of the spectrometer magnetic field to determine the window of field strengths that allow propagation of 15 keV electrons from the electron gun to the scintillator.	103
5.3.3	Plots of the kinetic energy of electrons observed versus the magnetic field within the gap of the magnet of the magnetic spectrometer...	104
5.3.4	A scan of the scintillation photon signal as a function of energy for approximately monoenergetic electrons. The scan shows a resolution of $\Delta E/E \approx 30\%$.	105
5.4.1	The angular distribution is measured by rotating the entire spectrometer. ϕ is the angle of rotation of the spectrometer. θ is the angle between an electron trajectory from the laser focus to the gap and the laser axis.	107
5.4.2	The angular distributions of 4 keV electrons from Nitrogen on opposite sides of the laser focus.	108
5.4.3	The asymmetry in the angular distribution of electrons due to the response of the spectrometer. The spectrometer rotates electrons 5.7° in ϕ from their original angle and the electrons can be considered released relative to an effective beam axis.	108

- 5.5.1 The energy spectrum of helium at 85.0° from the beam axis. The inset shows the measured spectrum out to 40 keV. The only peak is at 3.0 keV. These are from electrons freed in creating He^{2+} . The observed energy is slightly lower than the Monte Carlo simulation prediction of 3.4 keV (the dashed curve). 110
- 6.2.1 Intensity scan of 3 keV electrons ejected from neon. The signal as a function of intensity behaves as $I^{1.8 \pm 0.2}$. This is used to normalize the signal levels for the 5 shots taken at each energy to the corresponding signal at a single intensity (10^{18} W/cm^2). 114
- 6.2.2 The size of the focal volume of a Gaussian laser profile as a function of the ratio of the threshold intensity to the peak intensity of the laser pulse. For $I_{\text{th}} < 0.4I_0$, the functional dependence of the focal volume is closely approximated by $(I_{\text{th}}/I_0)^{3/2}$. 117
- 6.2.3 The energy distribution of the electrons ejected from neon at 87.3° from \vec{k} . Three distinct peaks corresponding to Ne^{3+} , Ne^{4+} , and Ne^{5+} are shown by the positions of the arrows. The cross hatched area below 2 keV is not measurable with the spectrometer. 119
- 6.2.4 The energy spectrum of neon at 75.8° from \vec{k} . The peak at approximately 67 keV is a sum of the contributions from the electrons of Ne^{7+} and Ne^{8+} . 120
- 6.2.5 The energy spectrum of neon at 78.8° from \vec{k} . The peak at approximately 60 keV is almost entirely electrons from Ne^{7+} . This allows determination of the energy and width of the peak from the Ne^{7+} electrons. 121
- 6.2.6 The energy spectrum of neon at 69.9° from \vec{k} . The peak at approximately 85 keV is almost entirely electrons from Ne^{8+} . This allows determination of the energy and width of the peak from the Ne^{8+} electrons. 121
- 6.3.1 The angular distribution of the 3.1 keV electrons from Ne^{3+} . The solid curve is a Gaussian curve fit to the experimental data. The dashed line is the angle predicted using equation (6.3.1) and $\gamma = E/mc^2 + 1 = 1.0059$. 124

- 6.3.2 The angular distribution of the 84 keV electrons from Ne^{8+} . The solid curve is a Gaussian curve fit to the experimental data. The dashed line is the angle predicted using equation (6.3.1) and $\gamma = E/mc^2 + 1 = 1.16$. 125
- 6.3.3 The energy of electrons ejected from the focus versus the angle of the peak of the electron angular distribution. The open circles are the experimental data. The solid circles are the Monte Carlo predictions. The solid line is the angle versus energy relation of equation (6.3.1). 126
- 7.1 The energies of electrons from Ne^{3+} to Ne^{8+} in circular polarization. The open circles are the predicted energies (twice the ponderomotive potential of the BSI threshold intensities) and the solid circles are the observed energies. 128

Chapter 1

Introduction

The scattering of electromagnetic radiation from electrons has historically been divided into the low-frequency ($\hbar\omega \ll mc^2$) Thomson scattering and the high-frequency ($\hbar\omega \gg mc^2$) Compton scattering regimes.

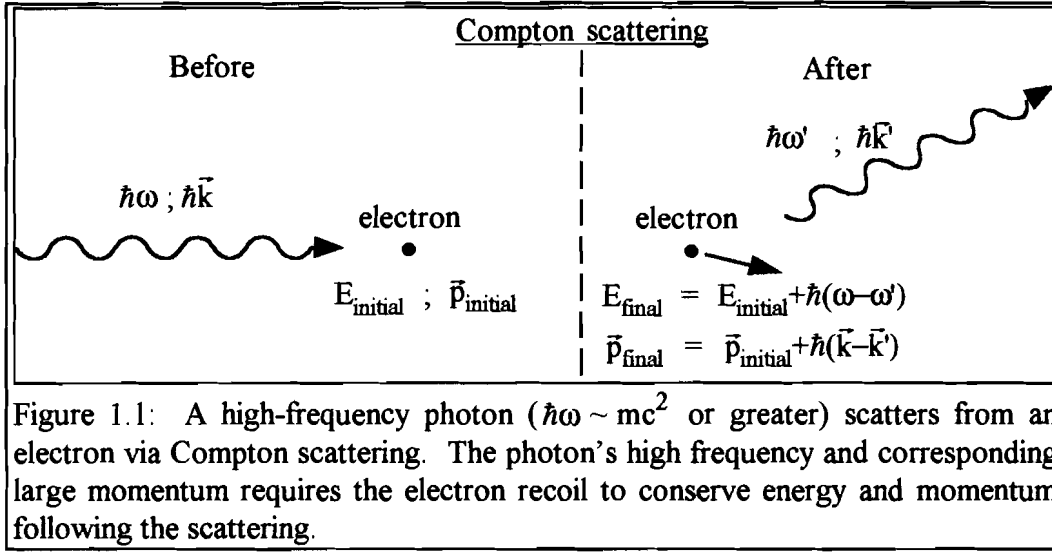
In Thomson scattering, a classical electric field accelerates an electron via the nonrelativistic Lorentz force equation,

$$m\dot{\vec{v}} = -e\vec{E}(\vec{r}, t) = -e\hat{\epsilon}_{\text{in}}E_0 \cos(\vec{k} \cdot \vec{r} - \omega t), \quad (1.1)$$

where m and e are the electron's charge and mass respectively, $\hat{\epsilon}_{\text{in}}$ is the polarization state of the scattered radiation, and the dot represents differentiation with respect to time. The radiation distribution from this charged particle acceleration is described by the Thomson scattering cross-section,¹

$$\frac{d\sigma}{d\Omega} = \left(\frac{e^2}{mc^2} \right)^2 \left| \hat{\epsilon}_{\text{in}}^* \cdot \hat{\epsilon}_{\text{out}} \right|^2, \quad (1.2)$$

where $\hat{\epsilon}_{\text{out}}$ is the polarization state of the scattered radiation and $*$ denotes the complex conjugate. The absence of the $\vec{v} \times \vec{B}$ magnetic field term from (1.1) means the electron suffers no recoil in the \vec{k} direction.



Compton scattering is said to take place when the frequency of the radiation field is high enough to make the electron velocity near-relativistic. Then the $\vec{v} \times \vec{B}$ term must be included in (1.1) and the electron does experience recoil in the \vec{k} direction. It is more common to adopt a particle picture for the high-frequency Compton photon (see Figure 1.1) and to use quantum field theory to describe the interaction. The scattering cross-section is given by the Klein-Nishina formula,¹

$$\frac{d\sigma}{d\Omega} = \left(\frac{e^2}{mc^2}\right)^2 \left(\frac{k_{\text{out}}}{k_{\text{in}}}\right)^2 \left(\left| \hat{\epsilon}_{\text{in}}^* \hat{\epsilon}_{\text{out}} \right|^2 + \frac{\hbar\omega}{4mc^2} (1 - \cos\theta) \right), \quad (1.3)$$

where θ is the angle between the incident (\vec{k}_{in}) and scattered (\vec{k}_{out}) photon wave vectors and $k_{\text{out}}/k_{\text{in}}$ is given by the Compton formula

$$\frac{k_{\text{out}}}{k_{\text{in}}} = \frac{1}{1 + \frac{\hbar\omega}{mc^2} (1 - \cos\theta)}. \quad (1.4)$$

The factor $k_{\text{out}}/k_{\text{in}}$ is a kinematical factor required to conserve energy and momentum when the electron recoils. The second term on the right side of equation (1.3) results from scattering by the electron's magnetic moment. The Compton scattering cross section obviously reduces to the Thomson scattering cross-section for low-energy photons ($\hbar\omega \ll mc^2$).

An optical photon's low-energy (~ 1 eV) compared to the electron's rest energy (511 keV) normally allows a Thomson scattering description of the interaction. However, there exist at least two situations at optical frequencies where the Thomson scattering description is insufficient and the electron's recoil due to Compton-like effects must be considered.

The first is the scattering of particles from a standing light wave. This is known as the Kapitza-Dirac effect.² A standing light wave consists of two counter-propagating traveling waves. Virtual absorption of one traveling wave's photons by a particle and stimulated emission into the counter-propagating wave causes a net momentum transfer to the particle of $2n\hbar\vec{k}$, where \vec{k} is the wave vector of the traveling wave and n is an integer that represents the possibility of multiple photon scatterings. Particles incident on a standing wave therefore gain even-integer multiples of the photon momentum and scatter from the standing wave (see Figure 1.2). Early attempts to observe the Kapitza-Dirac effect with electrons were inconclusive.³⁻⁵ Reproducible observations were first obtained using atoms.^{6,7} The recent availability

of low-energy electron beams, obtained by multiphoton ionization, has permitted a corresponding experiment with electrons.⁸

The second situation in which electron recoil is significant at optical frequencies is so-called high-intensity Compton scattering.⁹⁻¹⁶ High-intensity Compton scattering occurs when the electron's motion becomes relativistic and the $\vec{v} \times \vec{B}$ term in the Lorentz force must be considered. The $\vec{v} \times \vec{B}$ term causes the electron

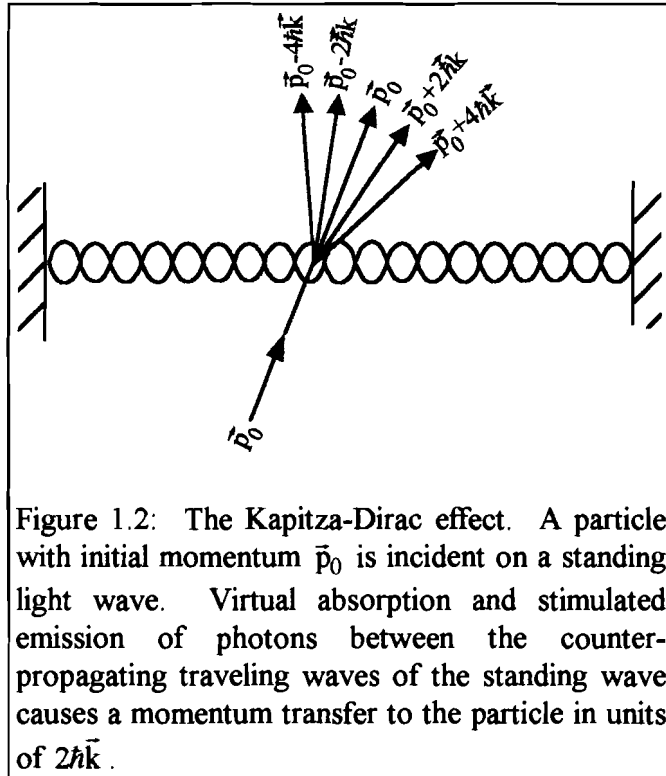


Figure 1.2: The Kapitza-Dirac effect. A particle with initial momentum \vec{p}_0 is incident on a standing light wave. Virtual absorption and stimulated emission of photons between the counter-propagating traveling waves of the standing wave causes a momentum transfer to the particle in units of $2\hbar\vec{k}$.

to drift in the \vec{k} direction (what will sometimes be called the longitudinal direction). The electron's longitudinal motion in an ultra-high-intensity optical field will be shown to be analogous to the Compton scattering recoil of an electron by a high-frequency photon in chapter 2.

High-intensity Compton scattering only results from single electron interactions with the field. Interaction of the electron with other particles in the presence of the field obviously destroys the simple picture of a free electron oscillating

in an electromagnetic field. The density of electrons and other particles must therefore be low enough to ensure the electron interacts with no other particles during its interaction with the photons. This was the case in the experiments described in this thesis.

Brown and Kibble⁹ predicted that an electron's longitudinal drift in a high-intensity field will result in a Doppler shift or an intensity-dependent frequency shift in the scattered radiation. Many papers were published on high-intensity Compton scattering,⁹⁻¹⁶ and an experiment was proposed¹³ to observe the frequency shift. To this author's knowledge, the frequency shift and drift were never experimentally observed.

The first measurements of longitudinal electron drift due to high-intensity scattering at optical wavelengths are presented in this thesis. Observation of the drift confirms the existence of electron recoil due to high-intensity scattering. The frequency shift in the scattered radiation has not been observed. To understand how this drift manifests itself in a high-intensity laser focus, we must first discuss the ponderomotive potential.

The ponderomotive potential is an effective potential experienced by charged particles in an electromagnetic field with a spatially varying intensity distribution. Spatial variation of the field causes a migration of charged particles from high- to low-

intensity regions. The motion of a particle's average position is described by the equation of motion,

$$m\ddot{\vec{r}} = -\vec{\nabla}\Phi_p \quad (1.5)$$

where Φ_p is the ponderomotive potential, given by

$$\Phi_p = \frac{q^2 \langle \vec{E}^2 \rangle}{2m\omega^2} = \frac{q^2 I \lambda^2}{2\pi m c^3}. \quad (1.6)$$

Here $\langle \vec{E}^2 \rangle$ is the time-averaged square of the electric field and $I = c \langle \vec{E}^2 \rangle / 4\pi$ is the field intensity. Clearly, Φ_p is only dependent on the spatial distribution of the intensity. As a result, the average motion of the charged particle is independent of field polarization. An example of an electron scattering from the ponderomotive potential is shown in Figure 1.3. Boot and Harvie discovered the ponderomotive potential in 1957^{17,18} when they theoretically predicted and confirmed its effects in 10-

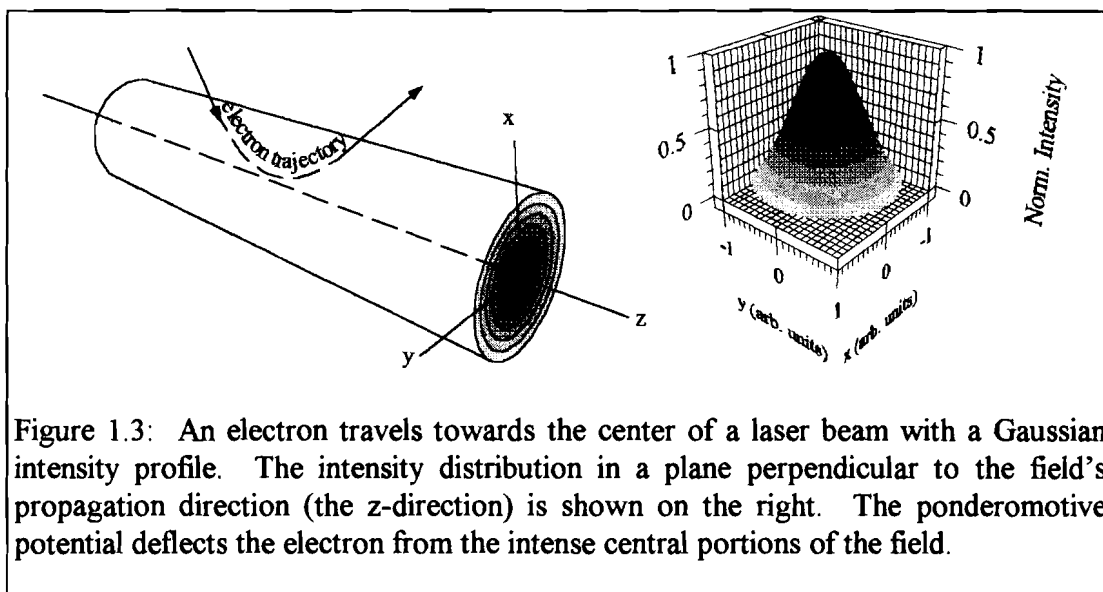


Figure 1.3: An electron travels towards the center of a laser beam with a Gaussian intensity profile. The intensity distribution in a plane perpendicular to the field's propagation direction (the z-direction) is shown on the right. The ponderomotive potential deflects the electron from the intense central portions of the field.

cm radiation in a magnetron.¹⁷ Further theoretical developments and understanding of the ponderomotive potential were given by Kibble and others.¹⁹⁻²²

The λ^2 wavelength dependence of the ponderomotive potential causes long-wavelength fields to exhibit stronger ponderomotive potentials than short-wavelength fields of the same intensity. For example, the 10-cm field used by Boot and Harvie had a ponderomotive potential 10^{10} times larger than a 1-micron field of the same intensity. The recent availability of high-intensity lasers allows the observation of ponderomotive potential effects at optical wavelengths.²³⁻³⁰

Bucksbaum *et al.*²⁵ conducted the first experiment that observed the scattering of a low-density electron beam from the focus of an intense optical laser pulse. Electrons were scattered away from the intense regions at the center of the laser focus due to the effects of the ponderomotive potential. This experiment also showed the interesting effect of electrons gaining (or losing) energy by “surfing” on the leading (or trailing) temporal edges of the laser pulse. This confirmed a prediction by Kibble that the ponderomotive potential can act inelastically and transfer energy between the field and the electron in time-dependent pulses, as with any time-dependent potential.

The electrons investigated in the experiments described in this thesis were produced by ionization of Neon in a high-intensity laser focus. In 1989, Corkum *et al.*³¹ examined the energy distribution of electrons ionized from xenon with a 2.5 ps

pulse length CO₂ laser at approximately 10^{14} W/cm² ($\Phi_{\text{osc}} \approx 1$ keV). A large focal spot was used to ensure that the ponderomotive potential did not accelerate the electrons. This lack of ponderomotive acceleration was caused by the combination of a large focal spot with a short pulse. In this case, the electron had insufficient time to “roll down” the ponderomotive potential before the pulse was past (see section 3.4). In both linear and circular polarization, the observed energy distributions were in good agreement with theoretical calculations of the energy of an electron born at rest in the field.

In our experiments, electrons are ionized from low-density Neon gas in an optical wavelength ($\hbar\omega \approx 1$ eV) Gaussian laser focus with a peak intensity of $I \geq 10^{18}$ W/cm². The electrons are born approximately at rest³¹ and the force on the electrons, resulting from the ponderomotive potential, is proportional to the gradient of the intensity. This force is symmetric about 90° to \vec{k} for a Gaussian focus. However, the derivation of the ponderomotive potential does not include the effects of high-intensity Compton scattering. High-intensity Compton scattering results in a component of the electrons’ momentum in the direction of \vec{k} or the longitudinal direction.

Our observations (see Figure 1.4) show a significant longitudinal component of electron momentum (25% of total momentum) for electrons ejected with high kinetic energies (84 keV) and relativistic velocities ($v_{\text{peak}} = 0.66c$). The observed

longitudinal momentum agrees well with the predictions of high-intensity Compton scattering (solid line in Figure 1.4).

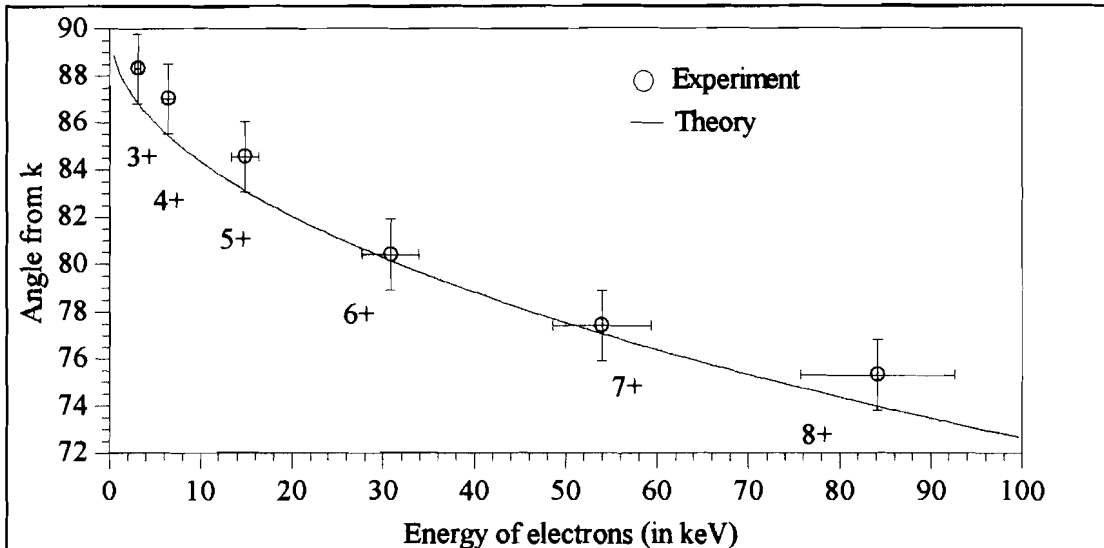


Figure 1.4: The kinetic energy of electrons versus their angle from \vec{k} following ejection from the laser focus. A forward component of the electrons' momentum that "pushes" the electrons toward \vec{k} is evident. The observed forward component of momentum is in good agreement with predictions based on high-intensity Compton scattering (solid line).

1.1 Outline

Chapter 2 derives the relativistic trajectory of an electron in an arbitrary-intensity plane wave. An electron is seen to develop a drift in the direction of \vec{k} at high intensities. This drift is shown to be the result of the absorption of momentum from the laser field and is consistent with high-intensity Compton scattering.

Chapter 3 incorporates the plane-wave results derived in Chapter 2 into predictions for a laser focus with spatial and temporal variations. The ponderomotive

potential is derived in the non-relativistic limit. The temporal variation of our laser pulse is shown to have little impact on the experiments presented in this thesis. The high-intensity Compton scattering correction to the ponderomotive potential is addressed.

Chapter 4 discusses a fully relativistic Monte Carlo simulation of electron dynamics in the laser focus. The angular distribution is seen to deviate from the ponderomotive potential predictions due to high-intensity Compton effects. The high-intensity Compton scattering correction to the ponderomotive potential discussed in Chapter 3 accurately describes the fully relativistic predictions.

Chapter 5 describes the laser and the experimental setup of the magnetic spectrometer used for the detection of the electrons. The angular resolving capabilities of this spectrometer allow the measurement of the angular distribution of the electrons relative to \vec{k} , and the corresponding axial component of the electron's momentum.

Chapter 6 discusses the electrons' energy and angular distributions obtained in our experiments. The theoretical predictions of the electrons' energies and ejection angles are in good agreement with the experimental observations.

The conclusions are presented in Chapter 7.

Appendix A is a printout of the Monte Carlo simulation computer code used to calculate the trajectories of electrons ionized from the various charge states of noble

gases. Appendix B shows the schematics of the magnetic spectrometer used for detection of the electrons in the experiment. Appendix C is a printout of the computer code used to calculate the electron trajectories through the magnetic spectrometer. Appendix D gives the measured electron energy spectra of the electrons ionized from Neon and subsequently ejected from the laser focus. These nine energy spectra at different angles from the laser \vec{k} were used to determine the angular distributions of the various charge states relative to \vec{k} . The angular distributions appear in Appendix E.

¹ J.D. Jackson, *Classical Electrodynamics* 2nd ed., (Wiley, New York, 1975).

² P.L. Kapitza and P.A.M. Dirac, "The reflection of electrons from standing light waves," *Proc. Cambridge Phil. Soc.* 29, 297 (1933).

³ L.S. Bartell, H.B. Thompson, R.R. Roskos, "Observation of stimulated Compton scattering of electrons by laser beam," *Phys. Rev. Lett.* 14, 851 (1965).

⁴ H. Schwartz, H.A. Tourtelotte, and W.W. Gaertner, "Direct observation of nonlinear scattering of electrons by laser beam," *Phys. Lett.* 19, 202 (1965).

⁵ L.S. Bartell, R.R. Roskos and H. Bradford Thompson, "Reflection of electrons by standing light waves: Experimental study," *Phys. Rev.* 166, 1494 (1968).

⁶ E. Arimondo, H. Lew, and T. Oka, "Deflection of a Na beam by resonant standing-wave radiation," *Phys. Rev. Lett.* 43, 753 (1979).

⁷ Phillip L. Gould, George A. Ruff, and David E. Pritchard, "Diffraction of atoms by light: The near-resonant Kapitza-Dirac effect," *Phys. Rev. Lett.* 56, 827 (1986).

⁸ P.H. Bucksbaum, D.W. Schumacher, and M. Bashkansky, "High-intensity Kapitza-Dirac effect," *Phys. Rev. Lett.* 61, 1182 (1988).

- ⁹ Lowell S. Brown and T.W.B. Kibble, "Interaction of intense laser beams with electrons," *Phys. Rev.* 133, A705 (1964).
- ¹⁰ Zoltan Fried and Joseph H. Eberly, "Scattering of a high-intensity, low-frequency electromagnetic wave by an unbound electron," *Phys. Rev.* 136, B871 (1964).
- ¹¹ T.W.B. Kibble, "Frequency shift in high-intensity Compton scattering," *Phys. Rev.* 138, B740 (1965).
- ¹² J. J. Sanderson, "Corrections to Thomson scattering for intense laser beams," *Phys. Lett.* 18, 114 (1965).
- ¹³ Joseph H. Eberly, "Proposed experiment for observation of nonlinear Compton wavelength shift," *Phys. Rev. Lett.* 15, 91 (1965).
- ¹⁴ T.W.B. Kibble "Radiative corrections to Thomson scattering from laser beams," *Phys. Lett.* 20, 627 (1966).
- ¹⁵ Joseph H. Eberly and Arthur Sleeper, "Trajectory and mass shift of a classical electron in a radiation pulse," *Phys. Rev.* 176, 1570 (1968).
- ¹⁶ Joseph H. Eberly, "Interaction of very intense light with free electrons," *Progress in Optics*, edited by E. Wolf, (North-Holland, Amsterdam, 1969), Vol. 7.
- ¹⁷ H.A.H. Boot and R.B. R.-S.-Harvie, "Charged particles in a non-uniform radio-frequency field," *Nature* 180, 1187 (1957).
- ¹⁸ H.A.H. Boot, S.A. Self, and R.B. R.-Shersby-Harvie, "Containment of a fully-ionized plasma by a radio-frequency field," *J. Electr. Control* 4, 434(1958).
- ¹⁹ A. V. Gaponov and M. A. Miller, "Potential wells for charged particles in a high-frequency electromagnetic field," *J. Exptl. Theoret. Phys. (U.S.S.R.)* 34, 242 (1958) [*Soviet Phys. JETP* 7, 168 (1958)].
- ²⁰ G.A. Askar'yan, "Effects of the gradient of a strong electromagnetic beam on electrons and atoms," *J. Exptl. Theoret. Phys. (U.S.S.R.)* 42, 1567 (1962) [*Soviet Phys. JETP* 15, 1088 (1962)].
- ²¹ T.W.B. Kibble, "Refraction of electron beams by intense electromagnetic waves," *Phys. Rev. Lett.* 16, 1054 (1966).

- ²² T.W.B. Kibble, "Mutual refraction of electrons and photons," *Phys. Rev.* 150, 1060 (1966).
- ²³ M.J. Hollis, "Multiphoton ionization and EM field gradient forces," *Optics Communications* 25, 395 (1978).
- ²⁴ R.R. Freeman, T.J. McIlrath, P.H. Bucksbaum, and M. Bashkansky, "Ponderomotive effects on angular distributions of photoelectrons," *Phys. Rev. Lett.* 57, 3156 (1986).
- ²⁵ P.H. Bucksbaum, M. Bashkansky, and T.J. McIlrath, "Scattering of electrons by intense coherent light," *Phys. Rev. Lett.* 58, 349 (1987).
- ²⁶ R.R. Freeman, P.H. Bucksbaum, H. Milchberg, S. Darack, D. Schumacher, and M.E. Geusic, "Above-Threshold Ionization with subpicosecond laser pulses," *Phys. Rev. Lett.* 59, 1092 (1987).
- ²⁷ T.F. Gallagher, "Above-Threshold Ionization in low-frequency limit," *Phys. Rev. Lett.* 61, 2304 (1988).
- ²⁸ M.D. Perry, O.L. Landen, and A. Szöke, "Measurement of the local laser intensity by photoelectron energy shifts in multiphoton ionization," *J. Opt. Soc. Am. B* 6, 344 (1989).
- ²⁹ P. Monot, T. Auguste, L.A. Lompré, G. Mainfray, and C. Manus, "Energy measurements of electrons submitted to an ultrastrong laser field," *Phys. Rev. Lett.* 70, 1232 (1993).
- ³⁰ U. Mohideen, M.H. Sher, H.W.K. Tom, G.D. Aumiller, O.R. Wood II, R.R. Freeman, J. Bokor, and P.H. Bucksbaum, "High intensity Above-Threshold Ionization of He," *Phys. Rev. Lett.* 71, 509 (1993).
- ³¹ P.B. Corkum, N.H. Burnett, and F. Brunel, "Above-threshold ionization in the long-wavelength limit," *Phys. Rev. Lett.* 62, 1259 (1989).

Chapter 2

Electron dynamics in an arbitrary-intensity plane wave

A free electron oscillating in an arbitrary-intensity electromagnetic field has an average quiver energy,

$$\Phi_{\text{osc}} \equiv \langle \text{Energy} \rangle = \frac{e^2 \langle \tilde{A}^2 \rangle}{2mc^2} \quad (2.1)$$

where m and e are the electron's rest mass and charge respectively, c is the speed of light in vacuum, \tilde{A} is the vector potential, and the brackets denote averaging over one cycle of the field. Another useful parameter in high-field interactions with electrons is the quiver velocity, v_{osc} . By this one means the electron's peak velocity in an electromagnetic field (ignoring relativistic effects),

$$v_{\text{osc}} \equiv \frac{eA_0}{mc}, \quad (2.2)$$

where A_0 is the peak vector potential of the field.

When $\Phi_{\text{osc}} \sim mc^2$ or $v_{\text{osc}} \sim c$, an electron's trajectory must be calculated relativistically. An exact analytic solution of the relativistic equation of motion of an electron in an electromagnetic field is possible only in the simplest fields. This chapter

will find the relativistic trajectory of an electron using the simplest case of all, a plane wave.

2.1 Electron's equation of motion in a high-intensity plane wave

Some of the many theoretical investigations of the behavior of electrons in intense fields are given in references 1-18. The relativistic equation of motion of an electron born at rest in a plane wave will be found here using the Hamilton-Jacobi technique.^{11,13,19} The following derivation differs from Sarachik and Schappert's derivation¹³ by the assumption of an electron born at rest in an already intense field (Sarachik and Schappert assumed an electron at rest in the absence of any field and subsequent interaction with a pulsed field). The Hamilton-Jacobi equation of motion is found from the square of the four-vector momentum,

$$p_{\mu}p^{\mu} = -m^2c^2 \quad (2.1.1)$$

or

$$\left(\frac{E(\vec{r}, t)}{c}\right)^2 - \vec{p}(\vec{r}, t)^2 = m^2c^2, \quad (2.1.2)$$

where $E(\vec{r}, t)$ is the electron's energy and $\vec{p}(\vec{r}, t)$ is the electron's momentum. In the Hamilton-Jacobi formalism, the action or principal function S satisfies,

$$\vec{p}(\vec{r}, t) + \frac{e\vec{A}(\vec{r}, t)}{c} = \vec{\nabla}S(\vec{r}, t) \equiv \vec{P}_{\text{can}}(\vec{r}, t) \quad (2.1.3)$$

and

$$\mathbf{E}(\vec{r}, t) = -\frac{\partial \mathcal{S}(\vec{r}, t)}{\partial t}, \quad (2.1.4)$$

where \vec{P}_{can} is the canonical momentum. After substituting the above expressions for the energy and the momentum into equation (2.1.2), we find the Hamilton-Jacobi equation of motion,

$$\left(\vec{\nabla} \mathcal{S}(\vec{r}, t) - \frac{e\vec{A}(\vec{r}, t)}{c} \right)^2 - \frac{1}{c^2} \left(\frac{\partial \mathcal{S}(\vec{r}, t)}{\partial t} \right)^2 + m^2 c^2 = 0. \quad (2.1.5)$$

In a plane-wave oscillatory field, \vec{A} can be represented by,

$$\vec{A}(\vec{r}, t) = \vec{A}(\eta) \quad (2.1.6)$$

where $\eta \equiv \omega t - \vec{k} \cdot \vec{r}$ is the Lorentz invariant phase. With this dependence on \vec{r} and t , the solution of equation (2.1.5) has the form,

$$\mathcal{S}(\vec{r}, t) = \vec{\alpha} \cdot \vec{r} + \beta ct + \Psi(\eta) \quad (2.1.7)$$

where $\vec{\alpha}$ and β are constants found from the initial conditions,

$$\Psi(\eta) = \frac{\int_{\eta_0}^{\eta} \left(\alpha^2 - \beta^2 + m^2 c^2 - \frac{2e\vec{\alpha} \cdot \vec{A}(\eta')}{c} + \frac{e^2 \vec{A}^2(\eta')}{c^2} \right) d\eta'}{2(\vec{\alpha} \cdot \vec{k} + \beta k)}, \quad (2.1.8)$$

and η_0 is the initial phase. The canonical momentum can be found by substituting equation (2.1.7) in equation (2.1.3),

$$\vec{P}_{\text{can}}(\eta) = \vec{\alpha} - \vec{k} \left(\frac{\vec{\alpha}^2 - \beta^2 + m^2 c^2 - \frac{2e}{c} \vec{\alpha} \cdot \vec{A}(\eta) + \frac{e^2}{c^2} \vec{A}^2(\eta)}{2(\vec{\alpha} \cdot \vec{k} + \beta k)} \right), \quad (2.1.9)$$

and the energy can be found by substituting equation (2.1.7) in equation (2.1.4),

$$E(\eta) = -c \left(\beta + \frac{\vec{k}}{k} \cdot (\vec{\alpha} - \vec{P}_{\text{can}}(\eta)) \right). \quad (2.1.10)$$

The trajectory of the electron is determined by differentiating the principal function with respect to the spatial constant $\vec{\alpha}$, and equating this with the electron's initial position,

$$\begin{aligned} \vec{r}(\eta) = \vec{r}(0) - \int_{\eta_0}^{\eta} \frac{\vec{\alpha} - \frac{e}{c} \vec{A}(\eta')}{\vec{\alpha} \cdot \vec{k} + \beta k} d\eta' \\ + \int_{\eta_0}^{\eta} \vec{k} \frac{\vec{\alpha}^2 - \beta^2 + m^2 c^2 - \frac{2e}{c} \vec{\alpha} \cdot \vec{A}(\eta') + \frac{e^2}{c^2} \vec{A}^2(\eta')}{2(\vec{\alpha} \cdot \vec{k} + \beta k)^2} d\eta' \end{aligned} \quad (2.1.11)$$

To find the constants $\vec{\alpha}$ and β , the initial conditions must be considered. We are interested in electrons released via ionization into an intense field. From Chapter 1 we recall Corkum's results²⁰ showing that electrons are released with a very low initial velocity which we take to be zero. This gives the initial conditions,

$$\vec{P}_{\text{can}} = \frac{e\vec{A}(0)}{c} \quad \text{and} \quad E(0) = mc^2, \quad (2.1.12)$$

where we arbitrarily choose the temporal and spatial coordinates of ionization as $t = 0$ and $\vec{r} = 0$.

The constant $\vec{\alpha}$ can be separated into two components based on the transverse requirement of a plane wave. $\vec{\alpha}_\perp$ represents the component of $\vec{\alpha}$ in the plane of polarization of the field, and $\alpha_{\vec{k}}$ represents $\vec{\alpha}$ in the direction of \vec{k} . The solution of equation (2.1.9) with the initial conditions defined in equation (2.1.12) gives

$$\vec{\alpha}_\perp = \frac{e\vec{A}(0)}{c} \quad (2.1.13)$$

and

$$\alpha_{\vec{k}} = -\beta \pm mc. \quad (2.1.14)$$

Equation (2.1.10) determines the correct choice of sign in equation (2.1.14),

$$\alpha_{\vec{k}} + \beta = -mc. \quad (2.1.15)$$

These constants are arbitrary except in their relation to each other. We can therefore use

$$\vec{\alpha} = \frac{e\vec{A}(0)}{c} \quad \text{and} \quad \beta = -mc \quad (2.1.16)$$

without loss of generality. The choice of $\alpha_{\vec{k}} = 0$ and $\beta = -mc$ defines the gauge and simplifies the algebra considerably. In their derivation, Sarachik and Schappert used a plane wave with a temporal envelope varying slowly compared to the period of the field. They considered an electron at rest before the pulse passed over the electron.

This resulted in $\bar{\alpha} = 0$ and $\beta = -mc$. An electron released into an intense plane wave results in $\bar{\alpha} \neq 0$ if $\bar{A}(0) \neq 0$, which is always the case in circular polarization. This result is a consequence of the electron being released into a field with non-zero initial canonical momentum,²⁰⁻²² as will be discussed in section 2.2.

Substitution of the constants in equation (2.1.16) into equations (2.1.9), (2.1.10), and (2.1.11) gives the electron's momentum, energy, and trajectory,

$$\bar{p}(\eta) = \frac{e}{c}(\bar{A}(0) - \bar{A}(\eta)) + \frac{\bar{k}}{k} \frac{e^2}{2mc^3} \left((\bar{A}(0) - \bar{A}(\eta))^2 \right), \quad (2.1.17)$$

$$E(\eta) = mc^2 \left(1 + \frac{e^2}{2m^2c^4} (\bar{A}(0) - \bar{A}(\eta))^2 \right), \quad (2.1.18)$$

and

$$\bar{r}(\eta) = \bar{r}(0) + \frac{e}{mc^2k} \int_{\eta_0}^{\eta} \left((\bar{A}(0) - \bar{A}(\eta')) + \frac{\bar{k}}{2} \frac{e}{mc^2k} (\bar{A}(0) - \bar{A}(\eta'))^2 \right) d\eta'. \quad (2.1.19)$$

The average energy of the electron is

$$\langle E \rangle = mc^2 + \frac{e^2 \bar{A}^2(0)}{2mc^2} + \frac{e^2 \langle \bar{A}^2(\eta) \rangle}{2mc^2}. \quad (2.1.20)$$

The first term is the rest energy of the electron. The second term arises as a consequence of the electron's release into a field with non-zero initial canonical momentum.²⁰⁻²² The third term is the average energy of the electron due to oscillations in the field, i.e., the quiver energy as defined in equation (2.1).

2.2 Electron trajectories in linear and circular polarization

To investigate the characteristic behavior of an electron in linear or circular polarization, we now consider an explicit choice of the vector potential,

$$\vec{A}(\eta) = A_0 \left(\hat{x} \delta \sin \eta + \hat{y} (1 - \delta^2)^{\frac{1}{2}} \cos \eta \right), \quad (2.2.1)$$

where the polarization is linear if $\delta = \pm 1$ or 0, or circular if $\delta = \pm 1/\sqrt{2}$. The electron's momentum and energy in the vector potential described by equation (2.2.1) are

$$\vec{p}(\eta) = mc \left(\begin{array}{l} q \left(\hat{x} \delta \sin \eta - \hat{y} (1 - \delta^2)^{\frac{1}{2}} (1 - \cos \eta) \right) + \\ \hat{z} \frac{q^2}{2} \left[\left(\frac{3}{2} - \delta^2 \right) - 2(1 - \delta^2) \cos \eta + \left(\frac{1}{2} - \delta^2 \right) \cos 2\eta \right] \end{array} \right) \quad (2.2.2)$$

and

$$E(\eta) = mc^2 \left(1 + \frac{q^2}{2} \left[\left(\frac{3}{2} - \delta^2 \right) - 2(1 - \delta^2) \cos \eta + \left(\frac{1}{2} - \delta^2 \right) \cos 2\eta \right] \right), \quad (2.2.3)$$

and the electron's trajectory is

$$\vec{r}(\eta) = \frac{1}{k} \left(\begin{array}{l} q \left(\hat{x} \delta (1 - \cos \eta) - \hat{y} (1 - \delta^2)^{\frac{1}{2}} (\eta - \sin \eta) \right) + \\ \hat{z} \frac{q^2}{2} \left[\left(\frac{3}{2} - \delta^2 \right) \eta - 2(1 - \delta^2) \sin \eta + \frac{1}{2} \left(\frac{1}{2} - \delta^2 \right) \sin 2\eta \right] \end{array} \right), \quad (2.2.4)$$

where q^2 is a dimensionless parameter defined by Sarachik and Schappert as $4\Phi_{\text{osc}}/mc^2$.

The experiments described in this thesis use electrons released by ionization in an intense laser field as a source of free electrons. The choice of ionization at $\eta=0$ sets conditions on the values of δ for a physically realistic model of an electron released via ionization. This can be understood by a short description of the physics of strong field ionization in an optical field.

Ionization of atoms with intense optical laser fields has traditionally been divided into two regimes, multiphoton and tunneling. The two regimes are differentiated by the Keldysh parameter²³

$$\gamma = \sqrt{\frac{E_{\text{ion}}}{2\Phi_{\text{osc}}}}, \quad (2.2.5)$$

where E_{ion} is the ionization potential of the atom.

For $\gamma > 1$, the binding potential within the atom dominates the electron's motion, and the laser field can be considered as a perturbation to the atom. Perturbation theory can then be used to calculate the transition rates from the bound state to unbound states. This regime is known as multiphoton ionization (MPI).²³⁻³³

For $\gamma < 1$, the quiver energy of the electron in the field is greater than the binding energy to the atom, and the field can no longer be treated perturbatively. In this case, the electron is considered trapped in the Coulomb potential well of the atom

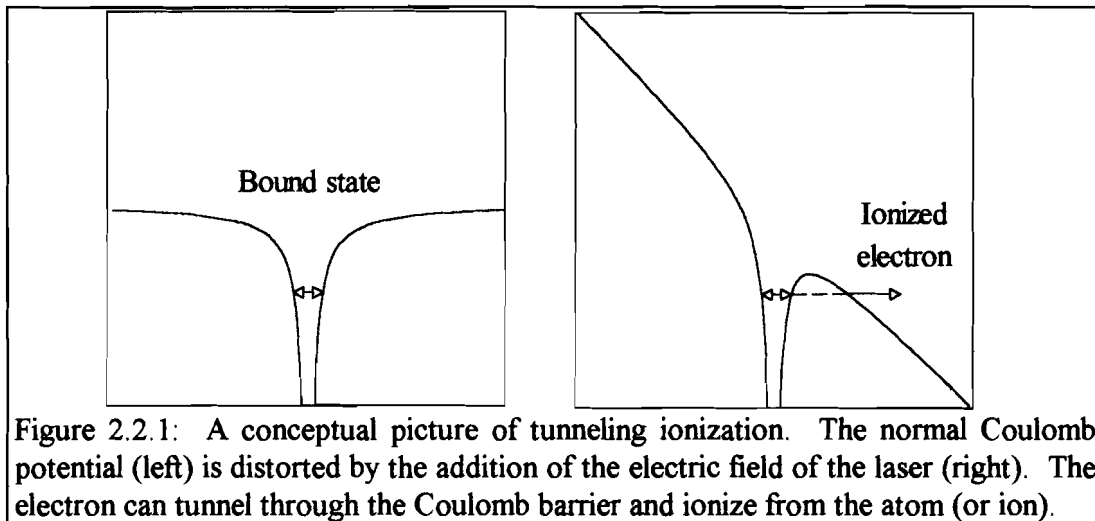


Figure 2.2.1: A conceptual picture of tunneling ionization. The normal Coulomb potential (left) is distorted by the addition of the electric field of the laser (right). The electron can tunnel through the Coulomb barrier and ionize from the atom (or ion).

(or ion), and the electric field of the laser distorts the potential allowing tunneling through the Coulomb barrier (see Figure 2.2.1). This process is known as tunneling ionization.^{23,29,33-42}

The strong field limit of tunneling ionization is Coulomb barrier suppression ionization (BSI).⁴² In this case, the electron gains enough energy from the field to

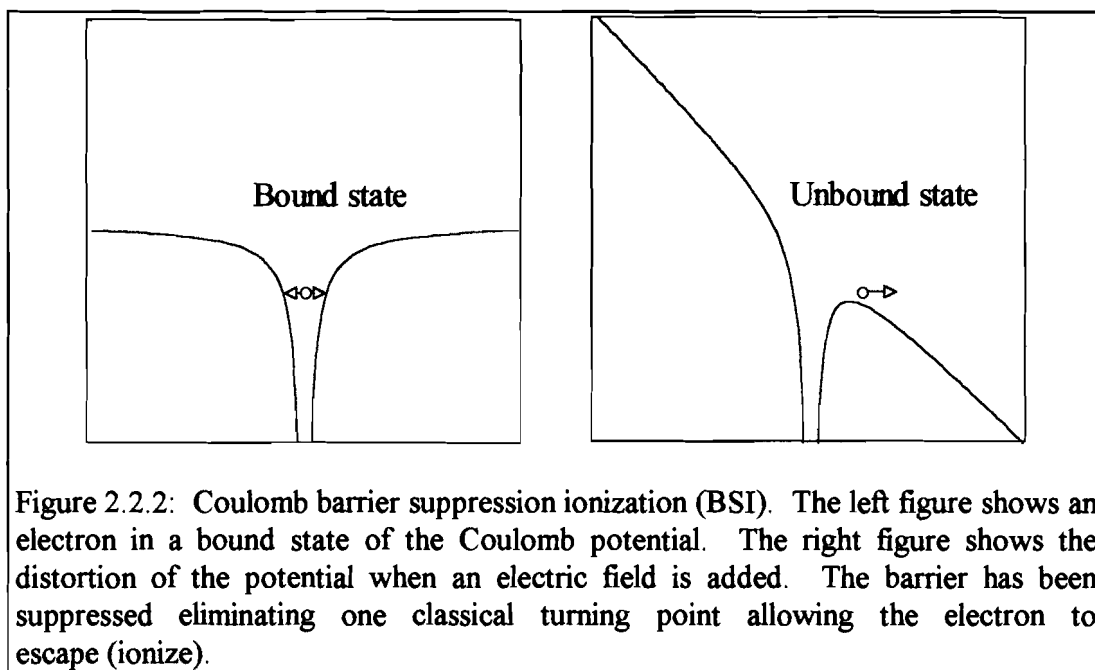


Figure 2.2.2: Coulomb barrier suppression ionization (BSI). The left figure shows an electron in a bound state of the Coulomb potential. The right figure shows the distortion of the potential when an electric field is added. The barrier has been suppressed eliminating one classical turning point allowing the electron to escape (ionize).

pass over the Coulomb barrier and become ionized (see Figure 2.2.2). BSI only occurs in low-frequency fields since the field must remain in one direction long enough for the electron to travel over the barrier before the field changes direction. The electric field at which BSI occurs is found by superimposing the potential of a static electric field on the Coulomb potential,

$$V(x) = -\frac{eZ}{|x|} - \mathcal{E}x, \quad (2.2.6)$$

where Z is the ionic charge (the charge of the ion created after ionization) and \mathcal{E} is the quasi-static electric field of the laser. Only one dimension is necessary since the field is approximated as constant during the ionization process. The local maximum value of equation (2.2.6) equated with the electron's ionization potential yields the critical electric field necessary for ionization,

$$\mathcal{E}_{\text{crit}} = \frac{E_{\text{ion}}^2}{4Ze^3}. \quad (2.2.7)$$

The noble gas charge states examined in the experiments described in this thesis (He^{2+} and Ne^{3+} to Ne^{8+}) have previously been shown to ionize in agreement with the BSI model of ionization.⁴² This model will therefore be used to describe the ionization process.

The Coulomb barrier will be suppressed most when the electric field is at its maximum. The electron is therefore most likely to be released at the peak of the electric field. In the vector potential described by equation (2.2.1), $\delta = \pm 1$

corresponds to linear polarization with the electric field peaked at $\eta=0$, the phase chosen for release of the electron into the field. The other linear polarization case of $\delta=0$ corresponds to the electric field being zero at $\eta=0$, and is therefore not a physically realistic model of ionization. In circular polarization, $\delta = \pm 1/\sqrt{2}$, the magnitude of the field is constant. Both values of δ are therefore physically realistic since there is no “preferred” phase where the field is peaked.

$\delta = \pm 1$ specifies the vector potential as $\vec{A}(\eta) = \pm \hat{x} A_0 \sin \eta$, or polarization in the x-direction. This is not a general requirement. The form of the vector potential in equation (2.2.1) and choosing $\vec{r} = t = \eta = 0$ has resulted in this requirement. In an actual experiment, the polarization of the field (which can be any direction) specifies the vector potential, and the position of the atom (or ion) specifies \vec{r} . The time at which ionization occurs is then determined by the phase at which the field is peaked.

For $\delta = \pm 1$, equations (2.2.2-2.2.4) reduce to

$$\vec{p}(\eta) = mc \left(\pm \hat{x} q \sin \eta + \hat{z} \left(\frac{q^2}{4} - \frac{q^2}{4} \cos 2\eta \right) \right), \quad (2.2.8)$$

$$E(\eta) = mc^2 \left(1 + \frac{q^2}{4} - \frac{q^2}{4} \cos 2\eta \right), \quad (2.2.9)$$

and

$$\vec{r}(\eta) = \frac{1}{k} \left(\pm \hat{x} q (1 - \cos \eta) + \hat{z} \frac{q^2}{2} \left[\left(\frac{1}{2} \right) \eta - \frac{1}{4} \sin 2\eta \right] \right). \quad (2.2.10)$$

The electron trajectory, $\vec{r}(\eta)$, can be separated into individual components,

$$x = \pm \frac{q}{k}(1 - \cos\eta),$$

$$y = 0,$$

and

$$z = v_d t - \frac{1}{2k} \frac{v_d}{c} \sin 2\eta, \quad (2.2.11)$$

where

$$v_d \equiv \frac{q^2}{4 + q^2} c.$$

The equation for z contains a non-oscillatory term that is also apparent in the z -component of the momentum shown in equation (2.2.8). The electron therefore drifts in the z -direction and in high-intensity fields ($q \sim 1$ or greater), the drift velocity is appreciable. As will be shown in section 2.3, the drift can be explained using the conservation laws of energy and momentum or, equivalently, the electron's recoil due to high-intensity Compton scattering.

It is important to note that the trajectory described by equations (2.2.11) is not simply an oscillation at the laser frequency for x and twice the laser frequency for z , because η itself depends on x and z . These are transcendental equations that contain an infinite number of harmonics in their solution, which generate an infinite number of harmonics in the scattered radiation.^{3,4,13,15,17}

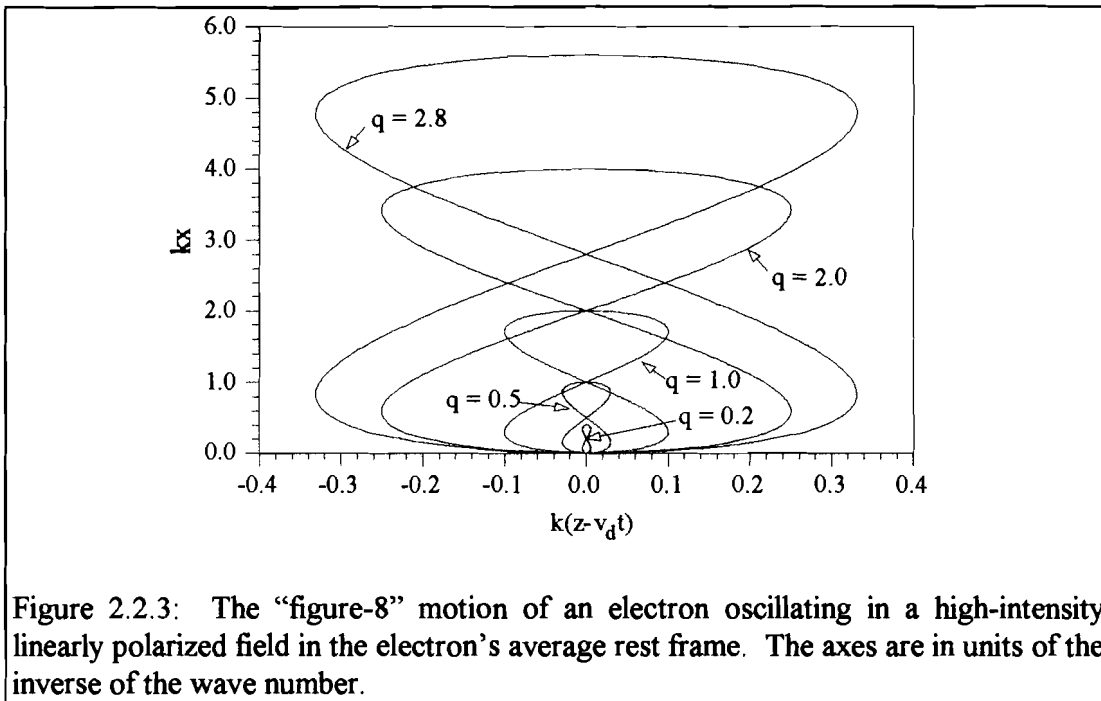


Figure 2.2.3: The “figure-8” motion of an electron oscillating in a high-intensity linearly polarized field in the electron’s average rest frame. The axes are in units of the inverse of the wave number.

The orbits of the electron can be found by eliminating η in equations (2.2.11),

$$(z - v_d t)^2 = \frac{1}{k^2} \frac{v_d}{c} \left(1 \mp \frac{kx}{c} \right)^2 \left(1 - \left(1 \mp \frac{kx}{q} \right)^2 \right). \quad (2.2.12)$$

Orbits for $\delta=1$ (neglecting the drift) are plotted in Figure 2.2.3 for a variety of values of q . The orbits shown represent only one lobe of the allowed orbits. Another lobe will occur with all negative x values due to the possibility of ionization when the field is reversed from that assumed above, i.e., at $\delta = -1$. For $q \ll 1$, the electron oscillates predominantly in the x -direction, as expected for low intensities. As q approaches and exceeds one, the electron begins to experience significant oscillations in the z -direction. These oscillations in the z -direction occur at twice the frequency of the x -

oscillations. This causes a “figure-8” motion in the electron’s average rest frame that was shown by Sarachik and Schappert.¹³

An inherently relativistic effect for an electron with $q=100$ is shown in Figure 2.2.4. The maximum amplitude of the oscillations in z is given by $k|z - v_d t| < 1/2$, while the oscillations in x are unbounded and increase linearly in q for large q . This is due to the effect of the electron’s drift velocity in z . In the lab frame, the spatial extent of one wavelength of light sets an upper limit on the distance the electron can oscillate in z before being “turned around” by the field. The x -direction has no such limit. The Lorentz transformation to and from the rest frame of the electron explains this result. In the electron’s average rest frame (the frame moving with velocity v_d), the electron experiences a much longer wavelength due to the Doppler shift. When the electron

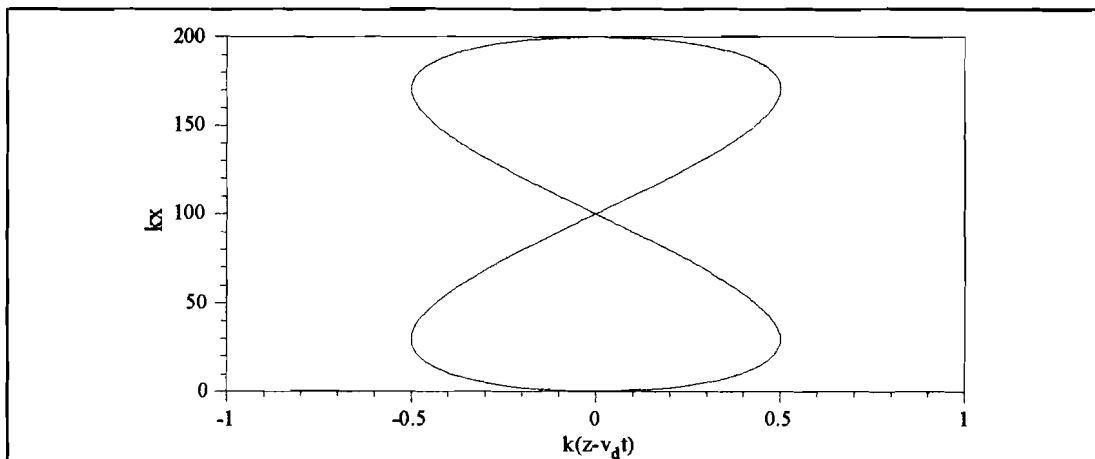


Figure 2.2.4: A highly relativistic electron trajectory ($q=100$) in the electron’s average rest frame. Both axes are in units of the inverse of the wave number. The maximum amplitude of the oscillations in z is given by $k|z - v_d t| < 1/2$ while the amplitude of the oscillation in x is much larger. This effect is due to the limit imposed on the z oscillations of one wavelength. The x oscillations have no such limit.

motion is transformed back to the lab frame, the oscillations in z are transformed back to a maximum amplitude of one wavelength. However, the x oscillations are unaffected by this transformation, and therefore behave as if in the presence of a much longer wavelength field, resulting in a larger quiver amplitude than the z oscillations.

For the case of circular polarization ($\delta = \pm 1/\sqrt{2}$),

$$\vec{p}(\eta) = mc \left(\pm \frac{q}{\sqrt{2}} (\hat{x} \sin \eta - \hat{y} (1 - \cos \eta)) + \hat{z} \left(\frac{q^2}{2} - \frac{q^2}{2} \cos \eta \right) \right), \quad (2.2.13)$$

$$E(\eta) = mc^2 \left(1 + \frac{q^2}{2} - \frac{q^2}{2} \cos \eta \right), \quad (2.2.14)$$

and

$$\vec{r}(\eta) = \frac{1}{k} \left(\pm \frac{q}{\sqrt{2}} (\hat{x} (1 - \cos \eta) - \hat{y} (\eta - \sin \eta)) + \hat{z} \frac{q^2}{2} (\eta - \sin \eta) \right). \quad (2.2.15)$$

Equation (2.2.15) can be separated into individual components,

$$x = \pm \frac{q}{k\sqrt{2}} (1 - \cos \eta),$$

$$y = \mp v'_{dy} t \pm \frac{1}{k} \frac{v'_{dy}}{c} \sin \eta,$$

and

$$z = v'_{dz} t - \frac{1}{k} \frac{v'_{dz}}{c} \sin \eta, \quad (2.2.16)$$

where

$$v'_{dz} \equiv \frac{q^2}{2+q^2} c \quad \text{and} \quad v'_{dy} = \frac{q \left(1 - \frac{v'_{dz}}{c}\right)}{\sqrt{2}} c.$$

Both the y and z components now contain a drift velocity. The orbit of the electron can again be found by eliminating η in equation (2.2.16) which results in

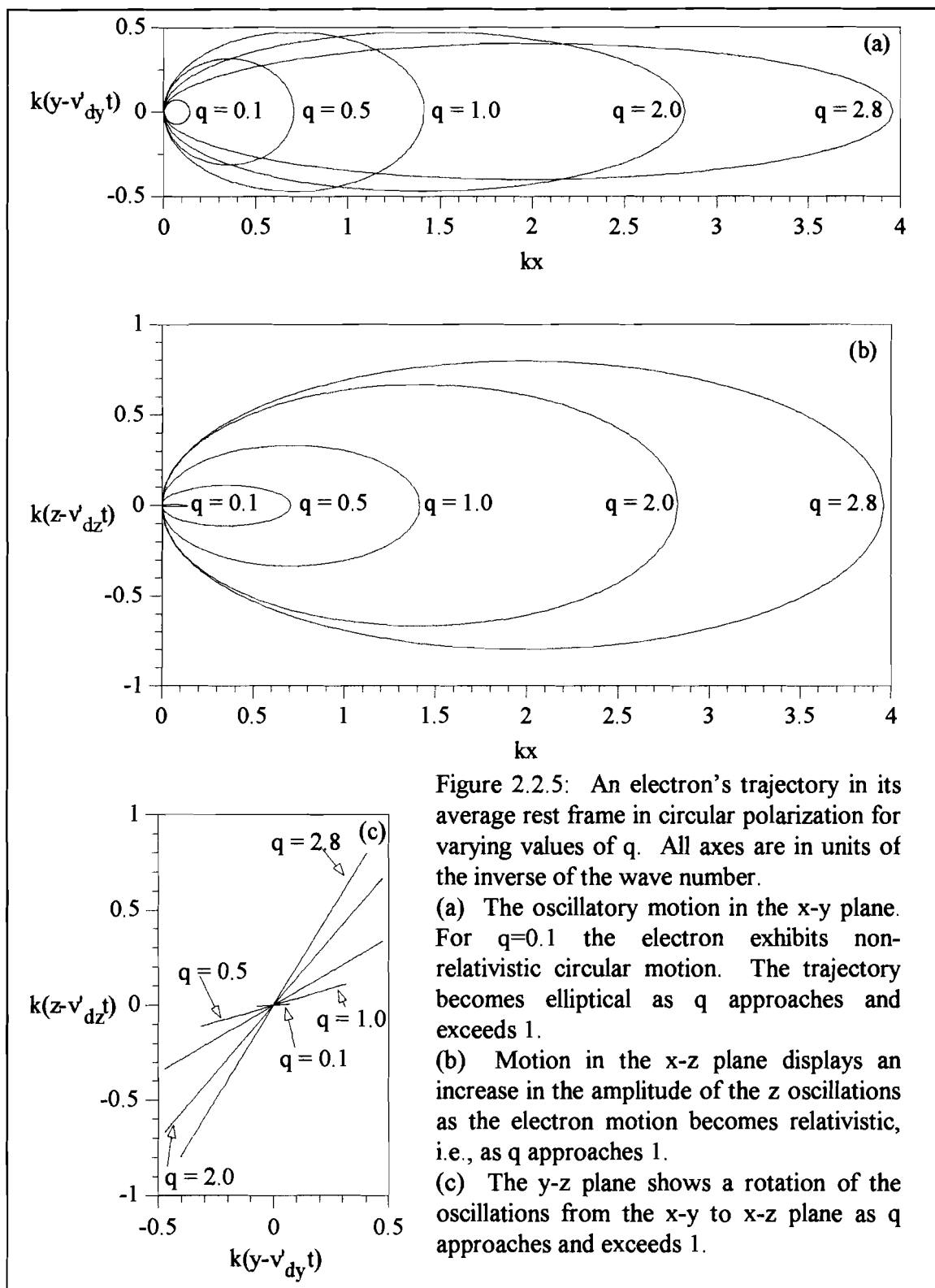
$$\frac{(y \pm v'_{dy} t)^2}{\frac{q^2}{2k^2} \left(1 - \frac{v'_{dz}}{c}\right)^2} + \frac{\left(x \pm \frac{q}{\sqrt{2}k}\right)^2}{\frac{q^2}{2k^2}} = 1 \quad (2.2.17)$$

and

$$\frac{(z - v'_{dz} t)^2}{\frac{1}{k^2} \left(\frac{v'_{dz}}{c}\right)^2} + \frac{\left(x \pm \frac{q}{\sqrt{2}k}\right)^2}{\frac{q^2}{2k} \left(\frac{v'_{dz}}{c}\right)^2} = 1. \quad (2.2.18)$$

These two equations are equations for ellipses. For $q \ll 1$, Equation (2.2.17) reduces to the equation of a circle with radius $q/\sqrt{2}k$, which is the standard trajectory of an electron oscillating in a non-relativistic, circularly polarized field. As q approaches and exceeds one, the x-y orbit becomes elliptical and oscillations in z become apparent (see Figure 2.2.5).

The drift of the electron in the y-direction is caused by the conservation of canonical momentum.²⁰⁻²² When the electron is released into the field at $\eta=0$, the canonical momentum is non-zero in circular polarization and points in the direction of $\vec{A}(0)$ (the $\pm y$ direction in the above example). As the vector potential rotates away



from $\vec{A}(0)$, the total canonical momentum must be conserved, which requires that the electron gain momentum in the $\vec{A}(0)$ direction. After the field rotates through π radians, this process reverses and the electron loses momentum to the field. This exchange of momentum continues throughout each laser cycle. The momentum gained by the electron is always in the direction of the initial canonical momentum. This causes the electron to drift in the $\vec{A}(0)$ direction.

The y-direction of this drift is caused by specifying $\vec{r} = t = 0$ as the position and time of ionization. In circular polarization, ionization is equally probable to occur at any phase since the probability of ionization is related to the amplitude of the field, and the amplitude of the field is independent of the phase. Ionization at an arbitrary phase results in an arbitrary direction to the canonical momentum drift, since the direction of the initial canonical momentum is dependent on the phase at the time of ionization.

2.3 The longitudinal drift

The motion of the electron in the \vec{k} direction is due to conservation of energy and momentum between the electron and the field. An electron oscillates in a plane wave with an energy (see equation (2.1.18)),

$$E(\eta) = mc^2 \left(1 + \frac{e^2}{2m^2c^4} (\vec{A}(0) - \vec{A}(\eta))^2 \right). \quad (2.3.1)$$

The electron was ionized with zero initial velocity ($E(0) = mc^2$) and has therefore gained an energy from the field of

$$\Delta E = E(\eta) - E(0) = \frac{e^2}{2mc^2} (\bar{A}(0) - \bar{A}(\eta))^2. \quad (2.3.2)$$

The absorption of energy from the field must be accompanied by an absorption of momentum. The only available momentum is in the field propagation direction (\vec{k}).

Therefore, to conserve momentum, the electron's \vec{k} momentum component must be

$$p_{\vec{k}} = \frac{\Delta E}{c} = \frac{e^2}{2mc^3} (\bar{A}(0) - \bar{A}(\eta))^2, \quad (2.3.3)$$

$p_{\vec{k}}$ is the same as the \vec{k} momentum component of an electron oscillating in a plane wave (see section 2.1),

$$\vec{p}(\eta) = \frac{e}{c} (\bar{A}(0) - \bar{A}(\eta)) + \frac{\vec{k}}{k} \frac{e^2}{2mc^3} \left((\bar{A}(0) - \bar{A}(\eta))^2 \right).$$

The motion of an electron in the \vec{k} direction in a plane wave is therefore due to the absorption of momentum from the field.

The forward drift found in linear and circular polarization in section 2.2 is caused by the positive-definite, non-zero average of the momentum shown in equation (2.3.3),

$$\langle p_{\vec{k}} \rangle = \frac{e^2}{2mc^3} \left(\bar{A}^2(0) + \langle \bar{A}^2(\eta) \rangle \right). \quad (2.3.4)$$

The vector potential used previously in section 2.2,

$$\vec{A}(\eta) = A_0 \left(\hat{x} \delta \sin \eta + \hat{y} (1 - \delta^2)^{\frac{1}{2}} \cos \eta \right),$$

reduces equation (2.3.4) to

$$\langle p_z \rangle = mc \frac{q^2}{2} \left(\frac{3}{2} - \delta^2 \right). \quad (2.3.5)$$

For linear polarization ($\delta = \pm 1$)

$$p_z = \frac{q^2}{4} mc, \quad (2.3.6)$$

and for circular polarization ($\delta = \pm 1/\sqrt{2}$)

$$p_z = \frac{q^2}{2} mc. \quad (2.3.7)$$

Equations (2.3.6) and (2.3.7) are the same as the non-oscillatory longitudinal components of the momenta found in equations (2.2.8) and (2.2.13) respectively.

The concept that motion of the electron in the \vec{k} direction is due to field momentum is a powerful tool for calculating electron trajectories in more complicated fields.²² This concept allows a calculation of electron trajectories ignoring field momentum effects, and later including these effects by requiring conservation of energy and momentum. This technique is used in Chapter 3 to generalize predictions for a relatively low-intensity spatially and temporally varying field to high intensities. The validity of this technique is shown in Chapter 4 where numerical solutions to the

electron's equation of motion in a high-intensity laser focus are calculated and compared to the analytical predictions.

The behavior of electrons in a low-intensity optical field is fundamentally different than at high intensities. At low intensities, oscillation at the field frequency dominates the electron's motion and the drift due to high-intensity Compton scattering is negligible. At high intensities, the longitudinal drift dominates the electron trajectory and the oscillatory motion of the electron is negligible.

The low- and high-intensity limits can be examined by comparing the energy of an electron traveling with a constant momentum of p_z in the absence of an electromagnetic field to an electron oscillating in a field with an average forward momentum of $\langle p_z \rangle$. Both electrons are traveling with the same average forward momentum. However, the one in the field has additional energy due to oscillations within the field. The electron traveling with a constant momentum has a kinetic energy (total energy minus the rest energy) of

$$E_z = \left((\Delta p_z)^2 c^2 + m^2 c^4 \right)^{\frac{1}{2}} - mc^2 = mc^2 \left[\left(1 + \frac{q^4}{4} \alpha^2 \right)^{\frac{1}{2}} - 1 \right], \quad (2.3.8)$$

where

$$\alpha \equiv \left(\frac{3}{2} - \delta^2 \right).$$

The average kinetic energy of the corresponding electron in the field is

$$\langle E(\eta) \rangle = \alpha mc^2 \frac{q^2}{2}. \quad (2.3.9)$$

The ratio of the energy of the electron traveling with a constant momentum to the total energy of the corresponding electron in the field is

$$\frac{E_z}{\langle E(\eta) \rangle} = \frac{\left(1 + \frac{q^4}{4} \alpha^2\right)^{\frac{1}{2}} - 1}{\frac{q^2 \alpha}{2}}. \quad (2.3.10)$$

For low intensities or $q \ll 1$

$$\frac{E_z}{\langle E(\eta) \rangle} \approx \frac{\alpha q^2}{4} \quad (2.3.11)$$

and therefore $E_z \ll \langle E(\eta) \rangle$. In this case the energy due to the forward momentum is negligible compared to the total energy of the electron oscillating in the field. This is the regime of Thomson scattering since the oscillatory motion of the electron is dominant and the absorption of field momentum is inconsequential.

For high intensities or $q \gg 1$

$$\frac{E_z}{\langle E(\eta) \rangle} \approx 1 \quad \text{or} \quad E_z \approx \langle E(\eta) \rangle. \quad (2.3.12)$$

Therefore, for $q \gg 1$, the energy due to the forward momentum gives the dominant contribution of energy and the oscillations contain relatively little energy. This is the ultra high-intensity limit of high-intensity Compton scattering where field momentum

effects dominate and the quiver motion of the electron is insignificant. This is analogous to the high-energy photon regime ($\hbar\omega \gg mc^2$) of single photon Compton scattering, in which only the particle nature of the photon and the resulting recoil of the electron plays a role in the dynamics of the interaction.

¹ N.D. Segupta, *Bull. Math. Soc. (Calcutta)* 41, 187 (1949)

² N.D. Segupta, *Bull. Math. Soc. (Calcutta)* 44, 175 (1952)

³ Vachaspati, "Harmonics in the scattering of light by free electrons," *Phys. Rev.* 128, 664 (1962).

⁴ O. von Roos, "Interaction of very intense radiation fields with atomic systems", *Phys. Rev.* 135, A43 (1964).

⁵ Lowell S. Brown and T.W.B. Kibble, "Interaction of intense laser beams with electrons," *Phys. Rev.* 133, A705 (1964).

⁶ Zoltan Fried and Joseph H. Eberly, "Scattering of a high-intensity, low-frequency electromagnetic wave by an unbound electron," *Phys. Rev.* 136, B871 (1964).

⁷ T.W.B. Kibble, "Frequency shift in high-intensity Compton scattering," *Phys. Rev.* 138, B740 (1965).

⁸ Joseph H. Eberly, "Proposed experiment for observation of nonlinear Compton wavelength shift," *Phys. Rev. Lett.* 15, 91 (1965).

⁹ J.J. Sanderson, "Corrections to Thomson scattering for intense laser beams," *Phys. Lett.* 18, 114 (1965).

¹⁰ T.W.B. Kibble "Radiative corrections to Thomson scattering from laser beams," *Phys. Lett.* 20, 627 (1966).

¹¹ Joseph H. Eberly and Arthur Sleeper, "Trajectory and mass shift of a classical electron in a radiation pulse," *Phys. Rev.* 176, 1570 (1968).

- ¹² Joseph H. Eberly, "Interaction of very intense light with free electrons," *Progress in Optics*, edited by E. Wolf, (North-Holland, Amsterdam, 1969), Vol. 7.
- ¹³ E.S. Sarachik and G.T. Schappert, "Classical theory of the scattering of intense laser radiation by free electrons," *Phys. Rev. D* 1, 2738 (1970).
- ¹⁴ P.K. Kaw and R. M. Kulsrud, "Relativistic acceleration of charged particles by superintense laser beams," *The Physics of Fluids* 16, 321 (1973).
- ¹⁵ J. Krüger and M. Bovyn, "Relativistic motion of a charged particle in a plane electromagnetic wave with arbitrary amplitude," *J. Phys. A* 9, 1841 (1976).
- ¹⁶ J.N. Bardsley, B.M. Penetrante, and M.H. Mittleman, "Relativistic dynamics of electrons in intense fields," *Phys. Rev. A* 40, 3823 (1989).
- ¹⁷ U. Mohideen, H.W.K. Tom, R.R. Freeman, J. Bokor, and P.H. Bucksbaum, "Interaction of free electrons with an intense focused laser pulse in Gaussian and conical axicon geometries," *J. Opt. Soc. Am. B* 9, 2190 (1992).
- ¹⁸ F.V. Hartemann, S.N. Fochs, G.P. Le Sage, N.C. Luhmann Jr., M.D. Perry, and G.A. Westenskow, "Nonlinear laser electron acceleration in vacuum," *Bull. Am. Phys. Soc.* 39, 1553 (1995).
- ¹⁹ Herbert Goldstein, *Classical Mechanics*, 2nd ed. (Addison-Wesley, Reading Massachusetts, 1980), p. 438.
- ²⁰ P.B. Corkum, N.H. Burnett, and F. Brunel, "Above-threshold ionization in the long-wavelength limit," *Phys. Rev. Lett.* 62, 1259 (1989).
- ²¹ W.B. Mori and T. Katsouleas, "Ponderomotive force of a uniform electromagnetic wave in a time varying dielectric medium," *Phys. Rev. Lett.* 69, 3495 (1992)
- ²² P. B. Corkum, N. H. Burnett and F. Brunel, "Multiphoton ionization in large ponderomotive potentials," *Atoms in Intense Laser Fields* edited by M. Gavrila, (Academic, New York, 1992), p. 109.
- ²³ L.V. Keldysh, "Ionization in the field of a strong electromagnetic wave," *Sov. Phys. JETP* 20, 1307 (1965).
- ²⁴ F.H.M. Faisal, "Multiple absorption of laser photons by atoms," *J. Phys. B* 6, L89 (1973).

- ²⁵ H.R. Reiss, "Effect of an intense electromagnetic field on a weakly bound system," *Phys. Rev. A* 22, 1786 (1980).
- ²⁶ A. L'Huillier, L.A. Lompré, G. Mainfray, and C. Manus, "Multiply charged ions induced by multiphoton absorption processes in rare-gas atoms at 1064 nm," *J. Phys. B* 16, 1363 (1983).
- ²⁷ T.S. Luk, U. Johann, H. Egger, H. Pummer, and C.K. Rhodes, "Collision-free multiple photon ionization of atoms and molecules at 193 nm," *Phys. Rev. A* 32, 214 (1985).
- ²⁸ C.K. Rhodes, "Physical processes at high field strengths," *Phys. Scr.* T17, 193 (1987).
- ²⁹ A. Szöke, "Theory of multiphoton ionization," in *Atomic and Molecular Processes with Short Intense Laser Pulses*, edited by A.D. Bandrauk (Plenum, New York, 1987) p. 207.
- ³⁰ M.D. Perry, A. Szöke, O.L. Landen, and E.M. Campbell, "Nonresonant multiphoton ionization of noble gases: theory and experiment," *Phys. Rev. Lett.* 60, 1270 (1988).
- ³¹ S.L. Chin, C. Rolland, P.B. Corkum, and P. Kelly, "Multiple ionization of Xe and Kr with intense 0.62- μm femtosecond pulses," *Phys. Rev. Lett.* 61, 153 (1988).
- ³² M.D. Perry, O.L. Landen, A. Szöke, and E.M. Campbell, "Multiphoton ionization of the noble gases by an intense 10^{14} -W/cm² dye laser," *Phys. Rev. A* 37, 747 (1988).
- ³³ G. Gibson, T.S. Luk, and C.K. Rhodes, "Tunneling ionization in the multiphoton regime," *Phys. Rev. A* 41, 5049 (1990).
- ³⁴ L.D. Landau and E.M. Lifshitz, *Quantum Mechanics* (Pergamon, New York, 1965).
- ³⁵ B.W. Boreham and J.L. Hughes, "Measurement of ionization threshold intensities in helium using ponderomotive force accelerated electrons," *Zh. Eksp. Teor. Fiz.* 80, (1981) [*Sov. Phys. JETP* 53, 252 (1981)].
- ³⁶ K.G.H. Baldwin and B.W. Boreham, "Investigation of tunneling processes in laser-induced ionization of argon," *J. Appl. Phys.* 52, 2627 (1981).

- ³⁷ M.V. Ammosov, N.B. Delone, and V.P. Krainov, "Tunnel ionization of complex atoms and of atomic ions in an alternating electromagnetic field," *Sov. Phys. JETP* **64**, 1191 (1987).
- ³⁸ F. Yergeau, S.L. Chin, and P. Lavigne, "Multiple ionisation of rare-gas atoms by an intense CO₂ laser (10^{14} W cm⁻²)," *J. Phys. B* **20**, 723 (1987).
- ³⁹ S.L. Chin, W. Xiong, and P. Lavigne, "Creation of multiple charges (up to Xe⁶⁺) from Xe atoms by an intense CO₂ laser," *J. Opt. Soc. Am. B* **4**, 853 (1987).
- ⁴⁰ S.L. Chin and W. Xiong, "Ionization of atoms by an intense CO₂ laser," in *Fundamentals of Laser Interactions II*, edited by F. Ehlotzky (Springer-Verlag, Berlin, 1989), p. 80.
- ⁴¹ S. Augst, D. Strickland, D.D. Meyerhofer, S.L. Chin, and J.H. Eberly, "Tunneling ionization of noble gases in a high-intensity laser field," *Phys. Rev. Lett.* **63**, 2212 (1989).
- ⁴² S. Augst, D.D. Meyerhofer, D. Strickland, and S.L. Chin, "Laser ionization of noble gases by Coulomb-barrier-suppression," *J. Opt. Soc. Am. B.* **8**, 858 (1991).

Chapter 3

Spatial and temporal effects in a laser focus

The experiments described in this thesis use a short pulse 1- μm wavelength laser focused to a 10- μm diameter spot size. This laser field exhibits a strong spatial and temporal dependence. The impact of the field variations on an electron's trajectory is discussed in this chapter.

3.1 The ponderomotive potential

Spatial variations of the field influence electron behavior in a laser focus through an effective potential known as the ponderomotive potential.¹⁻⁷ This potential produces a field-gradient force that pushes electrons from higher to lower intensity regions. Its effects are well documented.⁸⁻¹⁶

In chapter 2, the Hamilton-Jacobi formalism was used to determine an electron's trajectory in a plane wave. This formalism was used due to the extreme simplification of equation (2.1.5) for a plane wave and an obvious form for the action. In a spatially varying field $\vec{A}(\vec{r}, t) \neq A(\eta)$, i.e., space and time no longer occur in the combination $\eta = \omega t - \vec{k} \cdot \vec{r}$ explicitly. Without this dependence, the Hamilton-Jacobi

formalism becomes unnecessarily cumbersome. We therefore use a different technique to examine the effects of spatial field variations.

The traditional and arguably simplest derivation of the ponderomotive potential determines the time-averaged force exerted on the electron directly from the nonrelativistic Lorentz force equation. In terms of the vector potential this force equation is given by

$$m \frac{d\vec{v}(\vec{r}, t)}{dt} = -\frac{e}{c} \left(-\frac{\partial \vec{A}(\vec{r}, t)}{\partial t} + \vec{v}(\vec{r}, t) \times (\vec{\nabla} \times \vec{A}(\vec{r}, t)) \right). \quad (3.1.1)$$

This derivation and all derivations of the ponderomotive potential known to this author make the nonrelativistic assumption that the electron mass is constant or equivalently, $(v_{\text{osc}}/c)^2 \ll 1$.¹⁷ As we shall see, this assumption is unimportant since the stricter condition of $v_{\text{osc}}/c \ll 1$ is also required in the derivation.

Our interest is in electromagnetic fields with a temporal envelope or pulse length much larger than the period of the field ($\omega\tau \gg 1$ where τ is the pulse length).

This field can be written as

$$\vec{A}(\vec{r}, t) = \frac{1}{2} \left(\vec{A}_s(\vec{r}, t) e^{-i\omega t} + \vec{A}_s^*(\vec{r}, t) e^{i\omega t} \right), \quad (3.1.2)$$

where $\vec{A}_s(\vec{r}, t)$ defines the slowly varying portion of the field with the rapid variations at frequency ω extracted and $*$ denotes the complex conjugate. The spatial carrier, $e^{i\vec{k} \cdot \vec{r}}$, is included in the slowly varying function $\vec{A}_s(\vec{r}, t)$. For $e^{i\vec{k} \cdot \vec{r}}$ to be slowly

varying, $e^{i\vec{k}\cdot\vec{r}}$ must remain approximately constant over a cycle of the field or, equivalently, $kz_{\text{osc}} \ll 1$, where k is assumed in the z -direction and z_{osc} is the spatial extent of the oscillations in z . The maximum value of kz_{osc} over a cycle is kv_{osc}/ω . This gives the requirement $v_{\text{osc}}/c \ll 1$.

As was shown in section (2.3), the oscillations in the z -direction are caused by the absorption of momentum from the field. By neglecting the z -oscillations of the electron, we are therefore assuming that electron recoil due to high-intensity Compton scattering is insignificant.

An electron submitted to the vector potential in equation (3.1.2) with $v_{\text{osc}}/c \ll 1$ oscillates rapidly at the field frequency about an average position. The net motion of the average position of the electron is of interest, so we begin by expanding the electron's oscillatory motion about its average position. This expansion requires that the transverse spatial extent of the electron's oscillations be much less than the transverse spatial variation of the field. The zeroth order solution in \vec{r} to equation (3.1.1) is then

$$\vec{r}(\vec{R}, t) = \frac{1}{2}(\vec{x}_{\text{osc}}e^{-i\omega t} + \vec{x}_{\text{osc}}^*e^{i\omega t}) \quad \text{where} \quad \vec{x}_{\text{osc}} = -i \frac{e\vec{A}_s(\vec{R}, t)}{mc\omega}, \quad (3.1.3)$$

and

$$\vec{v}(\vec{R}, t) = \frac{1}{2}(\vec{v}_{\text{osc}}e^{-i\omega t} + \vec{v}_{\text{osc}}^*e^{i\omega t}) \quad \text{where} \quad \vec{v}_{\text{osc}} = \frac{e\vec{A}_s(\vec{R}, t)}{mc}, \quad (3.1.4)$$

and $\bar{\mathbf{R}}$ is the electron's average position vector. $|\bar{\mathbf{x}}_{\text{osc}}|$ is the spatial amplitude of the electron's transverse oscillations at the field frequency. The requirement that the spatial oscillation amplitude be much less than the transverse spatial variation of the field can be written as

$$|\bar{\mathbf{x}}_{\text{osc}}| \ll w_0 \quad \text{or} \quad \frac{v_{\text{osc}}}{c} \ll kw_0$$

where w_0 is the characteristic extent of spatial variations of the field transverse to the propagation direction, such as the spot size of a laser focus. This requirement is already specified by the condition $v_{\text{osc}}/c \ll 1$, since w_0 is at least as large as λ , and therefore $kw_0 > 1$.

We now expand equation (3.1.1) in a Taylor series to first order in $\bar{\mathbf{r}}$ about the average position vector $\bar{\mathbf{R}}$,

$$m \frac{d\bar{\mathbf{v}}(\bar{\mathbf{r}}, t)}{dt} \approx -\frac{e}{c} \left(-\frac{\partial \bar{\mathbf{A}}(\bar{\mathbf{R}}, t)}{\partial t} - (\bar{\mathbf{r}}(\bar{\mathbf{R}}, t) \cdot \bar{\nabla}) \frac{\partial \bar{\mathbf{A}}(\bar{\mathbf{R}}, t)}{\partial t} + \bar{\mathbf{v}}(\bar{\mathbf{R}}, t) \times \bar{\nabla} \times \bar{\mathbf{A}}(\bar{\mathbf{R}}, t) \right). \quad (3.1.5)$$

The partial time derivative of the vector potential is approximately

$$\frac{\partial \bar{\mathbf{A}}(\bar{\mathbf{R}}, t)}{\partial t} \approx \frac{1}{2} \left(-i\omega \bar{\mathbf{A}}_s(\bar{\mathbf{R}}, t) e^{-i\omega t} + i\omega \bar{\mathbf{A}}_s^*(\bar{\mathbf{R}}, t) e^{i\omega t} \right), \quad (3.1.6)$$

where terms from the derivative of the slowly varying envelope of order $1/\tau$ have been dropped since $\omega\tau \gg 1$. After substituting equations (3.1.2)-(3.1.4) and (3.1.6) into equation (3.1.5), we find

$$m \frac{d\vec{v}(\vec{r}, t)}{dt} \approx -\frac{e^2}{4mc^2} \left((\vec{A}_s \cdot \vec{\nabla}) \vec{A}_s^* + \vec{A}_s \times \vec{\nabla} \times \vec{A}_s^* + \text{c.c.} \right) + e^{i\omega t} \text{ terms.} \quad (3.1.7)$$

Only the terms in which the $e^{i\omega t}$ dependence has exactly canceled have been written.

This is because the intention is to find the time-average of the electron's motion. All

terms that retain any $e^{i\omega t}$ dependence will be of order $1/\omega\tau$ after time-averaging. Since

we are considering a slowly varying envelope ($\omega\tau \gg 1$) these terms are small and will

be discarded. The time-average of equation (3.1.7) is

$$m \frac{d\vec{v}(\vec{r}, t)}{dt} = \frac{e^2}{4mc^2} \vec{\nabla} |\vec{A}_s|^2, \quad (3.1.8)$$

where a vector identity¹⁸ has been used to simplify the equation. This is the equation

of motion of a particle in a potential of the form

$$\Phi_p = \frac{e^2 |\vec{A}_s|^2}{4mc^2} = \frac{e^2 \langle \vec{A}^2 \rangle}{2mc^2}, \quad (3.1.9)$$

where Φ_p is the ponderomotive potential. It is equal to the electron's quiver energy in

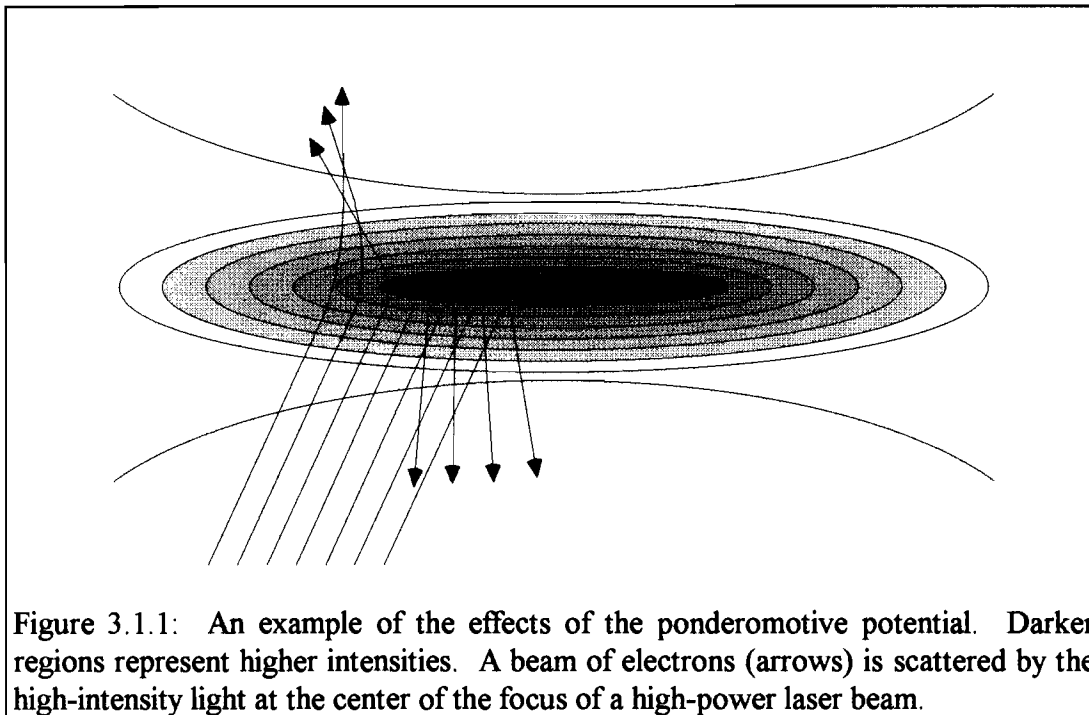
the field (see equation (2.1)). It was first predicted theoretically by Boot and Harvie in

the 1950's.^{1,2} The above derivation is from a review article by Eberly *et al.*¹⁹ An

interesting aspect of this result is that the ponderomotive potential is independent of

the field's polarization.

Figure 3.1.1 shows a simple example of the effects of this potential at the focus of a time-independent (continuous-wave or cw) laser beam. A beam of electrons



travels toward a laser focus with a peak ponderomotive potential greater than the energy of the electrons. As with any potential, energy must be conserved. This results in a deflection of the electrons away from the high intensities at the center of the focus. A very elegant experiment that investigated this simple scattering picture and the effects of a time-dependent pulse on this picture was performed by Bucksbaum *et al.*¹¹

Two assumptions were made in the derivation of the ponderomotive potential:

$$\omega\tau \gg 1,$$

and

$$v_{\text{osc}}/c \ll 1.$$

With respect to the experiments described in this thesis, the first assumption is very accurate since the laser used had over 1000 cycles in a pulse. The second is not. The

consequences of high-intensities, i.e., $q \sim 1$ or $v_{osc}/c \sim 1$, are the subject of this thesis. The question therefore arises, how severely does the breakdown of this assumption affect the validity of the ponderomotive potential? In Chapter 4, this question will be answered by comparing numerical solutions of the electron's fully relativistic equation of motion to the trajectory expected from the ponderomotive potential. These results will show that the ponderomotive potential remains valid for $q \sim 1$ and greater, as long as the forward drift due to high-intensity Compton scattering (see section 2.3) is included in the trajectory. The combination of these two processes will be considered in section 3.3.

3.2 *Electron ejection from a low-intensity laser focus*

The paraxial approximation for the intensity distribution of a Gaussian TEM₀₀ mode laser focus is given by,²⁰

$$I(r, \phi, z) = I_0 \left(\frac{w_0}{w(z)} \right)^2 \exp\left(-2 \frac{r^2}{w^2(z)} \right), \quad (3.2.1)$$

$$w(z) \equiv \sqrt{1 + z^2/z_0^2},$$

where I_0 is the peak intensity, w_0 is the $1/e^2$ radius of the intensity at the beam waist ($z=0$), and z_0 is the Rayleigh range (z position where intensity on laser axis drops by a factor of 2). The diffraction limited values of w_0 and z_0 for a Gaussian TEM₀₀ mode laser beam are,

$$w_0 = \frac{2\lambda f^\#}{\pi}, \quad z_0 = \frac{4\lambda (f^\#)^2}{\pi},$$

where $f^\#$ is the f-number of the focusing system, and is defined as the focal length of the lens divided by the diameter of the beam at the lens. The diameter of the beam is defined as the diameter at which the intensity drops to $1/e^2$ its peak intensity.

The spatial characteristics of the ponderomotive force are given by,

$$\vec{F}_p \propto \left(\frac{w_0}{w(z)} \right)^2 \left[\hat{r} \frac{2r}{w^2(z)} + \hat{z} \frac{z}{z_0^2} \left(\frac{w_0}{w(z)} \right)^2 \left(1 - 2 \left(\frac{r}{w(z)} \right)^2 \right) \right] \exp \left(-2 \left(\frac{r}{w(z)} \right)^2 \right). \quad (3.2.2)$$

Three important features of this force should be noted. The first is the cylindrical symmetry of the force. The second is the symmetry of the force in the axial direction,

$$F_z(z) = -F_z(-z). \quad (3.2.3)$$

The third is the relative size of the forces in the radial and axial directions. The ratio of the force in the axial direction to the force in the radial direction is approximately,

$$\frac{F_z}{F_r} \sim \frac{1}{4f^\#}. \quad (3.2.4)$$

For the laser focus used in these experiments, $f^\# \approx 5$ so that the force in the axial direction is about 20 times smaller than in the radial direction. Electrons are therefore ejected radially at $\theta=90^\circ$ from \vec{k} with a symmetric spread of $\Delta\theta \approx \pm 3^\circ$.

In circular polarization, the ejected electron energy will also be affected by the conservation of canonical momentum described in section 2.1. The momentum of the

electron in a circularly polarized plane wave was shown in equation (2.3.12) to be given by

$$\vec{p}(\eta) = mc \left(\pm \frac{q}{\sqrt{2}} (\hat{x} \sin \eta - \hat{y}(1 - \cos \eta)) + \hat{z} \left(\frac{q^2}{2} - \frac{q^2}{2} \cos \eta \right) \right).$$

The electron has a time-averaged drift in the y-direction,

$$\langle p_y \rangle = \mp \frac{qmc}{\sqrt{2}}. \quad (3.2.5)$$

The y-dependence of this drift is a result of the phase ($\eta=0$) chosen for release of the electron. In circular polarization, an electron is equally likely to be released at any phase of the field (see section 2.3). This allows the electron to be released when the vector potential is rotated in any direction. Since the initial direction of the vector potential defines the direction of the initial canonical momentum, the electron is equally likely to drift in any direction in the plane of polarization.

The energy associated with the canonical momentum drift in circular polarization (see equation (2.1.20)) is equal to the electron's ponderomotive energy,

$$E_D = \frac{e^2 \tilde{A}^2(0)}{2mc^2} = \frac{e^2 \langle \tilde{A}^2 \rangle}{2mc^2} = \Phi_p. \quad (3.2.6)$$

The energy of electrons ejected from a circularly polarized cw laser focus will therefore be $2\Phi_p$: one factor of Φ_p from the ponderomotive acceleration of the electrons, and one factor of Φ_p from the conservation of canonical momentum. The

existence of the drift due to the conservation of canonical momentum in circular polarization has been experimentally verified.²¹

The motion of the electrons due to the conservation of canonical momentum drift is not purely radial near the focus as is the case for the cylindrically symmetric ponderomotive acceleration. For example, consider an electron released at the beam waist ($z=0$), w_0 away from the beam axis in the x -direction, with a canonical momentum drift in the $+y$ direction (see Figure 3.2.1). This electron's

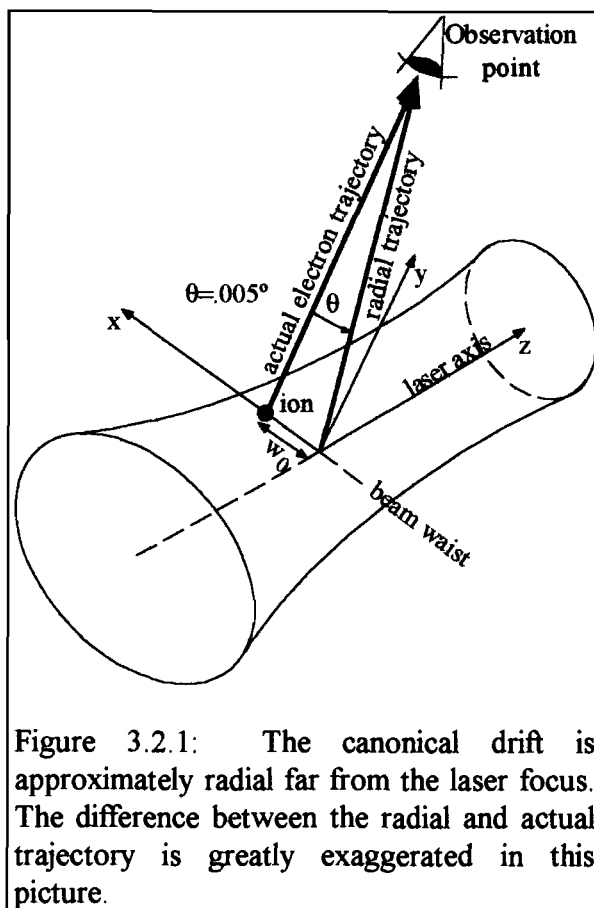


Figure 3.2.1: The canonical drift is approximately radial far from the laser focus. The difference between the radial and actual trajectory is greatly exaggerated in this picture.

trajectory is described by $\vec{r} = w_0\hat{x} + v_d t\hat{y}$. The electron is not traveling purely radially.

The experiments described in this thesis have examined the electron distributions 6 cm from a focus with $w_0 \approx 5 \mu\text{m}$. This means that the electron has traveled from

$\vec{r} = w_0\hat{x}$ to $\vec{r} = w_0\hat{x} + r_{\text{obs}}\hat{r}$, where r_{obs} is the observation distance of 6 cm. If we

assume that the electron is traveling purely radially throughout its trajectory, it would

travel from $\vec{r} = 0$ to $\vec{r} = r_{\text{obs}}\hat{r}$. The angular difference between these two vectors is

0.005° due to the large distance of observation compared to the electron's relatively small offset from the center of the focus. We therefore introduce very little error if the electron's motion is approximated as radial.

Circular polarization is used in our experiments to assure a cylindrically symmetric distribution of ejected electrons. The experiments involve the ionization of many atoms ($n \sim 10^5 - 10^7$) randomly distributed throughout a circularly polarized laser focus. Each ionized electron experiences a drift due to the conservation of canonical momentum and an acceleration from the ponderomotive potential. The drift depends on the phase of the field at which the electron is ionized. This phase will be different for each electron, and the net result will be an isotropic distribution in the plane of polarization for circular polarization. The direction of the ponderomotive acceleration depends on the initial position of the electron. The random distribution of electrons causes the distribution from the ponderomotive acceleration to be isotropic in the plane of polarization. Therefore, the combined effects of the ponderomotive acceleration and the conservation of canonical momentum drift for circular polarization at low intensities gives a uniform distribution of electrons in the plane of polarization, i.e., at 90° to the laser axis. These electrons travel approximately radially with twice the ponderomotive energy of the intensity at which they were born.

3.3 *Electron ejection from a high-intensity laser focus*

The analysis of the ponderomotive potential for a low-intensity Gaussian focus shows that electrons are emitted isotropically in the plane of polarization. At high intensities, the absorption of momentum from the field (see section 2.3) “pushes” the electron distribution forward so that electrons are emitted in a cone centered on \vec{k} . The angle from \vec{k} is given by the relationship between the forward component and the total momentum of the electron.

We begin calculating this angle by assuming that an electron is ejected from the laser focus with arbitrary energy E (including rest mass energy). As was previously shown in section 2.3, this energy must come from the laser field, which means the electron must also absorb momentum from the field,²²

$$\Delta p_z = \frac{\Delta E}{c} = \frac{E}{c} - mc = mc(\gamma - 1) \quad (3.3.1)$$

where

$$\gamma = \frac{E}{mc^2} = \frac{1}{\sqrt{1 - \vec{v}^2/c^2}}.$$

The electron’s total momentum is

$$\vec{p}^2 = \frac{E^2}{c^2} - m^2 c^2 = m^2 c^2 (\gamma^2 - 1). \quad (3.3.2)$$

From these we can determine the angle of ejection of the electron,

$$\cos^2 \theta = \left(\frac{\Delta p_z}{|\vec{p}|} \right)^2 = \frac{\gamma - 1}{\gamma + 1} \quad \text{or} \quad \tan^2 \theta = \frac{2}{\gamma - 1}. \quad (3.3.3)$$

This angle (see Figure 3.3.1)

is a function of the final energy of the electron only.

The only assumptions made

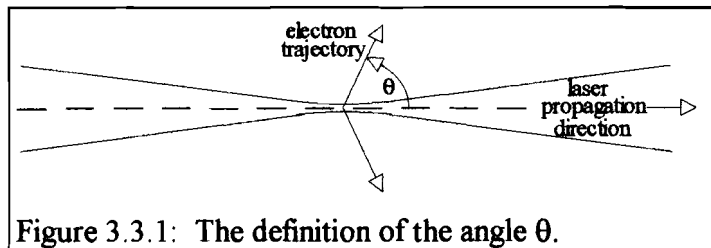


Figure 3.3.1: The definition of the angle θ .

were that all available momentum in the field was in the z direction, and only the electromagnetic field accelerates the electron.

3.4 The effects of a time-dependent pulse

An electron's ejection energy following ionization in a laser focus is dependent on the intensity at which it was ionized and the polarization of the field. An electron born at the peak of the field in a linearly polarized cw beam has zero initial canonical momentum and a potential energy given by the ponderomotive potential of the ionization threshold intensity. Subsequent acceleration by the ponderomotive potential converts the electron's ponderomotive quiver energy to kinetic translational energy. The electron is therefore ejected with the ponderomotive energy of the ionization threshold intensity. In a circularly polarized cw beam, an electron is released into the field with non-zero initial canonical momentum and a potential energy given by the ponderomotive potential of the ionization threshold intensity. Conservation of canonical momentum causes the electron to drift in the direction of the initial canonical

momentum. The energy contributed by this drift is exactly equal to the ponderomotive energy. In addition, the conversion of the ponderomotive quiver energy to translational energy gives the electron another factor of the ponderomotive energy. An electron born in circular polarization therefore acquires an energy of twice the ponderomotive potential of the ionization intensity.

In a pulsed laser, the intensity is time-dependent, and the corresponding ponderomotive potential is a time-dependent potential. Conservation of energy (required for a time-independent potential) no longer applies. The energy of an electron ejected from a laser focus by a time-dependent pulse is¹¹

$$E = \kappa \Phi_p(\vec{r}(t_0), t_0) + \int_{t_0}^{\infty} \frac{\partial \Phi_p(\vec{r}(t), t)}{\partial t} dt \quad (3.4.1)$$

where t_0 is the time at which the electron is ionized, κ is defined as one in linear polarization and two in circular polarization, and the ponderomotive potential is assumed to be zero at infinite time. The integral in equation (3.4.1) is the change in the electron's energy due to the time-dependent ponderomotive potential.

In the limit of long pulses, the partial differential in equation (3.4.1) will be approximately zero since the electron will leave the intense regions of the field before the slowly-varying temporal aspect of the pulse contributes to the differential. This will cause the contribution of the integral in equation (3.4.1) to be small or,

$$E \approx \kappa \Phi_p(\vec{r}(t_0), t_0). \quad (3.4.2)$$

The electron will therefore gain the full ponderomotive energy, and the pulse can be closely approximated as cw.

For extremely short laser pulses, the electron will not move before the pulse has passed. $\vec{r}(t)$ can therefore be approximated as constant, and the partial differential in equation (3.4.1) can be approximated by a total differential or,

$$E \approx (\kappa - 1) \Phi_p(\vec{r}(t_0), t_0). \quad (3.4.3)$$

In very short pulses, the electrons will therefore gain no energy from the field in linear polarization, and only the energy from the conservation of canonical momentum in circular polarization, i.e., Φ_p , not $2\Phi_p$ as in the cw case.

We are interested in discovering the pulse width necessary to enter the long pulse limit, i.e., the pulse width that allows full acquisition of the ponderomotive energy. For a Gaussian temporal and spatial profile laser pulse,

$$\Phi_p(\vec{r}(t), t) \propto \left(\frac{w_0}{w(z)} \right)^2 \exp\left(-2 \frac{r^2}{w^2(z)}\right) \exp\left(-\ln 2 \left(\frac{t - \frac{z}{c}}{\frac{\tau}{2}} \right)^2\right) \quad (3.4.4)$$

and

$$\frac{\partial \Phi_p(\vec{r}(t), t)}{\partial t} = -8 \ln 2 \left(\frac{t - \frac{z}{c}}{\tau^2} \right) \Phi_p(\vec{r}(t), t), \quad (3.4.5)$$

where τ is the FWHM pulse width. Equation (3.4.1) can now be approximated as

$$E \sim \left(\kappa - \frac{8 \ln 2}{\tau} \Delta t \right) \Phi_p(\vec{r}(t_0), t_0), \quad (3.4.6)$$

where Δt is the interaction time of the electron with the field. The interaction time can be approximated by the time the electron takes to travel w_0 , or $\Delta t \approx w_0/\bar{v}$ where \bar{v} is the average velocity of the electron. Therefore equation (3.4.6) becomes

$$E \sim \left(\kappa - \frac{8 \ln 2}{\tau} \frac{w_0}{\bar{v}} \right) \Phi_p(\vec{r}(t_0), t_0). \quad (3.4.7)$$

For pulse duration effects to be small, we must have,

$$\kappa \gg \frac{8 \ln 2}{\tau} \frac{w_0}{\bar{v}}. \quad (3.4.8)$$

The condition imposed on the pulse width for linear polarization is then

$$\tau \gg 8 \ln 2 \frac{w_0}{\bar{v}}, \quad (3.4.9)$$

and for circular polarization,

$$\tau \gg 4 \ln 2 \frac{w_0}{\bar{v}}. \quad (3.4.10)$$

The laser conditions used in these experiments were a circularly polarized 1.053- μm wavelength laser with a 1.5-ps FWHM pulse width and a 5- μm beam waist. The maximum value of the right side of equation (3.4.10) is obtained for the lowest energy electrons studied since these have the smallest average velocity. The lowest

energy electrons studied had an energy of 3 keV. These have an approximate average velocity of $0.09c$, which gives the requirement,

$$\tau \gg 0.5 \text{ ps.} \quad (3.4.11)$$

This is only weakly satisfied by the 1.5-ps pulse width of the laser used. However, the numerical integration of the electron trajectories in Chapter 4 will show that this is sufficient for pulse effects to be minimal in the experiment.

The effects described so far have assumed that the relativistic, pulse envelope and spatial effects can be considered independently and combined later. The next chapter will test the validity of these assumptions by numerically integrating the electron's relativistic equation of motion in a Gaussian focus, and comparing these results with those expected from the independent analytic treatment of spatial, temporal, and relativistic effects.

¹ H.A.H. Boot and R.B. R.-S.-Harvie, "Charged particles in a non-uniform radio-frequency field," *Nature* 180, 1187 (1957).

² H.A.H. Boot, S.A. Self, and R.B. R.-Shersby-Harvie, "Containment of a fully-ionized plasma by radio-frequency field," *J. Electr. Control* 4, 434(1958).

³ A. V. Gaponov and M. A. Miller, "Potential wells for charged particles in a high-frequency electromagnetic field," *J. Exptl. Theoret. Phys. (U.S.S.R.)* 34, 242 (1958) [*Soviet Phys. JETP* 7, 168 (1958)].

⁴ G.A. Askar'yan, "Effects of the gradient of a strong electromagnetic beam on electrons and atoms," *J. Exptl. Theoret. Phys. (U.S.S.R.)* 42, 1567 (1962) [*Soviet Phys. JETP* 15, 1088 (1962)].

- ⁵ T.W.B. Kibble, "Refraction of electron beams by intense electromagnetic waves," *Phys. Rev. Lett.* 16, 1054 (1966).
- ⁶ T.W.B. Kibble, "Mutual refraction of electrons and photons," *Phys. Rev.* 150, 1060 (1966).
- ⁷ W.B. Mori and T. Katsouleas, "Ponderomotive force of a uniform electromagnetic wave in a time varying dielectric medium," *Phys. Rev. Lett.* 69, 3495 (1992).
- ⁸ M.J. Hollis, "Multiphoton ionization and EM field gradient forces," *Optics Communications* 25, 395 (1978).
- ⁹ M.T. Bachelor and R.J. Stening, *Laser Part. Beams* 3, 189 (1985).
- ¹⁰ R.R. Freeman, T.J. McIlrath, P.H. Bucksbaum, and M. Bashkansky, "Ponderomotive effects on angular distributions of photoelectrons," *Phys. Rev. Lett.* 57, 3156 (1986).
- ¹¹ P.H. Bucksbaum, M. Bashkansky, and T.J. McIlrath, "Scattering of electrons by intense coherent light," *Phys. Rev. Lett.* 58, 349 (1987).
- ¹² R.R. Freeman, P.H. Bucksbaum, H. Milchberg, S. Darack, D. Schumacher, and M.E. Geusic, "Above-Threshold Ionization with subpicosecond laser pulses," *Phys. Rev. Lett.* 59, 1092 (1987).
- ¹³ T.F. Gallagher, "Above-Threshold Ionization in low-frequency limit," *Phys. Rev. Lett.* 61, 2304 (1988).
- ¹⁴ M.D. Perry, O.L. Landen, and A. Szöke, "Measurement of the local laser intensity by photoelectron energy shifts in multiphoton ionization," *J. Opt. Soc. Am. B* 6, 344 (1989).
- ¹⁵ P. Monot, T. Auguste, L.A. Lompré, G. Mainfray, and C. Manus, "Energy measurements of electrons submitted to an ultrastrong laser field," *Phys. Rev. Lett.* 70, 1232 (1993).
- ¹⁶ U. Mohideen, M.H. Sher, H.W.K. Tom, G.D. Aumiller, O.R. Wood II, R.R. Freeman, J. Bokor, and P.H. Bucksbaum, "High intensity Above-Threshold Ionization of He," *Phys. Rev. Lett.* 71, 509 (1993).

¹⁷ It should be noted that the ponderomotive potential derivation performed in ref. 6 uses relativistic four-vector notation. However, this derivation is also nonrelativistic since the requirement $\mu^2 \ll 1$ stated in the paper is equivalent to $(v_{\text{osc}}/c)^2 \ll 1$.

¹⁸ J.D. Jackson, *Classical Electrodynamics* 2nd ed., (Wiley, New York, 1975).

¹⁹ J.H. Eberly, J. Javanainen, K. Rzazewski, "Above-Threshold Ionization," *Phys. Reports* 204, 331 (1991).

²⁰ Peter W. Milonni and Joseph H. Eberly, *Lasers* (Wiley, New York, 1988), p.484-490.

²¹ P.B. Corkum, N.H. Burnett, and F. Brunel, "Above-threshold ionization in the long-wavelength limit," *Phys. Rev. Lett.* 62, 1259 (1989).

²² P.B. Corkum, N.H. Burnett and F. Brunel, "Multiphoton ionization in large ponderomotive potentials," *Atoms in Intense Laser Fields* edited by M. Gavrila, (Academic, New York, 1992), p. 109.

Chapter 4

Numerical simulation of electron dynamics in a focused laser field

The previous chapters have treated spatial, temporal, and relativistic effects independently. The validity of independent treatment of these effects is tested in this chapter by numerically integrating the covariant Lorentz force equation for an electron in a spatially and temporally varying field,¹

$$m \frac{dU^\alpha}{d\tau} = -\frac{e}{c} (\partial^\alpha A^\beta - \partial^\beta A^\alpha) U_\beta = -\frac{e}{c} F^{\alpha\beta} U_\beta, \quad (4.1)$$

where $F^{\alpha\beta}$ is the electromagnetic field-strength tensor,

$$F^{\alpha\beta} = \begin{pmatrix} 0 & -\mathcal{E}_x & -\mathcal{E}_y & -\mathcal{E}_z \\ \mathcal{E}_x & 0 & -B_z & B_y \\ \mathcal{E}_y & B_z & 0 & -B_x \\ \mathcal{E}_z & -B_y & B_x & 0 \end{pmatrix},$$

U^α is the four-velocity,

$$U^\alpha = (\gamma c, \gamma \vec{v}),$$

and $\vec{\mathcal{E}}$ and \vec{B} give the complete temporal and spatial description of the focused laser field, including the dependence on $e^{i\omega t}$ and $e^{i\vec{k} \cdot \vec{r}}$.

4.1 The paraxial approximation for a Gaussian laser focus

Accurate descriptions of the electric and magnetic fields are required to numerically integrate equation (4.1). The paraxial approximation for the electric field of a Gaussian continuous wave (cw) laser focus with \vec{k} in the z-direction is²

$$\vec{\mathcal{E}}_{\text{cw}} = \hat{\epsilon} \mathcal{E}_0 \frac{w_0}{w(z)} \exp(i(\Phi(r, z) - \omega t)) \exp\left(-\left(\frac{r}{w(z)}\right)^2\right) + \text{c.c.}, \quad (4.1.1)$$

where

$$w(z) \equiv w_0 \sqrt{1 + (z/z_0)^2} \quad (\text{beam radius at } z),$$

$$R(z) \equiv z + z_0^2/z \quad (\text{radius of curvature at } z),$$

$$\Phi(r, z) \equiv kz - \tan^{-1}\left(\frac{z}{z_0}\right) + \frac{kr^2}{2R(z)} \quad (\text{time-independent phase}),$$

$\hat{\epsilon}$ is a complex unit vector in the plane perpendicular to the propagation direction that specifies the polarization, and \mathcal{E}_0 is the peak amplitude of the field. The electric field for a pulsed laser with a Gaussian temporal profile is described by multiplying by another Gaussian,

$$\vec{\mathcal{E}}_t = \vec{\mathcal{E}}_{\text{cw}} \exp\left(-2 \ln 2 \left(\frac{\Phi(r, z) - \omega t}{\omega \tau}\right)^2\right) + \text{c.c.} \quad (4.1.2)$$

where τ is the FWHM of the pulse in intensity and $\vec{\mathcal{E}}_t$ is a transverse electric field. Use of $\Phi(r, z)$ in equation (4.1.2) causes the propagation of the pulse in the proper

direction, i.e., perpendicular to the phase fronts. The corresponding magnetic field can be found using Faraday's law,

$$\vec{\nabla} \times \vec{\mathcal{E}} + \frac{1}{c} \frac{\partial \vec{B}}{\partial t} = 0. \quad (4.1.3)$$

The standard approximations of long pulse width ($\omega\tau \gg 1$) and transverse electric and magnetic fields gives

$$\vec{B}_t \approx \hat{z} \times \vec{\mathcal{E}}_t \quad (\vec{k} \text{ assumed in } z \text{ direction}). \quad (4.1.4)$$

The electron trajectories calculated with these transverse electric (equation (4.1.2)) and magnetic (equation (4.1.4)) fields have a polarization dependence in contradiction with the ponderomotive potential (see section 3.2).

To demonstrate, consider a linearly polarized electromagnetic field ($\hat{\epsilon} = \hat{x}$),

$$\vec{\mathcal{E}}(\vec{r}, t) = |\vec{\mathcal{E}}_t(\vec{r}, t)| \hat{x}$$

and

$$\vec{B}(\vec{r}, t) = |\vec{\mathcal{E}}_t(\vec{r}, t)| \hat{y}. \quad (4.1.5)$$

We can write the equation of motion for the electron, equation 4.1, to the same order of the ponderomotive potential as

$$m \frac{d\vec{v}}{dt} = -e |\vec{\mathcal{E}}_t(\vec{r}, t)| \left(\left(1 - \frac{v_z}{c} \right) \hat{x} + \frac{v_x}{c} \hat{z} \right). \quad (4.1.6)$$

There is no component of acceleration in the y-direction. This results in a polarization dependence in contradiction to the ponderomotive potential.

4.2 The longitudinal field of a Gaussian focus

The polarization dependence is caused by the failure of the standard paraxial approximation for the electric and magnetic fields (correct to zeroth order in $1/f^\#$) to obey Maxwell's equations to the same order as assumed in the derivation of the ponderomotive potential (first order in $1/f^\#$). We must therefore find first order corrections to the paraxial electric and magnetic fields.

The first order correction to the paraxial electric field is found from the requirement that $\bar{\nabla} \cdot \bar{\mathcal{E}} = 0$.³ The divergence of the electric field in equation (4.1.2) is not equal to zero as required by Maxwell's equation. The first order correction is found by substituting the transverse electric field in equation (4.1.2) into $\bar{\nabla} \cdot \bar{\mathcal{E}} = 0$ and solving for a longitudinal field (z component of $\bar{\mathcal{E}}$) that satisfies $\bar{\nabla} \cdot \bar{\mathcal{E}} = 0$,

$$\frac{\partial \mathcal{E}_z}{\partial z} = -\bar{\nabla}_t \cdot \bar{\mathcal{E}}_t, \quad (4.2.1)$$

where $\bar{\nabla}_t = \partial/\partial x \hat{x} + \partial/\partial y \hat{y}$. We now make the approximation

$$\frac{\partial \mathcal{E}_z}{\partial z} \approx ik \mathcal{E}_z, \quad (4.2.2)$$

which is valid to first order in $1/f^\#$. This approximation and the paraxial approximation for the electric field in equation (4.1.2) give the solution to equation (4.2.1) as,

$$\mathcal{E}_z \approx -\bar{\mathcal{E}}_t \cdot \left[(2x\hat{x} + 2y\hat{y}) \left(\frac{i}{k(w(z))^2} + \frac{1}{R(z)} \right) \right]. \quad (4.2.3)$$

This equation for the longitudinal electric field, along with the transverse electric field in equation (4.1.2), satisfies $\vec{\nabla} \cdot \vec{\mathcal{E}} = 0$ to first order in $1/f^\#$. The first-order solution to the electric field is used in Faraday's law (equation (4.1.3)) to find the magnetic field. With the assumption that $\omega\tau \gg 1$, the magnetic field to first order in $1/f^\#$ is

$$\vec{B}_t \approx \hat{z} \times \vec{\mathcal{E}}_t \quad (4.2.4)$$

and

$$B_z = -\vec{B}_t \cdot \left[(2x\hat{x} + 2y\hat{y}) \left(\frac{i}{k(w(z))^2} + \frac{1}{R(z)} \right) \right]. \quad (4.2.5)$$

These expressions for the electric and magnetic fields give the expected results of polarization independence for the electron trajectories. This first order approximation in $1/f^\#$ is sufficient for the $f/5$ optics used in our experiments.

4.3 Monte Carlo simulation of electron ejection from a high-intensity, Gaussian laser focus

A Monte Carlo simulation computer program of the laser ionization and subsequent acceleration of electrons under the relativistic equations of motion has been written (see appendix A). The program models the propagation of a laser with a Gaussian spatial and temporal profile through a focus containing randomly distributed noble gas atoms.

The simulation begins by reading various experimental parameters from a data file. The experimental parameters used in the program include: the peak intensity, pulse width, focal spot characteristics, and polarization of the laser pulse; the noble gas to be studied; the noble gas pressure; and the initial charge state and number of atoms of the noble gas to be examined.

The program calculates the critical electric field necessary to ionize the initial charge state using BSI⁴ (see section 2.3),

$$\mathcal{E}_{\text{crit}} = \frac{E_{\text{ion}}^2}{4Ze^3}. \quad (4.3.1)$$

where E_{ion} is the ionization potential of the charge state and Z is the ionic charge. Ionization occurs in the BSI approximation when the electric field reaches the critical electric field defined in equation (4.3.1). The peak electric field in linear polarization is $\sqrt{2}$ larger than the peak electric field in circular polarization at the same intensity. This causes ionization to occur with linear polarization at half the intensity required with circular polarization. The threshold intensities are,

$$I_{\text{th}}(\text{W}/\text{cm}^2) = 4 \times 10^9 \frac{E_{\text{ion}}^4(\text{eV})}{Z^2} \quad \text{for linear polarization}$$

and

$$I_{\text{th}}(\text{W}/\text{cm}^2) = 8 \times 10^9 \frac{E_{\text{ion}}^4(\text{eV})}{Z^2} \quad \text{for circular polarization.}$$

The threshold intensity is used to calculate the volume within the focus (focal volume) where ionization will occur.⁵ An atom is then placed at a random position within the focal volume. The Gaussian temporal envelope, ignoring the phase, is used to solve for the time at which the electron experiences an intensity equal to the BSI threshold intensity. In circular polarization, this time was used as the starting point for when the electron was considered free of the atom. In linear polarization, it is assumed that the electron will be released at the peak of the electric field. Therefore, the program waits from the time determined by the Gaussian temporal envelope to a time within a half cycle when the field is peaked.

In both circular and linear polarization, the electron is assumed born at rest.⁶ The electron then experiences the electromagnetic field found above, and its trajectory is calculated using a 5th order Cash-Harp Runge-Kutta method to integrate equation (4.1).⁷ The electron trajectory is calculated until the intensity drops six orders of magnitude below the ionization threshold intensity.

The electron's position and velocity vectors are then stored in a data file, and a new atom is placed within the focus at another random position. This process continues until the specified number of atoms to be studied is reached. At this point, the program calculates the intensity necessary for ionization of the next higher charge state using BSI. If the threshold intensity is below the peak laser field intensity, the above process is repeated. This continues until the atom is completely ionized, or until

the peak laser intensity specified in the input file is below the intensity necessary for ionization of the next charge state. When this occurs, the program has calculated all electron trajectories and ends.

Ne	E_{ion}	I_{th} in lin.	$E_{\text{lin}}=\Phi_p(I_{\text{th}})$	τ_{lin}
1 ⁺	21.6 eV	8.71×10^{14} W/cm ²	90.1 eV	10 ps
2 ⁺	41.0	2.83×10^{15}	293 eV	5.5 ps
3 ⁺	63.5	7.23×10^{15}	748 eV	3.4 ps
4 ⁺	97.1	2.22×10^{16}	2.30 keV	2.0 ps
5 ⁺	126	4.03×10^{16}	4.17 keV	1.5 ps
6 ⁺	158	6.92×10^{16}	7.16 keV	1.1 ps
7 ⁺	207	1.50×10^{17}	15.5 keV	770 fs
8 ⁺	239	2.04×10^{17}	21.1 keV	660 fs

Table 1: Ionization potentials, E_{ion} , BSI threshold intensities, I_{th} in lin., and ejection energies, E_{lin} , for laser pulses much longer than τ_{lin} in linear polarization.

The dynamics of the electrons freed in creating Ne¹⁺ to Ne⁸⁺ were calculated for a variety of experimental conditions. The ionization potentials, BSI threshold intensities, expected ejection energies, and interaction times (see section 3.4) of electrons from Ne¹⁺ to Ne⁸⁺ are shown for linear polarization in Table 1, and for circular polarization in

Table 2. The ejection energies are the energies expected for laser pulse lengths much longer than the interaction time of the electron with the field.

Ne	E_{ion}	I_{th} in circ.	$E_{\text{circ}}=2\Phi_p(I_{\text{th}})$	τ_{circ}
1 ⁺	21.6 eV	1.74×10^{15} W/cm ²	360. eV	1.4 ps
2 ⁺	41.0	5.65×10^{15}	1.17 keV	800 fs
3 ⁺	63.5	1.45×10^{16}	3.00 keV	500 fs
4 ⁺	97.1	4.44×10^{16}	9.19 keV	290 fs
5 ⁺	126	8.07×10^{16}	16.7 keV	220 fs
6 ⁺	158	1.38×10^{17}	28.6 keV	170 fs
7 ⁺	207	3.00×10^{17}	62.1 keV	120 fs
8 ⁺	239	4.08×10^{17}	84.4 keV	110 fs

Table 2: Ionization potentials, E_{ion} , BSI threshold intensities, I_{th} in circ., and ejection energies, E_{circ} , in laser pulses much longer than τ_{circ} in circular polarization.

In the discussion that follows, all calculations use a 1.053- μm wavelength Gaussian profile laser focused to a diffraction-limited 5- μm spot size and a peak intensity of 10^{18} W/cm^2 .

Electrons ionized in a long-pulse, linearly polarized laser are expected to acquire an energy equal to the ponderomotive potential of their BSI threshold intensity. Figure 4.3.1a shows the electron energy spectrum of Ne^{3+} to Ne^{8+} ionized with a 1-ns pulse length ($\tau_{\text{laser}} \gg \tau_{\text{lin}}$) linearly polarized laser. The electron energy spectrum exhibits peaks at the ponderomotive energies corresponding to the different threshold intensities of the neon charge states. This is expected since the long pulse length allows the ponderomotive potential to behave as a time-independent potential, and energy is conserved.

Figure 4.3.1b shows the energy spectrum for a 50 fs, linearly polarized laser pulse. In this case, the pulse length is much shorter than τ_{lin} and the ponderomotive potential is no longer a conservative potential. The time-dependence of the pulse causes a wide range of ejected electron energies and no individual peaks are discernible.

In long-pulse circularly polarized laser fields, electrons with energies of four times those found for the same charge states in linear polarization are expected. This

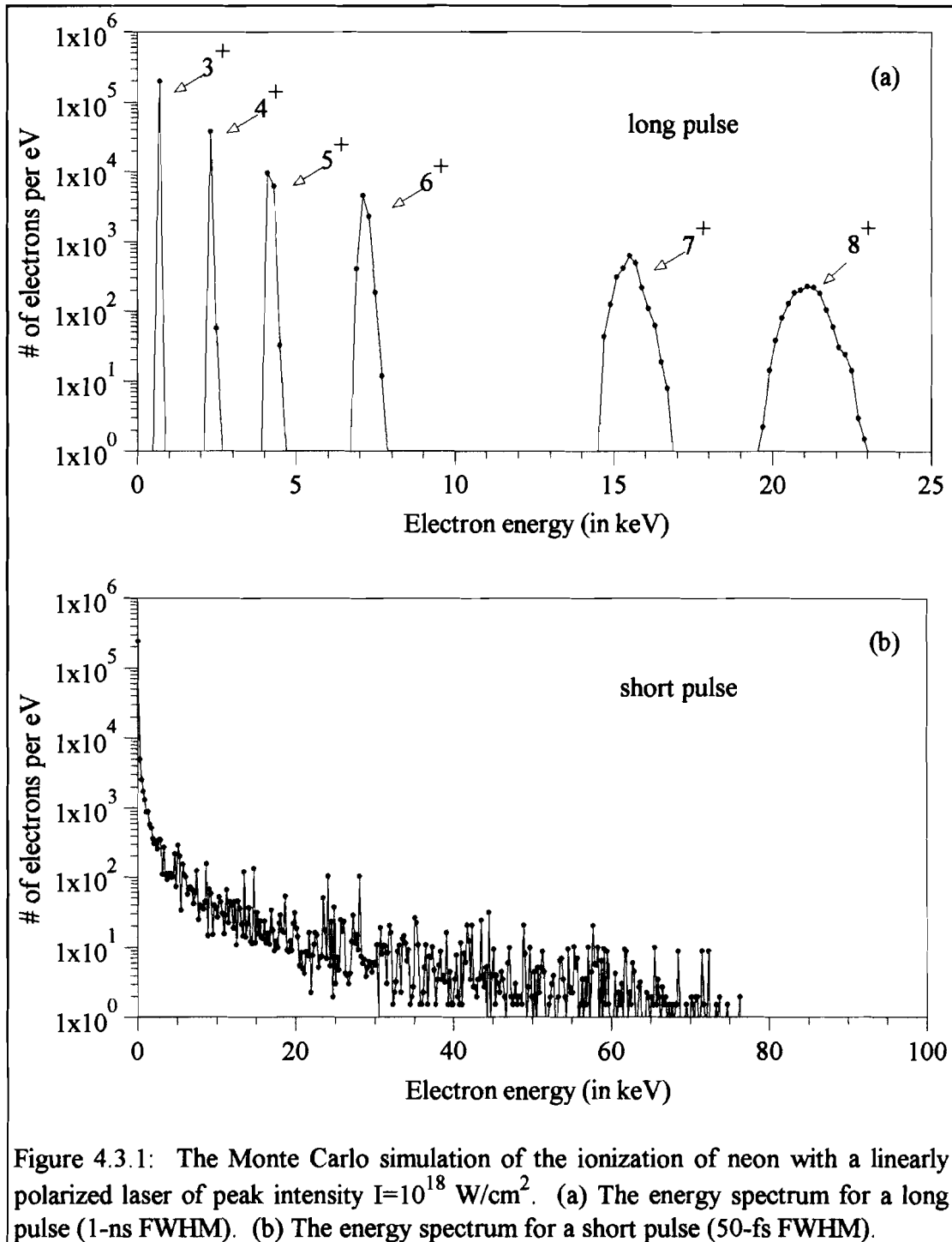


Figure 4.3.1: The Monte Carlo simulation of the ionization of neon with a linearly polarized laser of peak intensity $I=10^{18}$ W/cm². (a) The energy spectrum for a long pulse (1-ns FWHM). (b) The energy spectrum for a short pulse (50-fs FWHM).

occurs due to two factors. The first is because the ponderomotive potential is twice as high for the same charge state in circular polarization as in linear polarization due to the doubling of the BSI threshold intensity. The second is due to the conservation of canonical momentum described in section 2.2. This contributes a second factor of the ponderomotive potential.

Figure 4.3.2a shows the electron energy spectrum for Ne^{3+} to Ne^{8+} ionized with a 1-ns pulse length ($\tau_{\text{laser}} \gg \tau_{\text{circ}}$) circularly polarized laser. The electrons gain twice the ponderomotive energy of the circular polarization BSI threshold intensities of the neon charge states. This shows that the ponderomotive potential predicts the correct energy, even for relativistic electrons. $\gamma \approx 1.2$ for the 80-keV electrons. The electrons are experiencing a slight mass increase due to the deviation of γ from 1, but the ponderomotive potential predictions are unaffected and still give the correct results. Monte Carlo simulations of electrons ionized at intensities up to $I = 10^{20}$ W/cm^2 ($\Phi_p \approx 10 \text{ MeV}$; $\gamma \approx 20$) confirm that this agreement continues into the highly relativistic regime.

Figure 4.3.2b shows the energy spectrum of a 50-fs pulse length circularly polarized laser. The pulse length is now shorter than the interaction time, and the lower charge state electrons exhibit half the energy of the long pulse case. This occurs

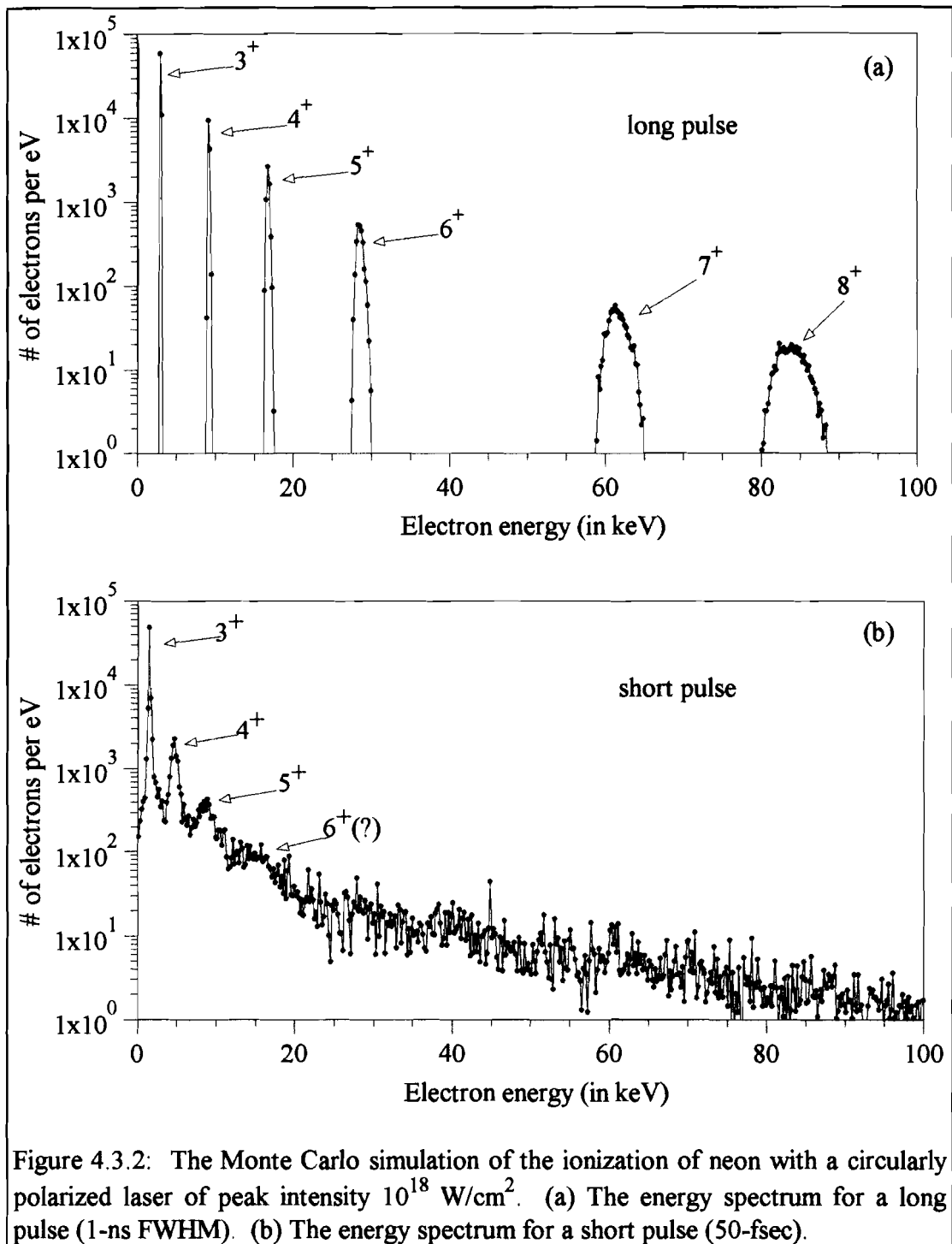


Figure 4.3.2: The Monte Carlo simulation of the ionization of neon with a circularly polarized laser of peak intensity 10^{18} W/cm². (a) The energy spectrum for a long pulse (1-ns FWHM). (b) The energy spectrum for a short pulse (50-fsec).

because energy is only acquired due to the conservation of canonical momentum, which is gained immediately following ionization. The pulse length is too short for electrons to gain the slowly developing ponderomotive energy. The higher charge state electrons are in the intermediate region between the long pulse case and the short pulse case. These electrons' interaction times are approximately twice the pulse width. This results in the acquisition of a range of energies depending on their initial placement within the laser focus. The electrons with 100-keV energies are “surfing”⁸ on the leading temporal edge of the laser pulse and gaining energies greater than $2\Phi_p$. Other electrons experience very little acceleration beyond the canonical momentum drift, or possibly even decelerate due to surfing on the trailing edge of the laser pulse. The net effect of the wide range of possible energies for the same charge state is to “wash-out” the peaks of the high charge states.

The pulse length of the laser used in the experiments reported here is approximately 1.5 psec. The expected spectrum of Ne^{3+} and higher charge states for linear polarization is shown in Figure 4.3.3a. The electrons here behave much as they did in the linearly polarized 50-fs pulse (see Figure 4.3.1b). The electron peaks that were visible in the long-pulse case are not present because the interaction time (from 700 fs for the highest energy electrons, to 3.5 ps for the lowest energy electrons) is similar to the pulse length. The energy spectrum of linear polarization has not been measured experimentally.

The case of circular polarization in Figure 4.3.3b exhibits electron peaks similar to those seen for the long-pulse case in circular polarization shown in Figure 4.3.2a. The interaction time for circular polarization is approximately 100 fs for the highest energy electrons, and 500 fs for the lowest energy electrons shown. This allows complete conversion of the slowly developing ponderomotive energy into kinetic energy. The energy spectrum in circular polarization has been measured experimentally and agrees well with this expectation. These observations will be discussed in detail in chapter 6.

The neglect of field momentum effects in the derivation of the ponderomotive potential manifests itself in the angular distributions of the ejected electrons at high-intensities. As was discussed in sections 3.2 and 3.3, the ponderomotive potential predicts electron ejection at 90° from \vec{k} , but high-intensity Compton scattering “pushes” the electrons forward of this predicted ejection angle

Figure 4.3.4 shows the Monte Carlo prediction (solid line) of the angular distribution of Ne^{1+} electrons ionized at $1.7 \times 10^{15} \text{ W/cm}^2$ in a 1.5-ps circularly polarized laser pulse. The angular distribution is peaked at 89.1° from \vec{k} . The ejection energy of these electrons in the Monte Carlo simulation is approximately 186 eV. The prediction of equation (3.3.3), which determines the angle of ejection based on

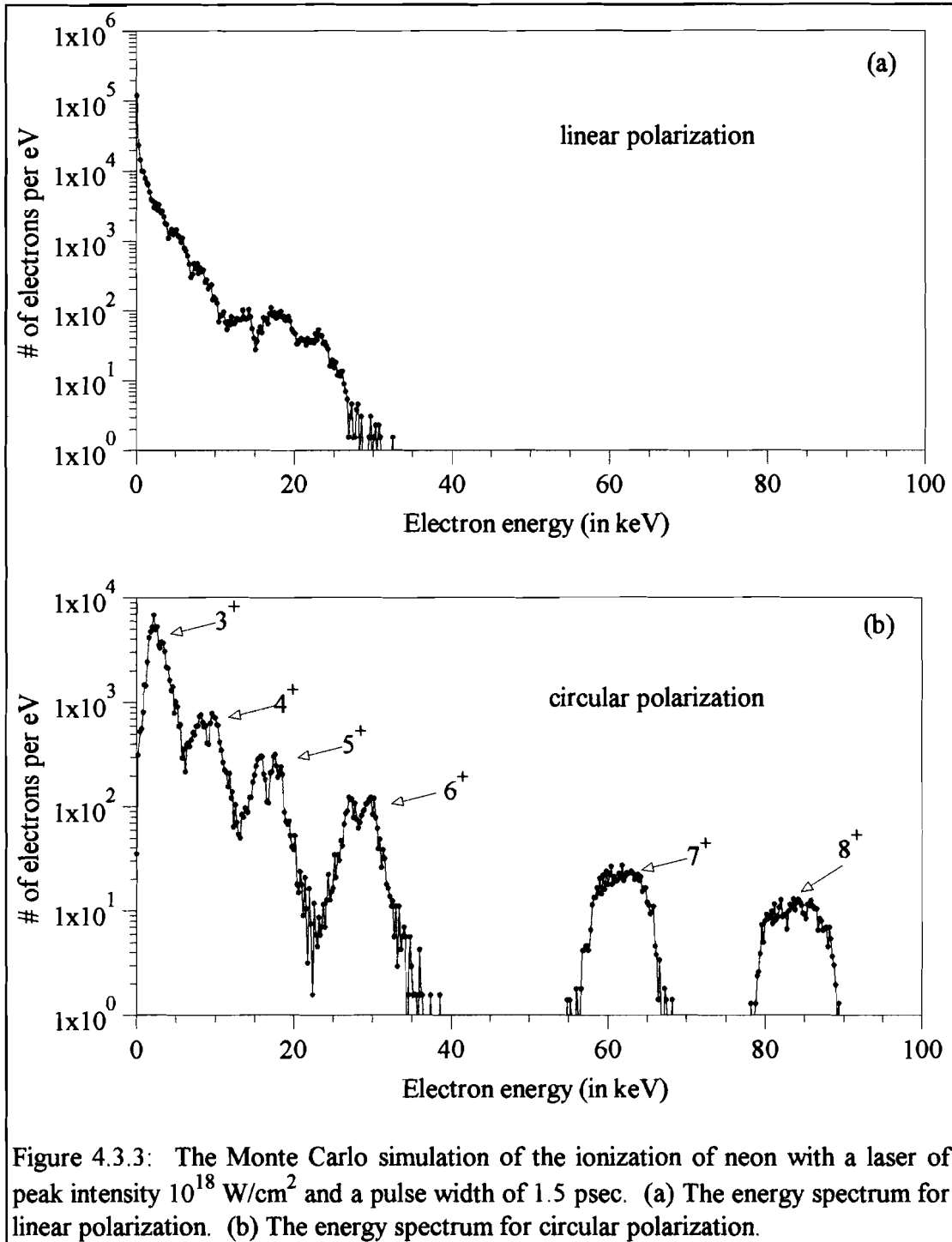
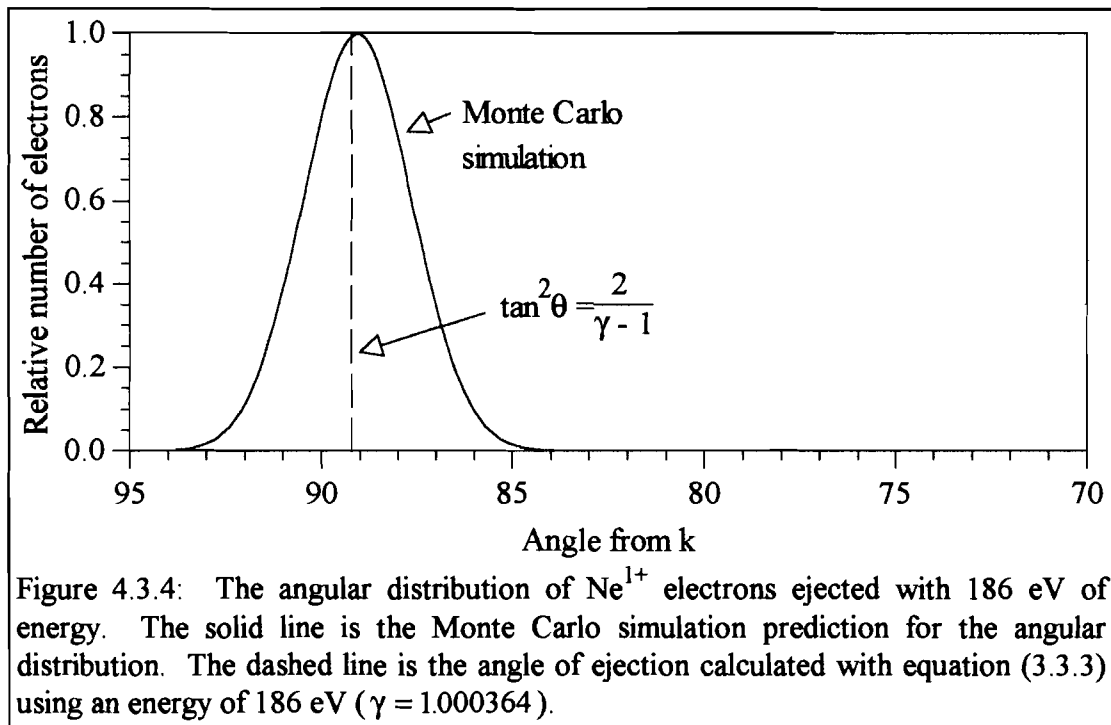
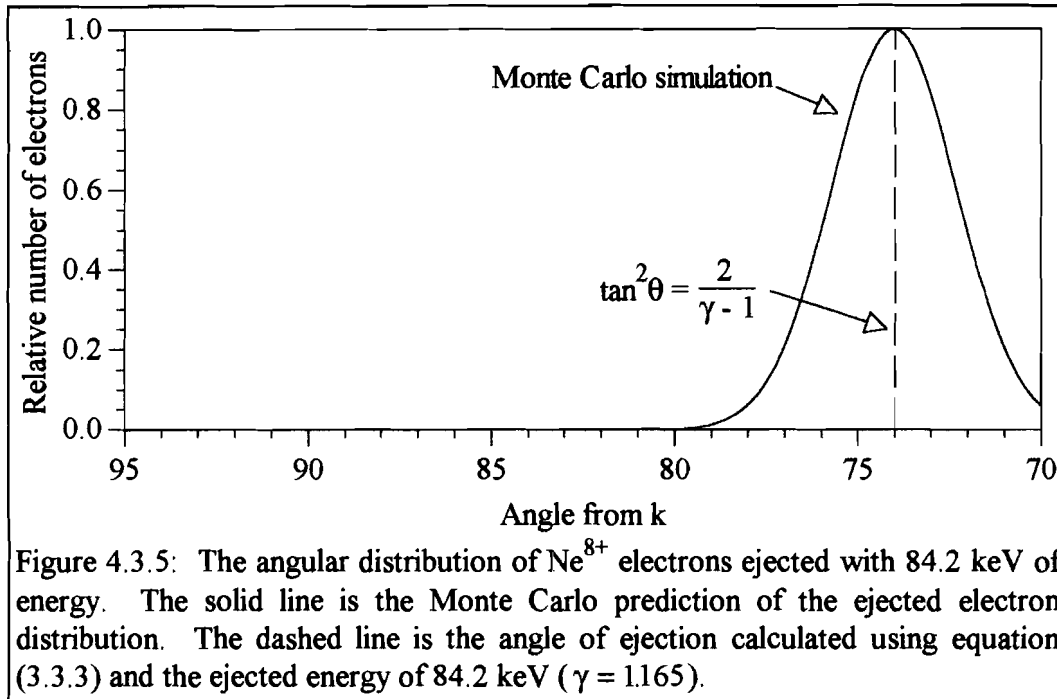


Figure 4.3.3: The Monte Carlo simulation of the ionization of neon with a laser of peak intensity 10^{18} W/cm² and a pulse width of 1.5 psec. (a) The energy spectrum for linear polarization. (b) The energy spectrum for circular polarization.



conservation of energy and momentum between the electron and the field, is 89.2° for 186-eV electrons (position shown by dashed line in Figure 4.3.4). $\gamma \approx 1$ for these electrons, resulting in ejection approximately perpendicular to the laser axis, which is expected at low ionization threshold intensities since $q \ll 1$ and high-intensity Compton effects are minimal.

Figure 4.3.5 shows the Monte Carlo prediction of the angular distribution of Ne^{8+} electrons ionized at $4.0 \times 10^{17} \text{ W/cm}^2$ in a 1.5-ps circularly polarized laser pulse. The angular distribution is peaked at approximately 74.1° . These electrons are ejected with energies of 84.2 keV in the simulation, which corresponds to an angle of 74.0° using equation (3.3.3) (position of dashed line in Figure 4.3.5). The high ionization threshold intensity of these electrons causes interaction with a field strength of $q \sim 1$.



High-intensity Compton scattering causes electron recoil and a \bar{k} component of momentum in agreement with the conservation of energy and momentum argument described by equation (3.3.3).

Many other numerical calculations of the relativistic electron trajectories have been performed. All are in excellent agreement with the predictions of the previous chapters. It is therefore clear that the predictions of the electron trajectories based on the separation of relativistic effects, pulse envelope, and spatial effects are valid when compared to a fully relativistic calculation of the electron trajectories. The next step is to compare these predictions to the actual observations. This will be done following a discussion of the apparatus used in the experiment.

-
- ¹ J.D. Jackson, *Classical Electrodynamics* 2nd ed., (Wiley, New York, 1975).
- ² Peter W. Milonni and Joseph H. Eberly, *Lasers* (Wiley, New York, 1988), p. 484-490.
- ³ M. Lax, W.H. Louisell, and W.B. Knight, "From Maxwell to paraxial wave optics," *Phys. Rev. A* 11, 1365 (1975).
- ⁴ S. Augst, D.D. Meyerhofer, D. Strickland, and S.L. Chin, "Laser ionization of noble gases by Coulomb-barrier suppression," *J. Opt. Soc. Am. B* 8, 858 (1991).
- ⁵ S. Augst, "Tunneling ionization of noble gas atoms using a high intensity laser at 1 μm wavelength," Ph. D. thesis, University of Rochester, 1991.
- ⁶ P.B. Corkum, N.H. Burnett, and F. Brunel, "Above-threshold ionization in the long-wavelength limit," *Phys. Rev. Lett.* 62, 1259 (1989).
- ⁷ William H. Press, Saul A. Teukolsky, William T. Vetterling, and Brian P. Flannery, *Numerical recipes in FORTRAN: the art of scientific computing* 2nd ed. (Cambridge University press, Cambridge, 1992) p.701-716.
- ⁸ P.H. Bucksbaum, M. Bashkansky, and T.J. McIlrath, "Scattering of electrons by intense coherent light," *Phys. Rev. Lett.* 58, 349 (1987).

Chapter 5

Experimental Setup

In the experiments, a circularly-polarized, high-power (~ 1 TW) laser pulse is focused into a vacuum chamber backfilled with neon gas (see Figure 5.0.1). The laser pulse ionizes the gas at the focus, and freed electrons are ponderomotively accelerated from the focus. A magnetic spectrometer placed above the laser focus measures the energy and angular distributions of the electrons. This chapter describes the experimental setup and, in particular, the magnetic spectrometer.

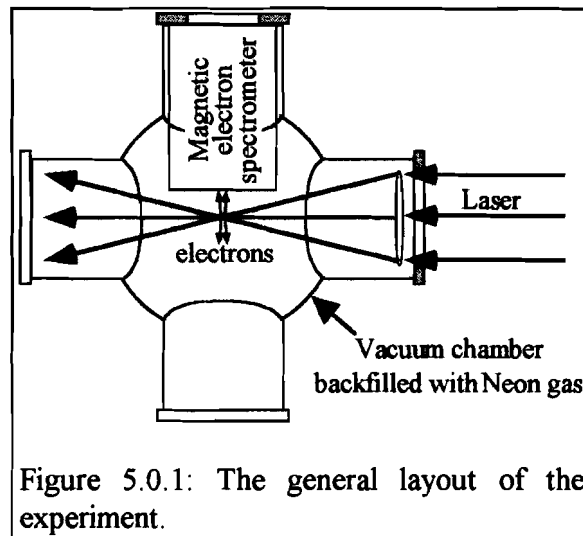


Figure 5.0.1: The general layout of the experiment.

5.1 *Laser system*

The high-power laser pulse used in the experiments is generated with a Nd:YLF/Glass Chirped-Pulse-Amplification (CPA) laser system (see Figure 5.1.1).^{1,2} The pulse begins in a Nd:YLF oscillator where a 100-MHz pulse train with 1 nJ of energy per 50-ps pulse is created. The pulse train undergoes dispersion and self-phase-modulation (SPM) in a 1-km long optical fiber. The dispersion produces a linear dependence of frequency on time (linear temporal chirp) and a pulse width of 100 ps.

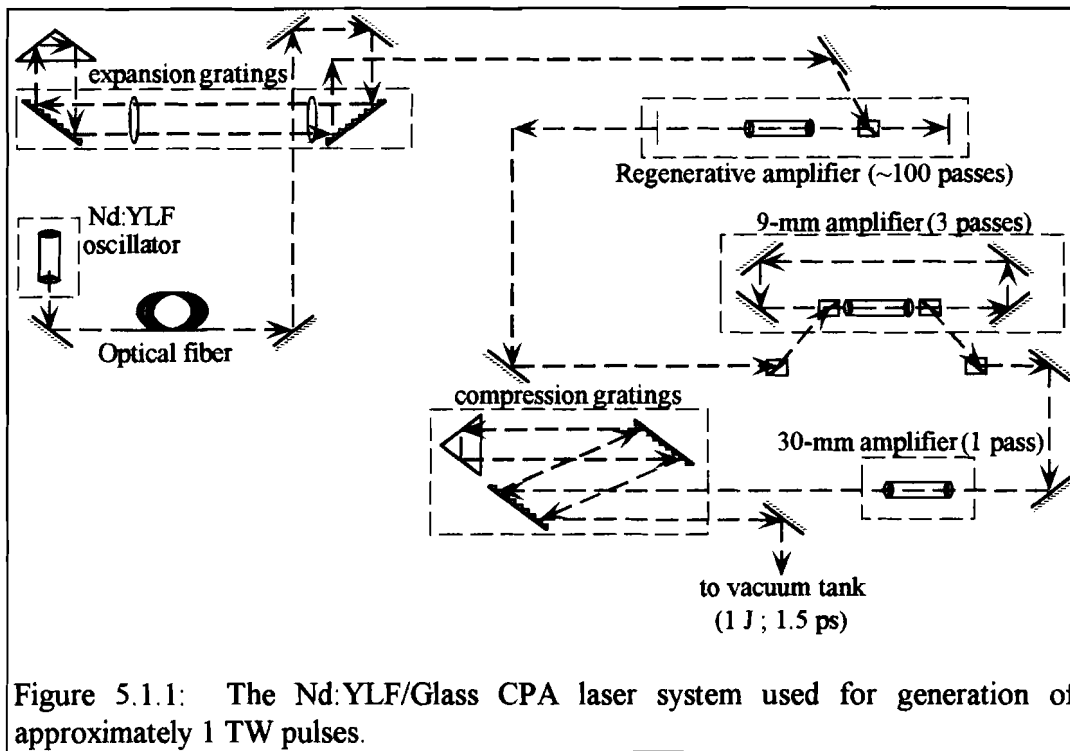


Figure 5.1.1: The Nd:YLF/Glass CPA laser system used for generation of approximately 1 TW pulses.

The SPM increases the bandwidth from 0.3 to 25 Å. Diffraction gratings further expand the pulse width to approximately 500 ps.

A single pulse of this train is switched into a Nd phosphate glass regenerative amplifier, where approximately 100 passes through the amplifier increase the pulse energy to 500 μJ . The many passes also decrease the bandwidth of the pulse to approximately 12 Å due to gain narrowing in the amplifier rod. The pulse is further amplified to 40 mJ by 3 passes through a 9-mm Nd phosphate glass amplifier. The final amplification stage is a 30-mm Nd phosphate glass amplifier that increases the energy to 1 J or higher. The effects of thermal lensing in this amplifier limit the repetition rate of the laser to one pulse every 3 minutes. A pair of gold coated, holographic diffraction

gratings compress this high-energy pulse to approximately the Fourier transform limited pulse width ($\Delta t \Delta \nu = 0.44$), or approximately 1.5 ps.

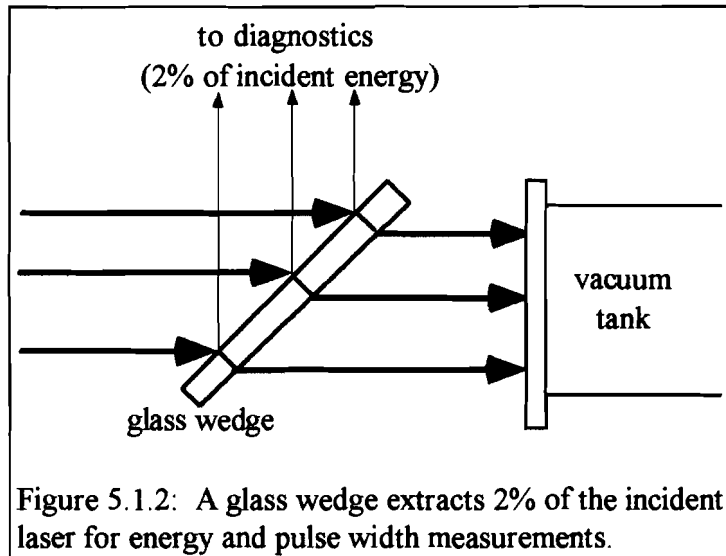


Figure 5.1.2: A glass wedge extracts 2% of the incident laser for energy and pulse width measurements.

The pulse width and energy are measured for each laser shot during the experiment by deflecting 2% of the laser pulse to a pair of diagnostics

(see Figure 5.1.2). The pulse width is measured using 2nd-order auto-correlation which has a relative uncertainty of $\pm 15\%$ and an absolute uncertainty of $\pm 30\%$. An example of an auto-correlation trace of the pulse is shown in Figure 5.1.3. The solid

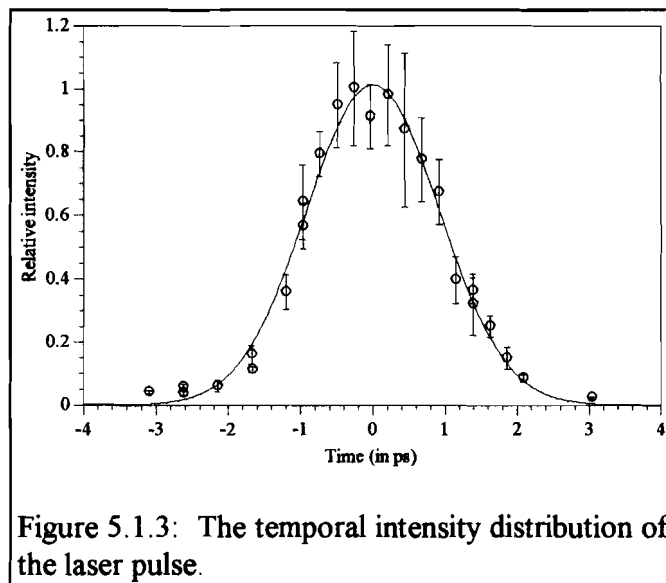


Figure 5.1.3: The temporal intensity distribution of the laser pulse.

curve is a Gaussian curve fit to the data. In this case, the measured pulse was approximately 2 ps long, which is longer than the typical pulse width of 1.5 ps.

The energy is measured with a photo-diode and a 2249w analog-to-digital converter (ADC). The photo-diode produces a pulse of current that is integrated by the

ADC. The total charge integrated by the ADC is linearly related to the incident laser energy. By calibrating this signal using an energy monitor placed directly before the vacuum tank, the energy is determined to an absolute uncertainty of $\pm 10\%$ and a relative uncertainty of $\pm 5\%$.

Figure 5.1.4 shows the near-field intensity distribution of the laser at the lens. This intensity distribution is without the 30-mm amplifier firing. Previous measurements have shown that the 9-mm amplifier governs the intensity distribution, and the 30-mm amplifier is unnecessary for these measurements. The flat-top nature of the distribution shown is due to higher gain in the outer edges of the 9-mm amplifier rod. This is caused by higher absorption of the pump radiation in the edges of the rod. The higher gain in the edges of the rod amplifies the wings more than the center of the spatially Gaussian input pulse and results in a flat-top beam profile.

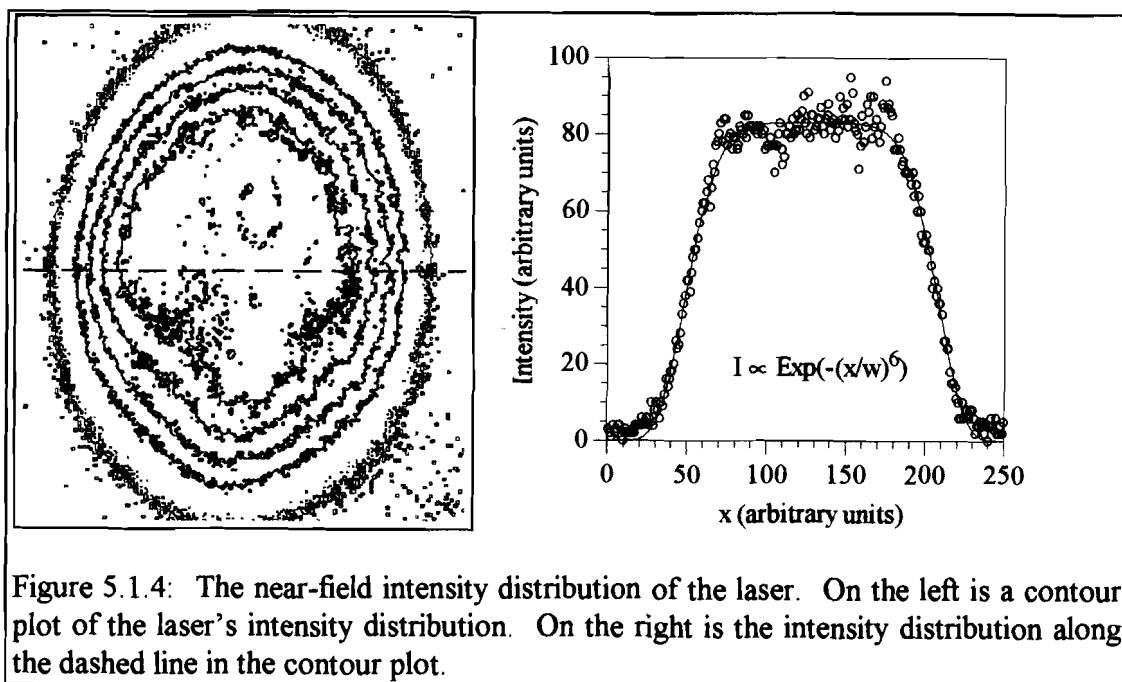


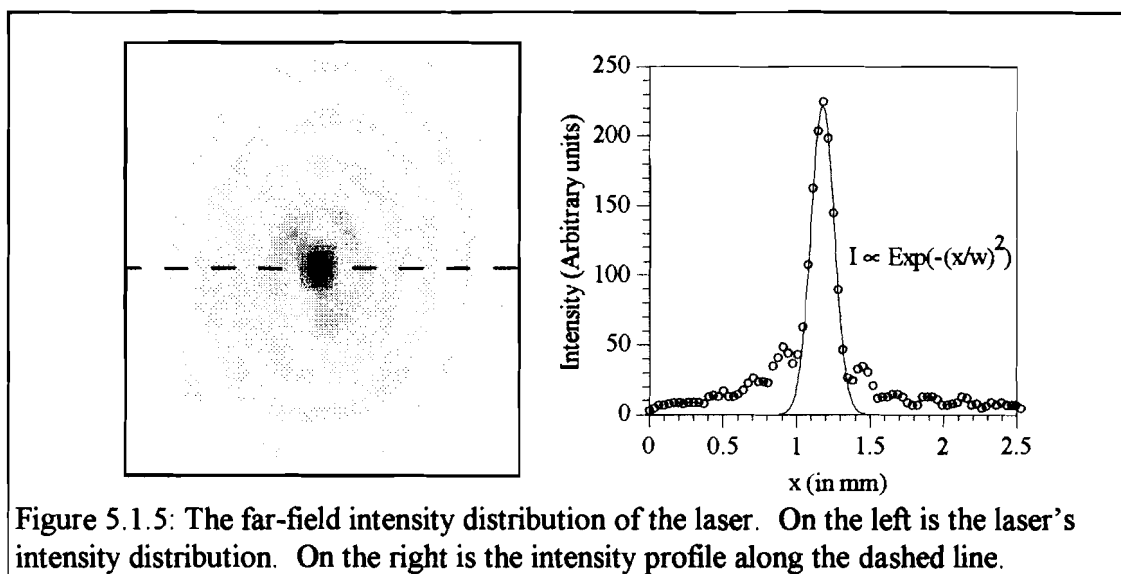
Figure 5.1.4: The near-field intensity distribution of the laser. On the left is a contour plot of the laser's intensity distribution. On the right is the intensity distribution along the dashed line in the contour plot.

A 20-cm focal length lens focuses the pulse to a spot size of $37 \pm 3 \mu\text{m}^2$ in the vacuum chamber. The area of the spot size is defined as,

$$\text{Area} \equiv \frac{1}{I_{\text{peak}}} \int I(x, y) dA, \quad (5.1.1)$$

where I_{peak} is the peak intensity and the integral is over the plane perpendicular to the laser propagation direction at the beam waist (position where spot size is minimum).

The spot size was determined by placing a short focal length imaging lens after the focus of the 20-cm lens used for the experiments. The 30-mm amplifier was not used in these measurements. The imaging lens magnified the focal spot, allowing a picture of the focus to be taken with a charge-coupled-device (CCD) (see Figure 5.1.5). The magnification was found to be 34 ± 1 by measuring the image distance (distance from the imaging lens to the imaged focus) and the object distance (distance from the 20-cm lens focus to the imaging lens) and taking their ratio. The area of the central



peak of the imaged focal spot shown in Figure 5.1.5 was $85,400 \mu\text{m}^2$. The true focal spot size of the 20-cm focal length lens was determined to be approximately $37 \mu\text{m}^2$ by dividing the magnified focal spot area by the square of the magnification. The focal spot size was found not to fluctuate on a shot-to-shot basis. The spot size was therefore not measured for each laser shot during the experiments since a one-time measurement was sufficient.

The combined uncertainties of the energy, pulse width, and spot size result in a relative uncertainty in the intensity of $\pm 20\%$ and an absolute uncertainty of approximately $\pm 35\%$.

The calculations in the previous chapters assumed a Gaussian TEM_{00} mode laser profile. The actual distributions are a super-Gaussian at the lens (see Figure 5.1.4) and a Gaussian central peak with rings at the focus (see Figure 5.1.5). The rings at the focus occur due to a combination of two diffraction effects. The approximately flat-top incident beam produces an Airy disc pattern,³ and a 5-mm hole in the center of the focusing lens results in diffraction rings. The effects of the experimental focal distribution are minimal in connection with high-intensity Compton scattering. This is because the focus is still axially symmetric, resulting in a symmetric ponderomotive force (see section 3.2),

$$F_z(z) = -F_z(-z).$$

An increase in the angular spread of the electron distribution is possible due to larger variations in the radial vs. axial components of momentum, but the peak of the angular distribution will be unaffected.

5.2 *Magnetic electron spectrometer*

A magnetic spectrometer was constructed to measure the energy and angular distributions of the electrons ejected from the laser focus. Figure 5.2.1 shows the layout of the spectrometer. Detailed schematics of the spectrometer are presented in Appendix B. Ejected electron trajectories are curved in a magnetic field in the gap of a “c-shaped” electromagnet and travel toward an organic plastic scintillator.⁴ Electrons striking the scintillator release photons that are detected by a photomultiplier tube (PMT).

The electrons are detected if they are curved the proper amount in the magnetic field to allow propagation to the scintillator. Electrons traveling perpendicular to a constant magnetic field travel in a circle with a radius known as the gyration radius. This radius is found from the electron’s equations of motion in a constant magnetic field,

$$\frac{d\vec{p}}{dt} = -\frac{e}{c} \vec{v} \times \vec{B} \quad \text{and} \quad (5.2.1)$$

$$\frac{dE}{dt} = mc^2 \frac{d\gamma}{dt} = 0. \quad (5.2.2)$$

Since γ is constant in time, equation (5.2.1) reduces to

$$\frac{d\vec{v}}{dt} = -\frac{e}{\gamma mc} \vec{v} \times \vec{B}. \quad (5.2.3)$$

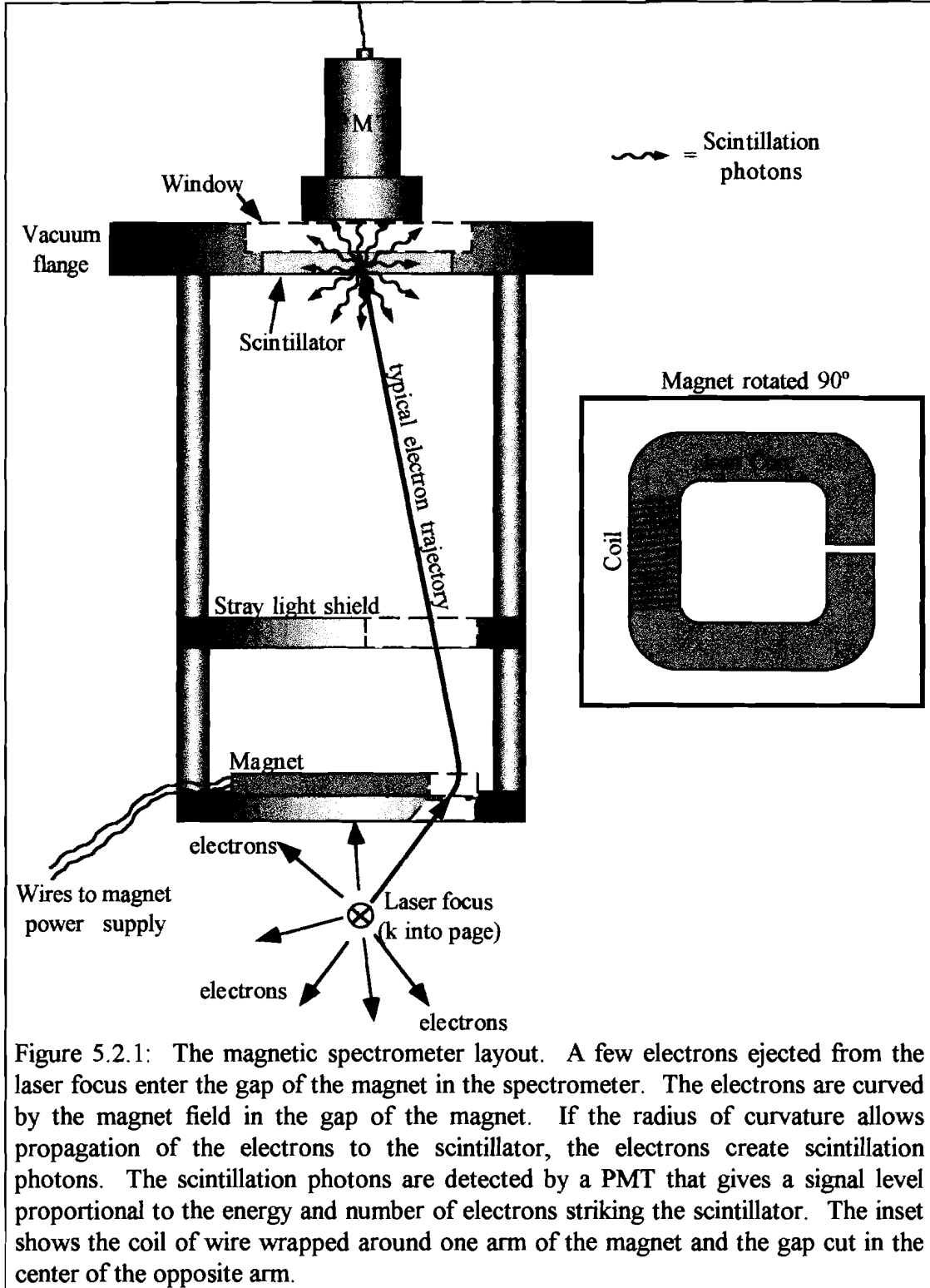


Figure 5.2.1: The magnetic spectrometer layout. A few electrons ejected from the laser focus enter the gap of the magnet in the spectrometer. The electrons are curved by the magnet field in the gap of the magnet. If the radius of curvature allows propagation of the electrons to the scintillator, the electrons create scintillation photons. The scintillation photons are detected by a PMT that gives a signal level proportional to the energy and number of electrons striking the scintillator. The inset shows the coil of wire wrapped around one arm of the magnet and the gap cut in the center of the opposite arm.

This equation describes circular motion with a frequency of

$$\omega_B = \frac{e|\vec{B}|}{\gamma mc} = \frac{ec|\vec{B}|}{E} \quad (\text{the gyration frequency}), \quad (5.2.4)$$

and a radius of

$$\rho = \frac{|\vec{v}_0|}{\omega_B} = \frac{\sqrt{E^2 - m^2 c^4}}{e|\vec{B}|} \quad (\text{the gyration radius}). \quad (5.2.5)$$

where \vec{v}_0 is the initial velocity of the electron. The geometry of the spectrometer determines the gyration radius necessary for detection (see Figure 5.2.2). This causes ρ to be fixed and the relation between the electron energy and magnetic field is,

$$E^2 = (e\rho B)^2 + m^2 c^4 \quad (5.2.6)$$

By varying the strength of the magnetic field, the energy window of the spectrometer is changed according to equation (5.2.6).

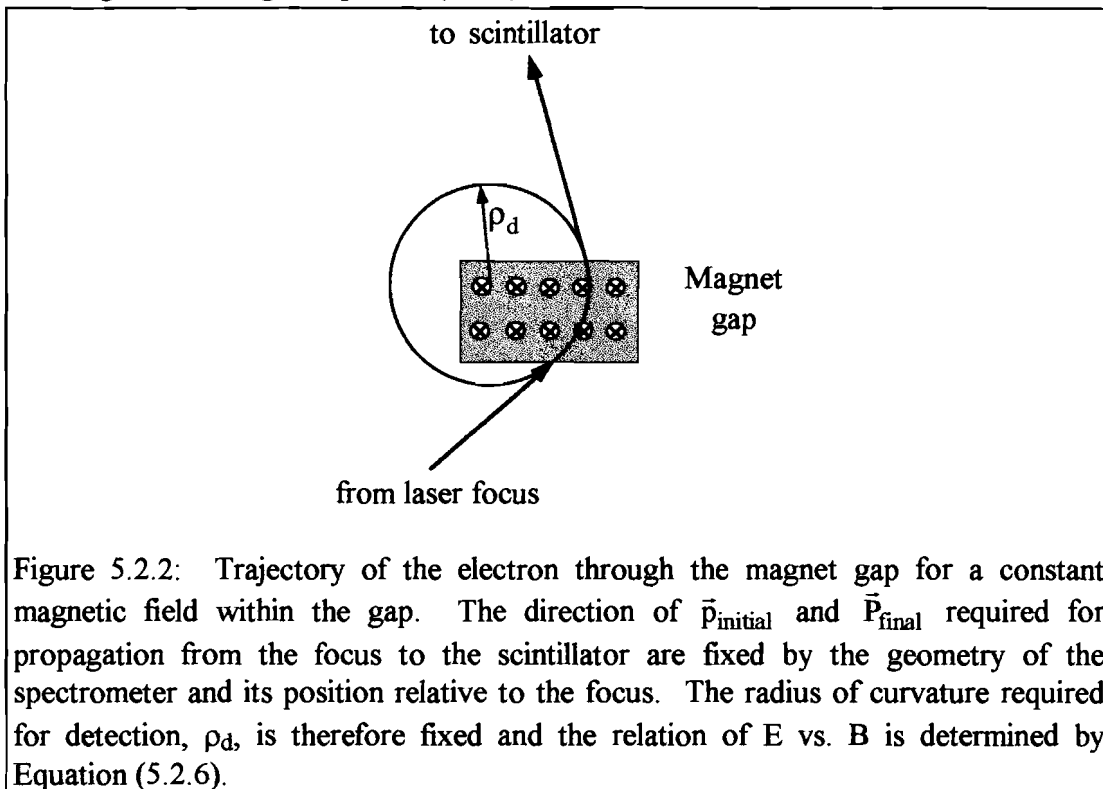


Figure 5.2.2: Trajectory of the electron through the magnet gap for a constant magnetic field within the gap. The direction of \vec{p}_{initial} and \vec{P}_{final} required for propagation from the focus to the scintillator are fixed by the geometry of the spectrometer and its position relative to the focus. The radius of curvature required for detection, ρ_d , is therefore fixed and the relation of E vs. B is determined by Equation (5.2.6).

The magnetic field in the gap of the magnet is generated by sending current through the coil wrapped around one arm of the c-shaped iron core. The coil is a solenoid that generates a magnetic field within the iron core. The high permeability of the iron core ($\mu \sim 1000\mu_0$) confines the magnetic field lines in the iron and the magnetic field travels around the core and through the gap creating a closed magnetic circuit (see Figure 5.2.3). The small width of the gap (2 mm) allows approximately 97% of the magnetic field generated by the coil to travel around the core and through the gap. Approximately 3% of the magnetic field from the coil “leaks” from the iron core.

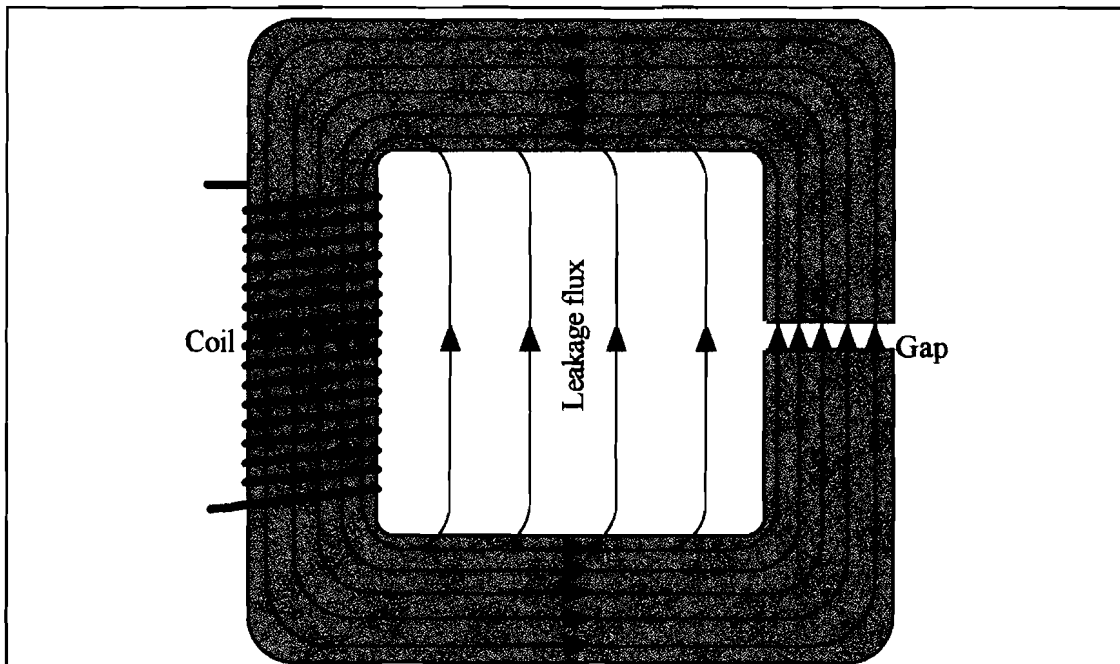


Figure 5.2.3: The magnetic flux lines of the c-shaped magnet in the spectrometer. The dark region is the iron core of the magnet. The high permeability ($\mu \sim 1000\mu_0$) of the iron confines 97% of the magnetic field to the magnetic circuit created by the iron and the gap. 3% of the magnetic flux leaks from the iron through the hollow center of the magnet.

The current through the coil is a 100-ms square-topped pulse. The coil can be viewed as an inductor and resistor in series, where the resistance is the resistance of the wire in the coil. A circuit of this type arrives in a steady state in a time given approximately by L/R where L is the inductance and R is the resistance.⁵ The coil has an inductance of approximately 1 millihenry and a resistance of 0.3Ω . This circuit therefore arrives in a steady state in approximately 3 ms. The electrons enter the gap of the magnet 80 ms after the beginning of the current pulse and therefore experience a constant magnetic field.

The strength of the magnetic field in the gap of the magnet was measured using a Hall probe⁶ to an accuracy better than $\pm 5\%$. Initial measurements of the field measured the “hysteresis” loop of the magnet (see Figure 5.2.4). A 100-ms flat-top pulse of current was fired through the coil and the steady state field in the gap was measured. The magnitude of the current pulse was then decreased in constant increments until the negative of the initial current pulse was reached. The opposite arm of the hysteresis loop was generated by reversing the above process until the initial current pulse was reached.

Accurate determination of the magnetic field is required for measurement of the electron energy through equation (5.2.6). The significant hysteresis effects evident in Figure 5.2.4 make a determination from the current alone insufficient since the history of the iron core plays a crucial role in the amplitude of the magnetic field. Only

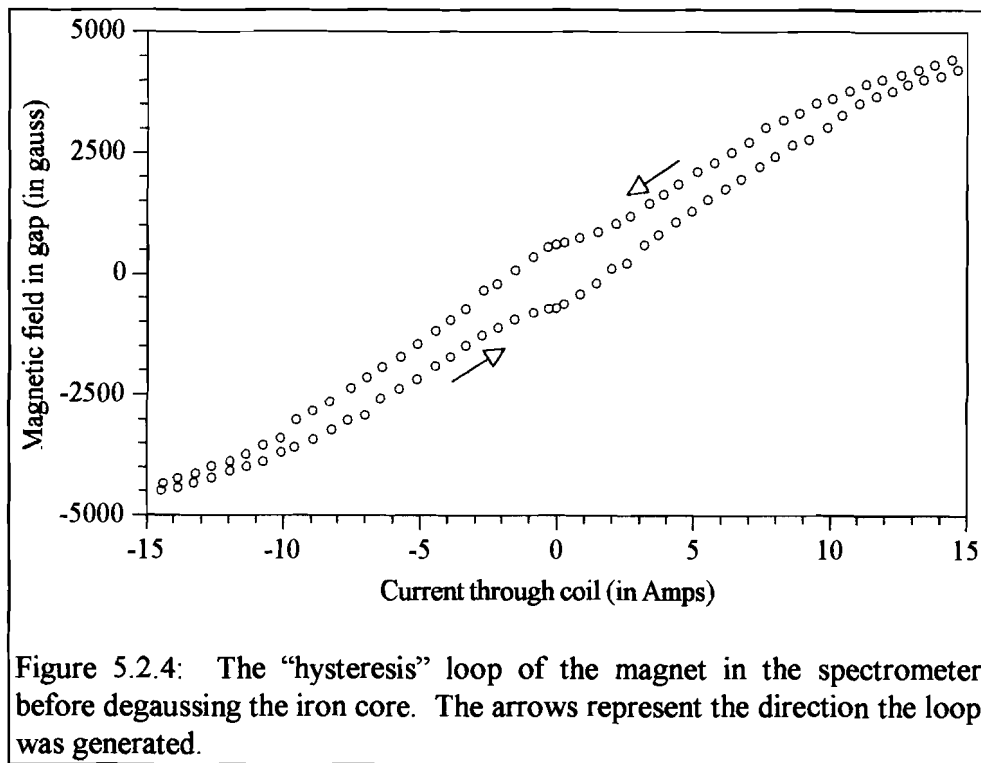


Figure 5.2.4: The “hysteresis” loop of the magnet in the spectrometer before degaussing the iron core. The arrows represent the direction the loop was generated.

a direct measurement of the field would be sufficient and this was impractical during normal operation of the spectrometer.

The problem was solved by degaussing the iron core after each flat-top pulse of current through the coil. The hysteresis effects were related to residual fields left in the iron core after the magnet was “fired.” For example, a pulse of 15 Amps left a strong residual field of approximately 600 Gauss in the gap, which affected subsequent firing of the magnet.

The degaussing of the core significantly reduces the magnet’s residual field. One second after the end of the 100 ms DC pulse, a slowly diminishing sinusoidal current is applied to the magnet. This has the effect of sending the magnet through a hysteresis loop for each cycle of the current. The slowly decreasing amplitude of the

AC current causes each subsequent hysteresis loop to become smaller and smaller. After many cycles the current approaches zero and the hysteresis loop collapses about the origin, i.e., zero current and field. This degaussing concept is shown pictorially in Figure 5.2.5. This figure is only a demonstration of principle and is not an actual measurement.

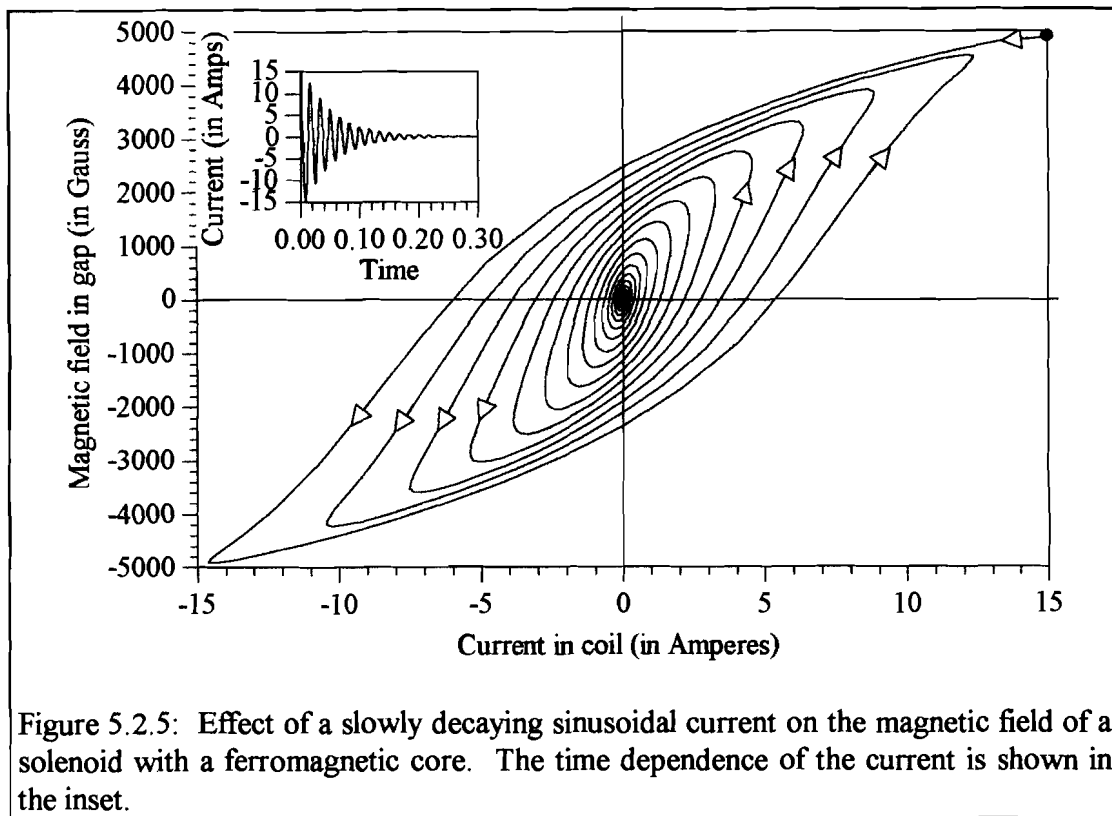


Figure 5.2.5: Effect of a slowly decaying sinusoidal current on the magnetic field of a solenoid with a ferromagnetic core. The time dependence of the current is shown in the inset.

The schematic of a circuit to degauss a magnetic material is shown in Figure 5.2.6. When the switch is closed, 10 VAC is applied across a pair of positive-temperature-coefficient (PTC) thermistors and the magnet coil. A PTC thermistor is a device whose resistance increases as its temperature increases (see Figure 5.2.7). Thermistors with 1Ω resistance at room temperature are used in the degaussing

circuit for the electromagnet in the spectrometer. The coil has a resistance of 0.3Ω giving a total resistance for the circuit of 0.8Ω . This results in an initial current of

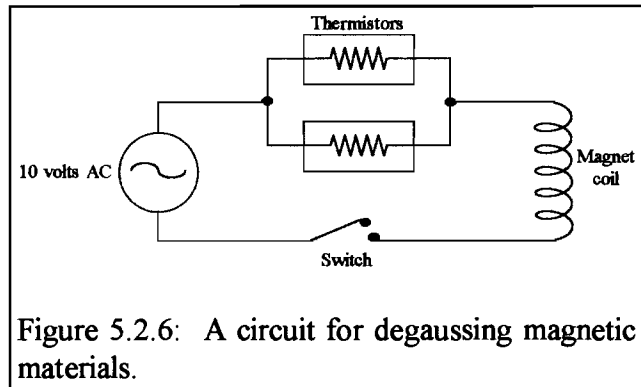


Figure 5.2.6: A circuit for degaussing magnetic materials.

12.5 A through the circuit. Each thermistor initially conducts 6.25 A and therefore absorbs 78 W of power. The thermistors are only able to dissipate approximately 14 mW of power per $^{\circ}\text{C}$ above the ambient temperature and are therefore resistively heated. As the thermistors heat up, their resistance increases and this decreases the current flowing through the coil. As the current decreases, the power absorbed by the thermistors also decreases. When each thermistor's resistance reaches approximately 90Ω , the power absorbed is equal to the power dissipated by the thermistor and the circuit arrives in a steady state. The residual current is approximately 280 mA and the corresponding magnetic field of approximately 20 Gauss represents the limit of the degaussing of the magnet with this setup.

The residual current can be made smaller by increasing the voltage across the

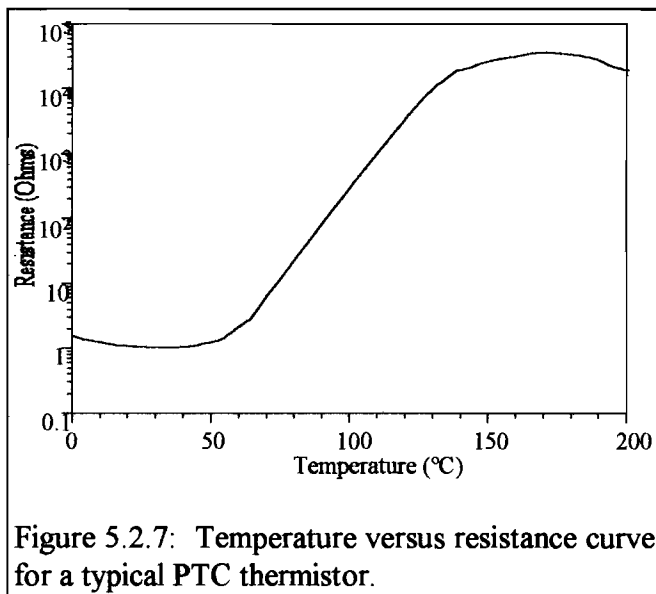


Figure 5.2.7: Temperature versus resistance curve for a typical PTC thermistor.

thermistors and coil. However, an increase in voltage causes the thermistor to heat up faster and therefore “turn off” faster. The current must diminish slowly to allow the hysteresis cycles to spiral inward to zero field. The above combination of 1Ω thermistors and 10 V of applied voltage represents the optimal arrangement (found empirically) for minimum residual field.

The circuit for firing and degaussing the magnet is shown in Figure 5.2.8. A variac adjusts the voltage from a DC power supply between 0 and 24 V. A trigger from the laser system closes the “DC Relay” in the figure 80 ms before the laser pulse arrives in the vacuum tank. This relay remains closed for 100 ms and allows the 0 to 24 V from the DC power supply through the magnet coil. A “reverse field switch” selects the polarity of the voltage and therefore, the direction of the magnetic field in the magnet. One second after the DC relay opens, another relay (AC relay) closes

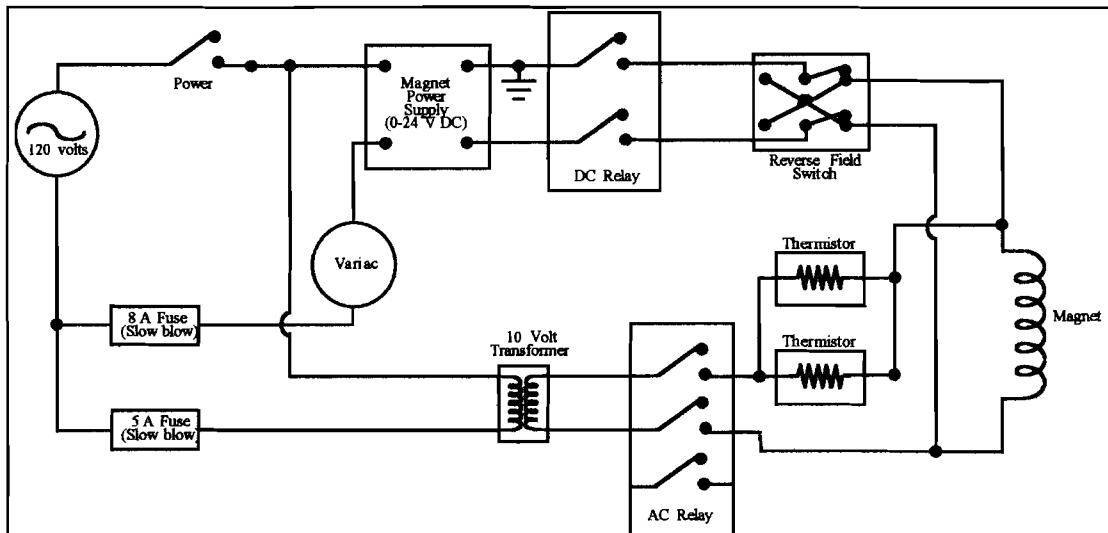


Figure 5.2.8: Circuit diagram of the power supply to fire and degauss the magnet in the electron spectrometer.

allowing 10 VAC through the coil of the magnet. This current flows through two thermistors that begin to heat and suppress the current flowing through the coil. The AC relay closes for approximately 10 seconds to allow the current to arrive in a steady state. After the AC relay opens, the thermistors require approximately 20 seconds to cool before the magnet can be fired again. This technique assures that the magnet is degaussed every time the DC voltage is fired.

The magnetic field as a function of current after degaussing is shown in Figure 5.2.9. The magnetic field generated in the gap was measured for a series of current

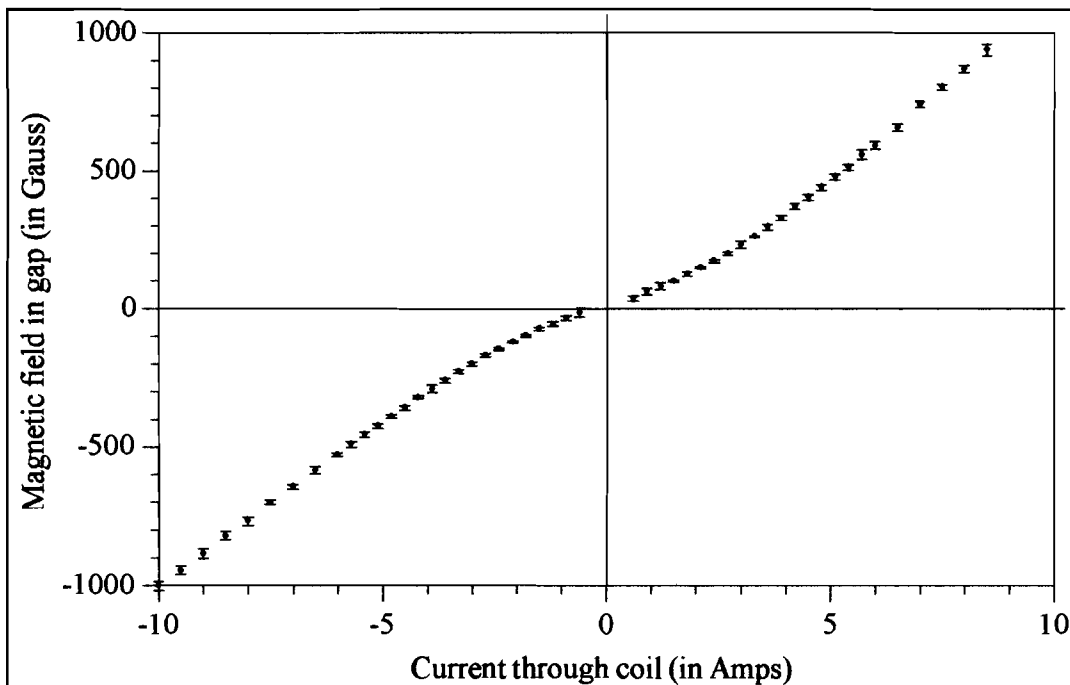


Figure 5.2.9: The magnetic field generated in the gap of the magnet as a function of current through the coil after degaussing. Six measurements were taken at a series of current settings. The measurements were taken in random order so that any significant hysteresis effects should cause large fluctuations in the field. The average standard deviation of the magnetic field was <3% for fields above 80 gauss.

settings. The current was randomly changed between current settings until 6 points at each current were measured. The average values and the standard deviation (error bars) of these 6 points at each current are shown in the figure. The error bars show only small fluctuations in the magnetic field above 80 Gauss. The dependence of the field on the history of the magnet has therefore been eliminated and the field strength can now be accurately determined from the current alone. Below 80 Gauss, the residual field still significantly affects the field produced, resulting in large relative fluctuations. The spectrometer is therefore only accurate at magnetic field strengths above 80 gauss or a corresponding electron energy of 2 keV.

The path of the electrons through the spectrometer is approximately 30 cm. The operation of the spectrometer requires the propagation of electrons without interaction with other particles at the pressure of neon gas used in the experiment, 10^{-3} Torr. Two interactions are possible; the electrons can interact with the background atoms in the vacuum tank or the electrons can interact with other charged particles.

The electron range of 0.3 keV to 20 MeV electrons in a neutral material is to a good approximation,⁷

$$R(\text{cm}) = 537 \times 10^{-4} \frac{E(\text{keV})}{\rho(\text{g/cm}^3)} \left(1 - \frac{0.9815}{1 + 0.003123E(\text{keV})} \right) \quad (5.2.7)$$

where E is the electron energy and ρ is the material's density. The experiments performed measured electron energies greater than 1 keV in neon. The range of 1 keV electrons in 10^{-3} Torr of neon gas ($12 \times 10^{-9} \text{ g/cm}^3$) is 10 meters. Higher energy electrons will propagate further and interactions with neutral atoms are therefore insignificant in the experiment.

The effects of interactions with other charged particles were determined experimentally. The signal level from the detection of low-energy (3 keV) electrons at 10^{-3} Torr was compared to signal levels at 5×10^{-4} Torr. The signal level at 10^{-3} Torr was twice the signal level at 5×10^{-4} . Collective plasma interactions would result in a nonlinear dependence of the signal level on the pressure that was not observed. These effects are therefore unimportant at 10^{-3} Torr and can be ignored.

The range of electrons is also important in determining the minimum thickness of the scintillator and shielding needed for complete absorption of electrons. The highest energy or deepest penetrating electrons in the experiments had an energy of 80 keV. These electrons have a range of 90 μm in the plastic scintillator and 30 μm in the aluminum shielding. The electrons are therefore completely absorbed in a very thin layer on the inside surface of the scintillator and minimal thickness shielding is required to block the electrons completely.

The shielding is necessary in two places within the spectrometer. One is the bottom disk of the spectrometer which holds the magnet. This must stop electrons

from traveling to the scintillator without going through the magnet gap. The disk is 1.27 cm thick which easily stops all electrons of interest. The second is a 3 mm thick aluminum mask placed over the scintillator which is discussed below. This mask completely blocks electrons from striking the outer portions of the scintillator.

The radius of curvature necessary for detection can be estimated analytically using a square topped magnetic field within the gap of the magnet and zero magnetic field elsewhere, i.e., by assuming that fringe fields and leakage from the magnet core can be ignored. These estimates give the required gyration radius as 1.1 cm and do not agree well with the radius found in the experimental calibration, 1.54 cm (see section 5.3). This discrepancy occurs because the contribution of fringe and leakage fields can be substantial.

The electron's equation of motion in a constant magnetic field is given by equation (5.2.3),

$$\frac{d\vec{v}}{dt} = -\frac{e}{\gamma mc} \vec{v} \times \vec{B}$$

or

$$d\vec{v} = -\frac{e}{\gamma mc} d\vec{l} \times \vec{B} \quad (5.2.8)$$

where $d\vec{l}$ is the differential path length of the electron's trajectory. Therefore, $B d\vec{l}$ gives the magnitude of the curvature. Since the fringe and leakage fields act over larger distances than the field within the gap, small values of the magnetic field outside

the gap can be offset by large propagation distances and play a substantial role in the electron trajectories.

The magnetic field profiles in and around the gap in the magnet were measured using a Hall probe. The measured profiles (see Figure 5.2.10) showed large fringe fields from the gap and a background leakage field of approximately 3% the peak magnetic field in the gap.

The fringe fields are due to the finite dimensions of the faces of the gap. The background field is due to the leakage of magnetic flux between the arms of the magnet caused by the finite magnetic permeability of the iron core. To model the magnet's field profile analytically, the measured values are curve-fit to a field of the form,

$$\frac{B_{\text{peak}}}{\left(1 + (\xi/w)^a\right)^b} \quad (5.2.9)$$

where B_{peak} is the peak magnetic field in the gap, ξ is the x or z coordinate as shown in the inset of Figure 5.2.10, and w is the width of the distribution. This function fits the curves well except for a slight deviation near the center of the magnet (at $x=4$ cm in the profile in the x direction). The slight deviation is due to the leakage flux from the iron and is accounted for by a separable field which drops off as $1/r^2$ for large

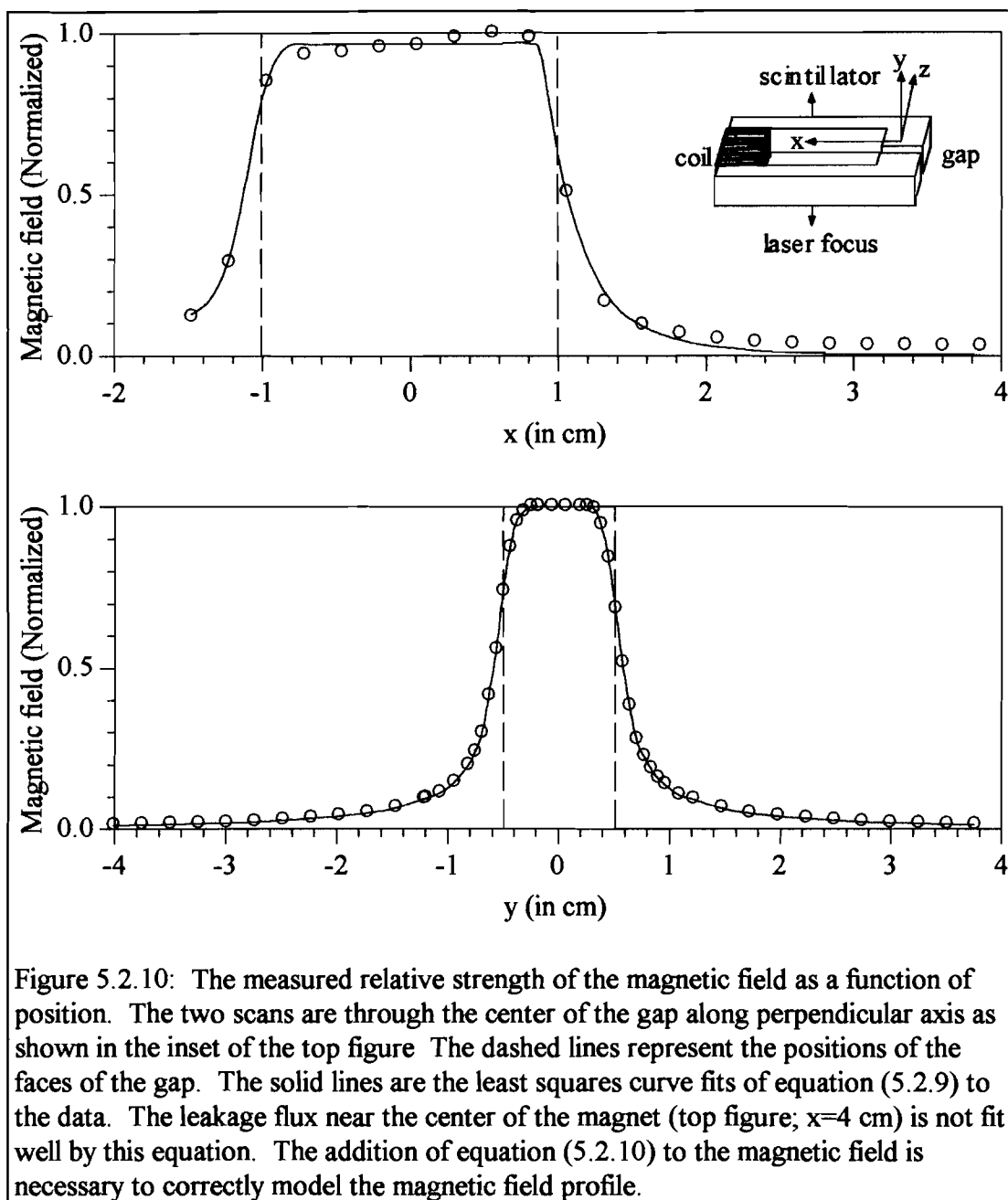


Figure 5.2.10: The measured relative strength of the magnetic field as a function of position. The two scans are through the center of the gap along perpendicular axis as shown in the inset of the top figure. The dashed lines represent the positions of the faces of the gap. The solid lines are the least squares curve fits of equation (5.2.9) to the data. The leakage flux near the center of the magnet (top figure; $x=4$ cm) is not fit well by this equation. The addition of equation (5.2.10) to the magnetic field is necessary to correctly model the magnetic field profile.

distances from the magnet, in analogy to the expected fall off of a field from a “hole” in a conductor.⁸ This field is assumed to be of the form,

$$B(y) = \frac{B_{\text{leak}}}{1 + (y/r_m)^2} \quad (5.2.10)$$

where B_{leak} is the field at the center of the magnet, y is along the central axis of the spectrometer (see Figure 5.2.10 inset), and r_m is the effective radius of the hole in the magnet (the radius of a circle with the same area as the opening in the center of the magnet, 3.4 cm). The contributions from the fringe fields and the leakage flux are added to give the total distribution of the magnetic field.

A Monte Carlo simulation of the electron’s propagation through the spectrometer has been performed. The computer code is presented in appendix C. The simulation modeled the magnetic field in the gap based on the measurements of the fields described above. The gyration radius found in the simulation, 1.52 cm, was in excellent agreement with the gyration radius found from the experimental calibration, 1.54 cm (see section 5.3).

The number of electrons striking the scintillator can be approximated from the measured signal levels. The light output of the scintillator is linear with electron energy for electron energies greater than 125 keV,⁴

$$N_p \propto E \cdot N_e \quad (5.2.11)$$

where N_e is the electron number, N_p is the number of photons created, and E is the electron energy. For energies below 125 keV, surface quenching effects⁴ cause the light output to drop below the linear approximation of equation (5.2.11). The exact energy dependence of surface quenching effects requires an experimental calibration of the light output versus electron energy. This calibration has not been performed. However, the maximum effect of surface quenching for the electron energies observed in the experiments is a 10% deviation from the linear approximation of equation (5.2.11).⁴ The use of a linear approximation for the scintillator's energy response therefore introduces little error.

The light output of the scintillator in the linear regime is approximately 10 photons per keV of incident electron energy or,⁷

$$N_p \approx 10 \cdot E(\text{keV}) \cdot N_e \quad (5.2.12)$$

The 2.5-cm diameter photo-cathode of the PMT is 2.5 cm from the inside surface of the scintillator. If we assume photons are generated directly below the PMT on the inside surface of the scintillator, the photo-cathode subtends a solid angle of 1.26 sr or collects 10% of the photons produced in the scintillator. The quantum efficiency of the photo-cathode is 25% for the 420-nm scintillation photons. The gain of the PMT at the voltage used in the experiments, 1500 V, is $5 \times 10^5 \pm 50\%$. The total charge produced by the PMT for N_e electrons of energy E striking the scintillator is therefore,

$$\begin{aligned}
 q &\approx e E(\text{keV}) N_e (10)(0.10)(0.25) (5 \times 10^5) \\
 &\approx 0.02 E(\text{keV}) N_e \text{ picocoulombs}
 \end{aligned}
 \tag{5.2.13}$$

A 2249w Analog-to-Digital Converter (ADC) is used to integrate the total charge produced. The ADC produces 1 count of signal for each 0.25 pC of input charge. The number of counts from the 2249w is therefore given by,

$$N_c \approx (0.08) E(\text{keV}) N_e. \tag{5.2.14}$$

This allows determination of the number of electrons striking the scintillator from the measured signal of the ADC,

$$N_e \approx 125 \frac{N_c}{E(\text{keV})}. \tag{5.2.15}$$

This derivation is intended as an order of magnitude calculation of the number of electrons only. The uncertainty in the gain of the PMT and variations in the solid angle subtended by the PMT (due to electrons not striking directly below the PMT) may cause significant differences between the number calculated in equation (5.2.15) and the actual number of electrons.

An error in the absolute number of electrons is unimportant to the experiments described in this thesis. Only the relative number of electrons is required for an accurate determination of the energy and angular distributions. The relative error is known to within $\pm 10\%$ since this only depends on the linearity of the scintillator and PMT. The response of the PMT is highly linear in the absence of saturation, which was avoided during these experiments.

5.3 The energy calibration of the spectrometer

An electron gun was constructed to calibrate the energy versus magnetic field response of the spectrometer. Two parallel copper plates were placed on either side of the laser focus (see Figure 5.3.1). The plates were aligned so that the perpendicular to the surface of the plates passed through the gap in the magnet. A hole was cut in the plate between the laser focus and the gap in the magnet, and copper screening was placed over the hole.

An electrostatic field was applied across the plates and the vacuum chamber was backfilled with helium. A low-energy laser pulse (approximately 15 mJ) focused between the plates ionized the helium resulting in a low-density plasma. The ions were accelerated by the electrostatic field away from the gap in the magnet toward the cathode. The ions struck the cathode and released many low-energy ($E_{\text{initial}} < 50$ eV) secondary electrons.⁹ These electrons were accelerated by the electrostatic field toward the anode and the gap in the magnet. As the electrons reached the anode and passed through the copper grid, acceleration ceased and the electrons traveled at a constant energy corresponding to the full potential of the applied electrostatic field (2.5 to 20 kV). The small initial energies ($E_{\text{initial}} < 50$ eV) compared to the final energies ($E_{\text{final}}=2.5$ to 20 keV) of the electrons resulted in a nearly monoenergetic distribution. The electrons then traveled to the gap and entered the spectrometer.

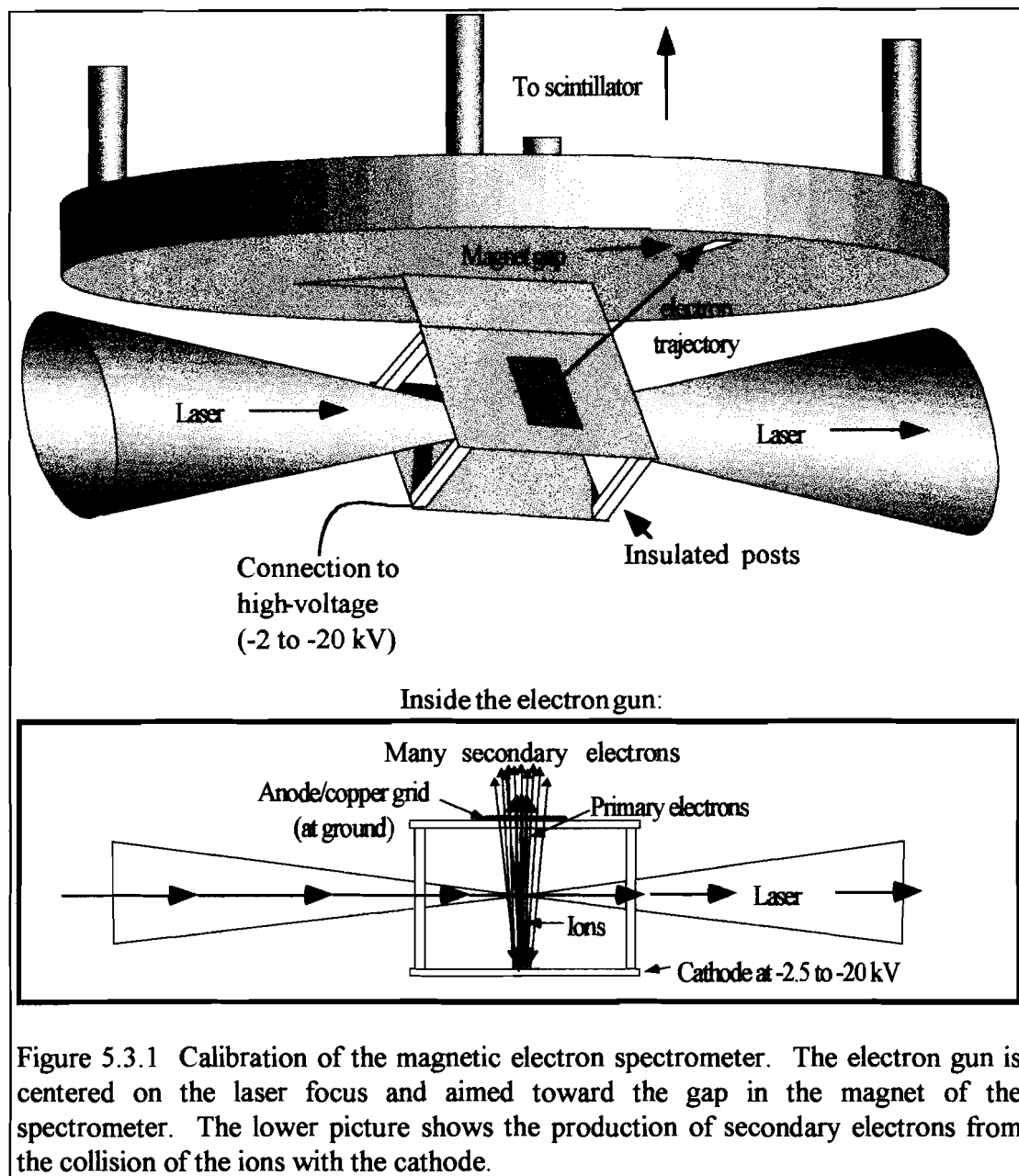
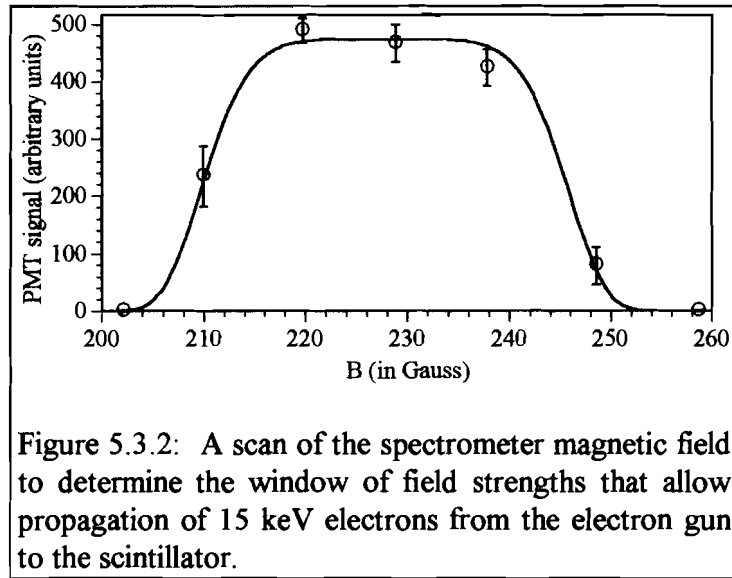


Figure 5.3.1 Calibration of the magnetic electron spectrometer. The electron gun is centered on the laser focus and aimed toward the gap in the magnet of the spectrometer. The lower picture shows the production of secondary electrons from the collision of the ions with the cathode.

The electrons were determined to be secondary electrons from ions striking the cathode by the observation of a significant time delay between the laser ionization of the gas and subsequent detection of the electrons. The time-of-flight (TOF) of

electrons from the center of the electron gun to the scintillator is on the order of 10 ns for all applied voltages. Multiple peaks in time detected on the order of a 100 ns after ionization were observed. The delay



was due to the TOF of the ions in the electron gun as they traveled to the cathode. The multiple peaks were due to multiple charge states of the ionizing gas. Examination of helium, neon and xenon showed peaks at times in excellent agreement with the TOF of the ions in the electron gun. No significant signal from the primary electrons was observed.

The electrons were detected if the magnetic field was of the proper strength to cause the gyration radius necessary for propagation to the scintillator. Since the electron energy was known from the applied potential to the plates, the magnetic field could be adjusted until electrons were visible on the scintillator, and the magnetic field corresponding to that electron energy was determined (see Figure 5.3.2).

A series of the required magnetic fields for the applied potentials to the electron gun was measured using this technique (see Figure 5.3.3). These points were least-squares fit using equation (5.2.6) with the gyration radius as the curve-fit

parameter. This determined the gyration radius as 1.54 cm, in excellent agreement with the theoretical prediction of 1.52 cm.

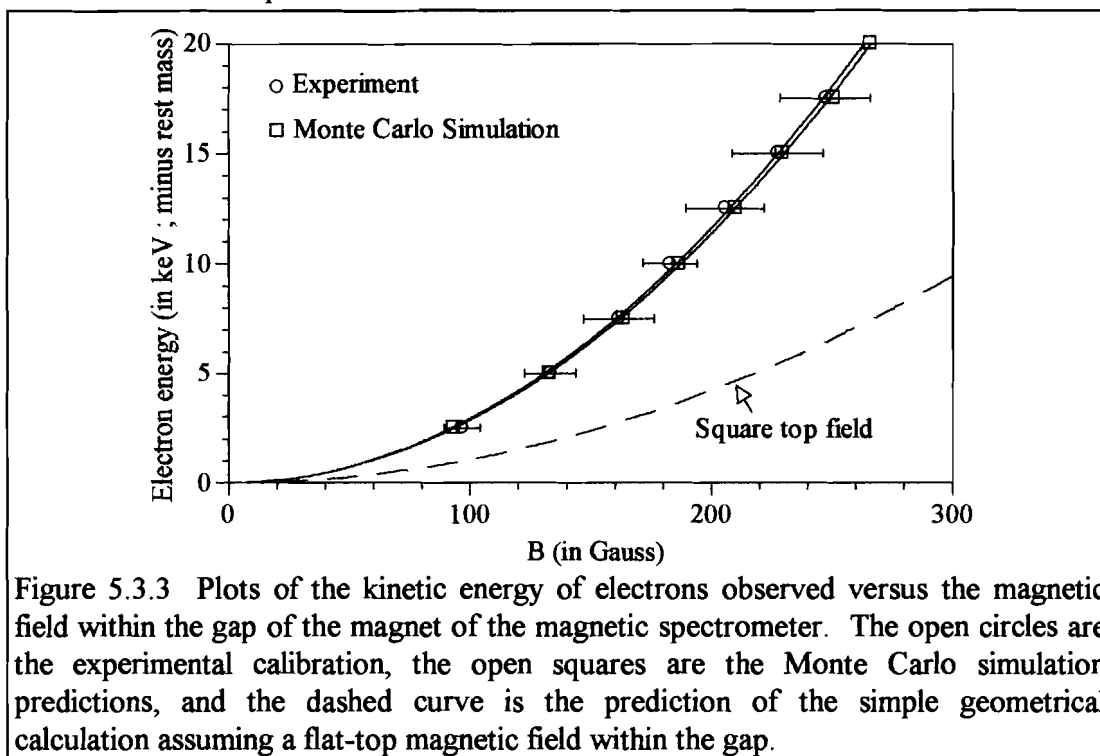


Figure 5.3.3 Plots of the kinetic energy of electrons observed versus the magnetic field within the gap of the magnet of the magnetic spectrometer. The open circles are the experimental calibration, the open squares are the Monte Carlo simulation predictions, and the dashed curve is the prediction of the simple geometrical calculation assuming a flat-top magnetic field within the gap.

The magnetic field in the gap of the magnet causes electrons entering the gap to be projected on the scintillator. The Monte Carlo simulation predicts monoenergetic electrons are projected onto a strip approximately 3 cm long. An aluminum mask blocking all but a 3-cm wide strip is therefore placed over the scintillator to maximize the energy resolution of the spectrometer. With this mask in place, the resolution of the spectrometer is found experimentally as $\Delta E/E \approx 30\%$ FWHM, i.e., the FWHM of a monoenergetic electron peak is 30% of the energy of the peak (see Figure 5.3.4).

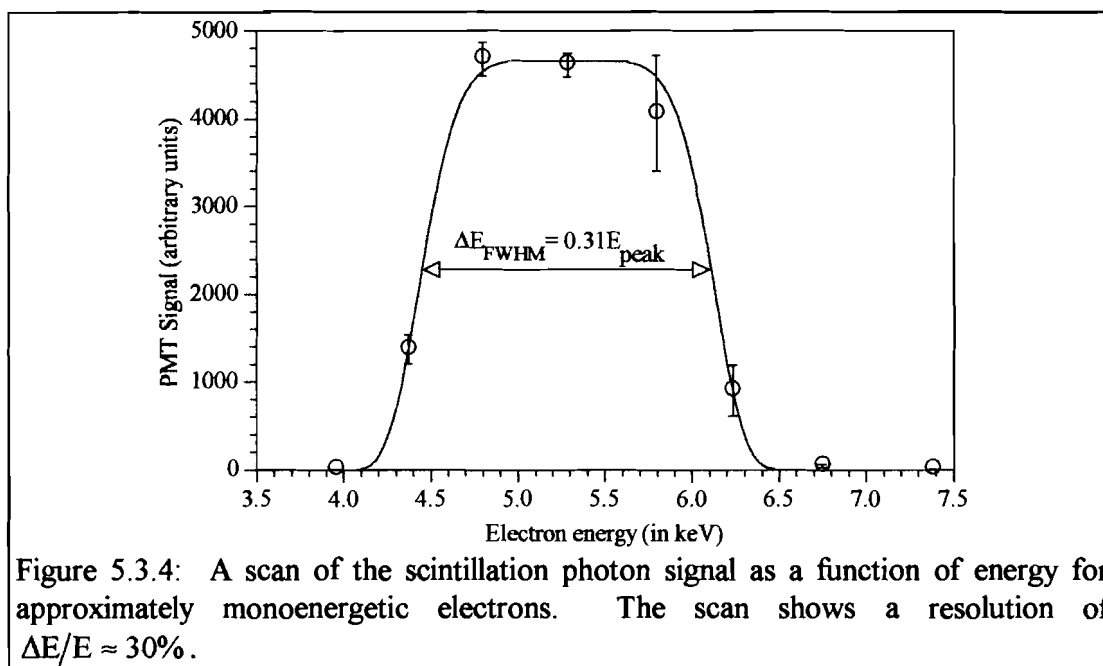


Figure 5.3.4: A scan of the scintillation photon signal as a function of energy for approximately monoenergetic electrons. The scan shows a resolution of $\Delta E/E \approx 30\%$.

5.4 Measurement of the angular distribution of the electrons

The center of the scintillator disk, the center of the magnet, and the laser focus lie on a single line. This is the central axis of the spectrometer. The alignment of the focus to the central axis of the spectrometer is accomplished by viewing a laser induced discharge in air through a 0.5-mm hole in the bottom disk of the spectrometer.

A PMT was placed above the output window of the spectrometer looking through the hole. A low-energy laser pulse (approximately 1 mJ) was fired through the lens into the vacuum chamber, which was open to air. The position of the focus was moved by adjusting the focusing lens. The position of the lens was set so that the signal observed by the PMT from the discharge in the focus was maximized. The hole is blocked for standard operation of the spectrometer.

The plane of the gap in the magnet passes through the central axis which assures that a line of sight can always be traced from the laser focus through the gap. This is an important aspect of the magnet and spectrometer because rotation of the magnet and entire spectrometer around the central axis maintains the ability to trace a clear line of sight from the laser focus through the gap, regardless of the rotation angle of the spectrometer. This allows measurement of the angular distributions of the electrons relative to the laser axis. The 2-mm width of the gap in the magnet corresponds to a 2° angle over which electrons are accepted to the spectrometer.

Figure 5.4.1 shows the detection angle of the spectrometer as it is rotated. Since the magnet rotates in a plane above the laser axis, the angle of rotation of the spectrometer, ϕ , is different from the angle between an electron trajectory from the laser focus to the gap and the laser axis, θ . These angles are related by,

$$\cos\theta = \cos 45^\circ \cdot \cos\phi \quad (5.4.1)$$

Ionization and subsequent acceleration of electrons from a circularly polarized Gaussian laser focus must cause a cylindrically symmetric distribution of ejected electrons about the beam axis due to the symmetry of the laser. A measurement of the angular distributions of 4 keV electrons ejected from N^{4+} in a circularly polarized focus showed an asymmetry in the spectrometer. These electrons were observed at $\phi=81.9^\circ$ on one side of the focus and at $\phi=93.2^\circ$ on the opposite side of the focus, i.e., with the spectrometer rotated approximately 180° (see Figure 5.4.2).

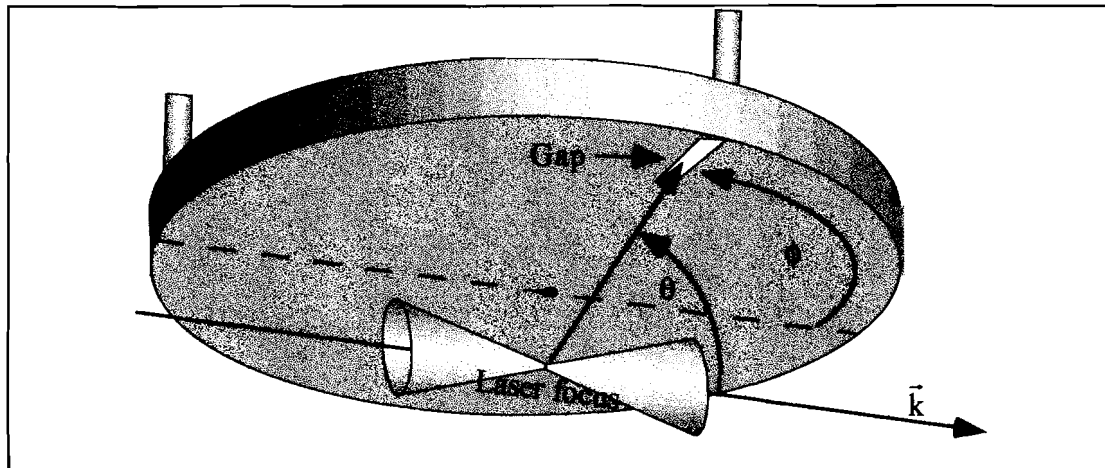


Figure 5.4.1 The angular distribution is measured by rotating the entire spectrometer. ϕ is the angle of rotation of the spectrometer. θ is the angle between an electron trajectory from the laser focus to the gap and the laser axis.

The asymmetry is believed to be due to a 2° tilt in the magnetic field of the spectrometer that curves the electrons in the z -direction as defined in Figure 5.2.10. In circular polarization, the focus is symmetric and the only explanation for this asymmetry is in the spectrometer. The shift can therefore be taken into account by simply rotating the observed angular distributions by a ϕ of $5.7^\circ \pm 0.5^\circ$ (see Figure 5.4.3). Measurement of high-energy electrons (80 keV) from neon confirm that a rotation by $\phi=5.7^\circ$ corrects this asymmetry. The asymmetry causes an increase in the uncertainty of the measured angles from $\pm 10^\circ$ due to the geometrical acceptance angle of the magnet gap to $\pm 15^\circ$ due to the added uncertainty from the asymmetry.

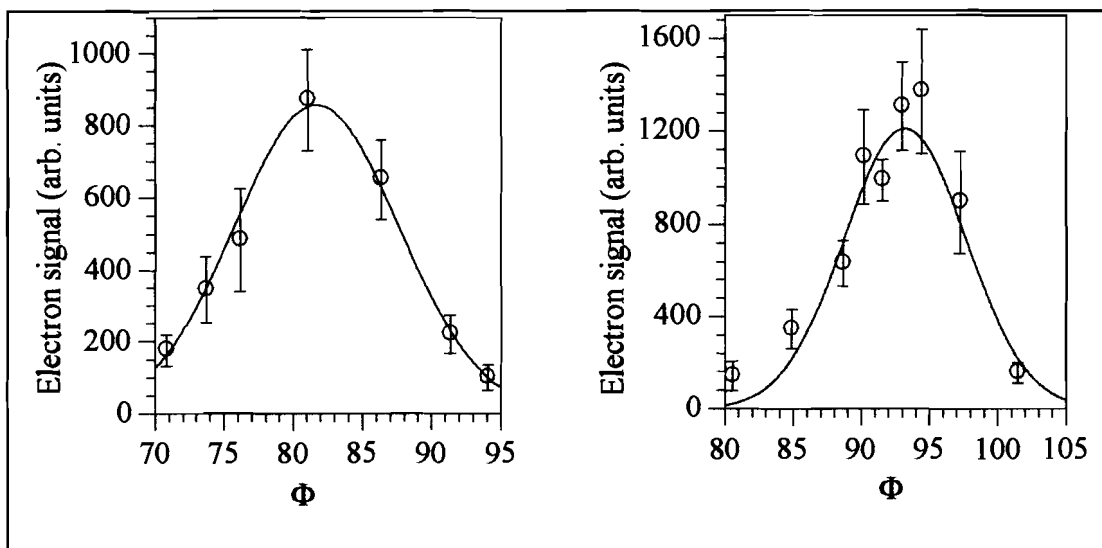


Figure 5.4.2: The angular distributions of 4 keV electrons from Nitrogen on opposite sides of the laser focus.

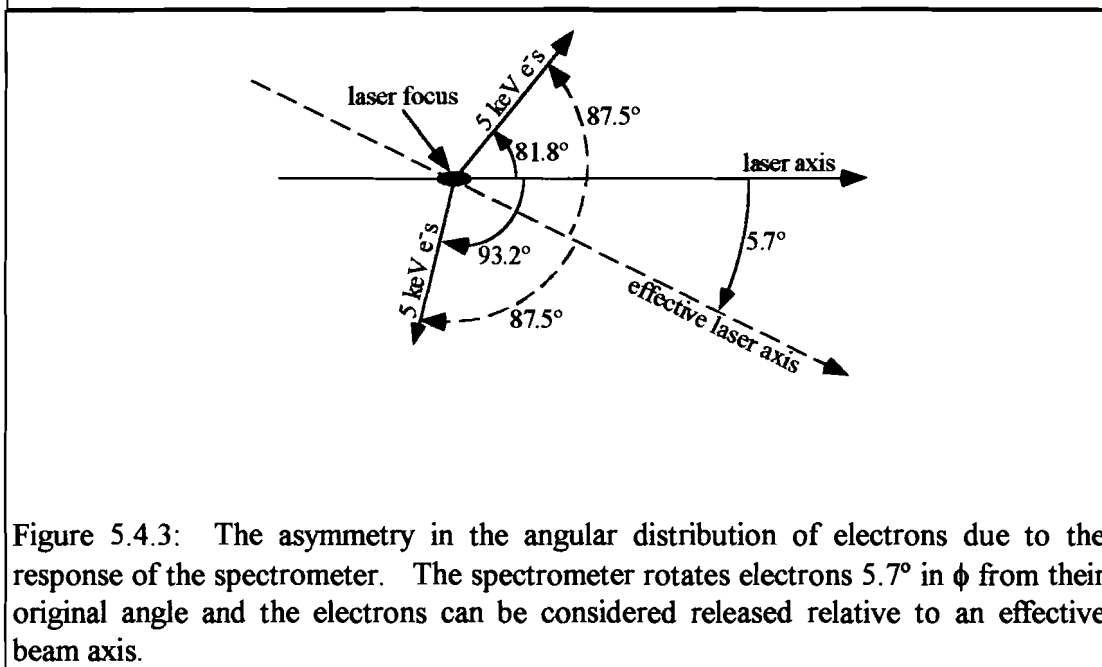


Figure 5.4.3: The asymmetry in the angular distribution of electrons due to the response of the spectrometer. The spectrometer rotates electrons 5.7° in ϕ from their original angle and the electrons can be considered released relative to an effective beam axis.

5.5 Energy spectrum of helium

An examination of the energy distribution of electrons ejected from helium at 85.0° from \vec{k} using circular polarization was conducted. This scan is used to verify

the expectation that the energy of the ejected electrons is approximately twice the ponderomotive potential as predicted in chapter 3. Confirmation that the electrons are ejected with $2\Phi_p$ of energy allows the categorization of the different peaks to the different charge states in the more complicated energy spectrums of neon. It is also useful in testing the accuracy of the Monte Carlo simulation.

The BSI threshold intensity in circular polarization for the creation of He^{2+} is $1.76 \times 10^{16} \text{ W/cm}^2$. This corresponds to a ponderomotive energy of 1.82 keV or an expected ejection energy of 3.64 keV. The Monte Carlo prediction of the energy of the ejected electrons is 3.4 keV. The slightly lower energy of the simulation is due to the 500-fs interaction time (see section 3.4) of these low-energy electrons. This is only a factor of 3 less than the pulse width of the laser, 1.5 ps, so the electrons acquire only 87% of the ponderomotive energy.

The measured energy spectrum and the Monte Carlo simulation prediction are shown in Figure 5.5.1. A single peak in the data is evident at 3.0 keV. This is the highest energy peak visible from the ionization of helium (see Figure 5.5.1 inset). These electrons must therefore be generated in the creation of He^{2+} , or fully stripped helium. The energy is within 12% of the prediction of the Monte Carlo simulation.

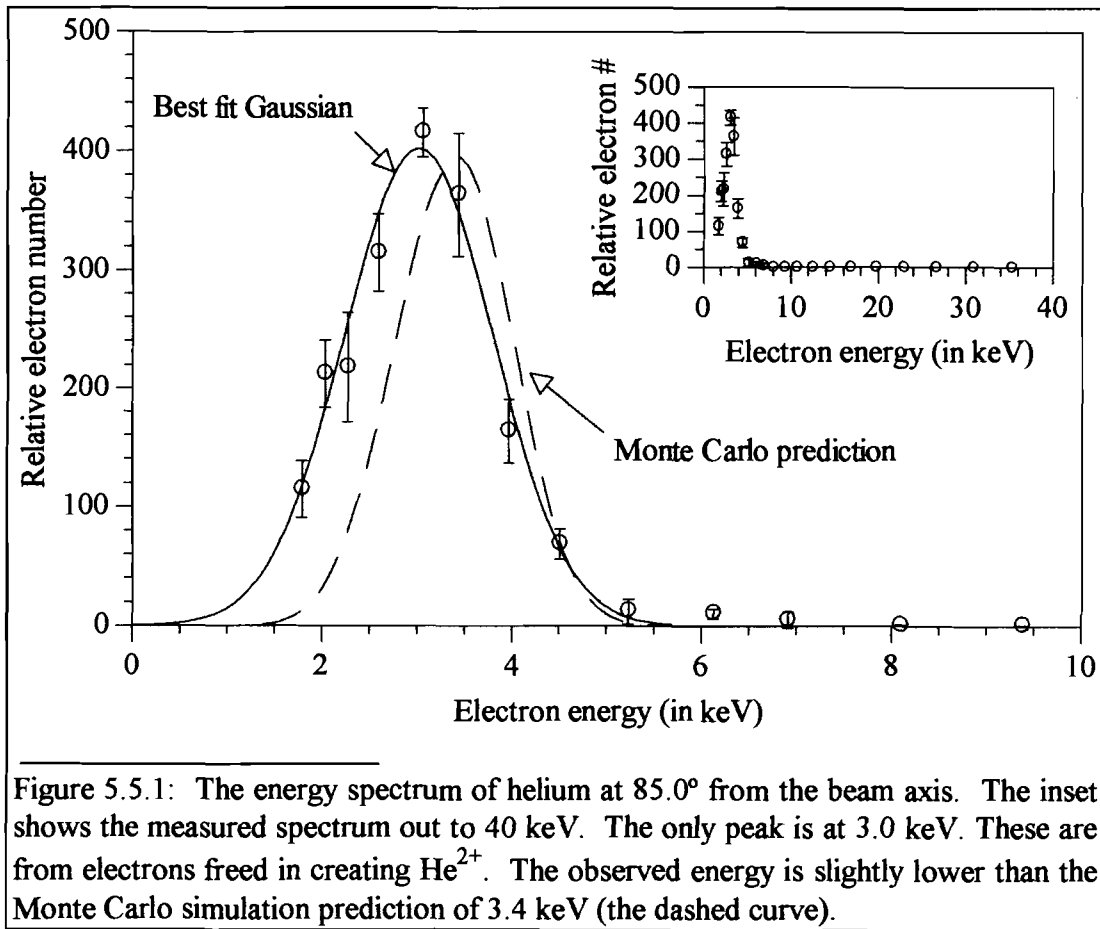


Figure 5.5.1: The energy spectrum of helium at 85.0° from the beam axis. The inset shows the measured spectrum out to 40 keV. The only peak is at 3.0 keV. These are from electrons freed in creating He^{2+} . The observed energy is slightly lower than the Monte Carlo simulation prediction of 3.4 keV (the dashed curve).

The slight difference in the Monte Carlo prediction and the observed energy is unimportant for the main goal of the helium experiment. The main goal is to determine the validity of our predictions for the electron energy. The energies agree well enough (within 12%) to allow the categorization of the peaks in the energy spectrum of neon to their particular charge states. The absence of high-energy electrons also confirms that no plasma physics mechanisms are generating energetic electrons. Only single particle interactions with the field are significant.

-
- ¹ P. Maine, D. Strickland, P. Bado, M. Pessot and G. Mourou, "Generation of ultrahigh peak power pulses by chirped pulse amplification," *IEEE J. Quantum Electron.* QE-24, 398 (1988).
- ² Y.-H. Chuang, D.D. Meyerhofer, S. Augst, H. Chen, J. Peatross, and S. Uchida, "Pedestal suppression in a chirped pulse amplification laser," *J. Opt. Soc. Am. B* 8, 1226 (1991).
- ³ Joseph W. Goodman, *Introduction to Fourier Optics*, (McGraw-Hill, 1968, San Francisco).
- ⁴ J.B. Birks, *The Theory and Practice of Scintillation Counting*, (Macmillan, New York, 1964).
- ⁵ John O'Malley, *Basic Circuit Analysis*, (McGraw-Hill, New York, 1982), p. 127.
- ⁶ Paul Horowitz and Winfield Hill, *The Art of Electronics*, (Cambridge, 1980), p.1007.
- ⁷ *American Institute of Physics Handbook*, edited by Dwight E. Gray, (McGraw-Hill, New York, 1972), -Section 8, page 182.
- ⁸ John David Jackson, *Classical Electrodynamics* 2nd edition, (Wiley, New York, 1962).
- ⁹ G. Carter and J.S. Colligon, *Ion Bombardment of Solids*, (American Elsevier, New York, 1968).

Chapter 6

Experimental observations of the electron distributions

Observations of the forward drift of electrons due to high-intensity Compton scattering in an optical laser focus are presented in this chapter. The first section discusses the steps involved in acquiring the electrons' energy spectra at a variety of angles. The analysis of the energy spectra and their conversion to the angular distributions for each charge state are addressed in section 6.2. The final section presents the angular distributions and their confirmation of the forward drift due to high-intensity Compton scattering.

6.1 Acquisition

The energy and angular distribution of the electrons is measured with the magnetic spectrometer by varying the spectrometer's magnetic field and rotation angle. Measurement of the electron energy spectra from 2 keV to 100 keV at nine angles is accomplished using the following methods.

The spectrometer is placed above the laser focus with the gap at one specific angle from \vec{k} . The vacuum tank is filled with neon at 10^{-3} Torr of pressure. An energy spectrum is generated by varying the magnetic field in the spectrometer to map

out the electrons' energy distribution. The energy scan begins at a magnetic field corresponding to an electron energy of approximately 2 keV. Five circularly polarized laser shots with a peak intensity of approximately 10^{18} W/cm² are taken. The electron signal from the spectrometer is digitized with a 2249w Analog-to-Digital converter (ADC), and the number of counts is recorded for each shot. The energy and pulse width of the laser are also recorded to allow determination of the laser's intensity. The vacuum tank is then pumped out to minimize contamination in the tank. The magnetic field is increased by an amount corresponding to an energy increase of one-quarter the resolution limit of the spectrometer, or $(0.075)E$. This insures that even a monoenergetic electron peak is not "skipped over" in the scan. The tank is refilled, five more shots are taken and the signals recorded. The tank is pumped out and the magnetic field increased, etc.

The energy scan results in measurements of the electron signal for energies from 2 keV to 100 keV at the angle of observation of the spectrometer. The spectrometer is then rotated to a different angle with respect to \vec{k} and the energy scan is repeated. This process is used to measure the electrons' energy spectra at nine different angles, 69.9° to 92.5° with respect to \vec{k} .

6.2 Analysis

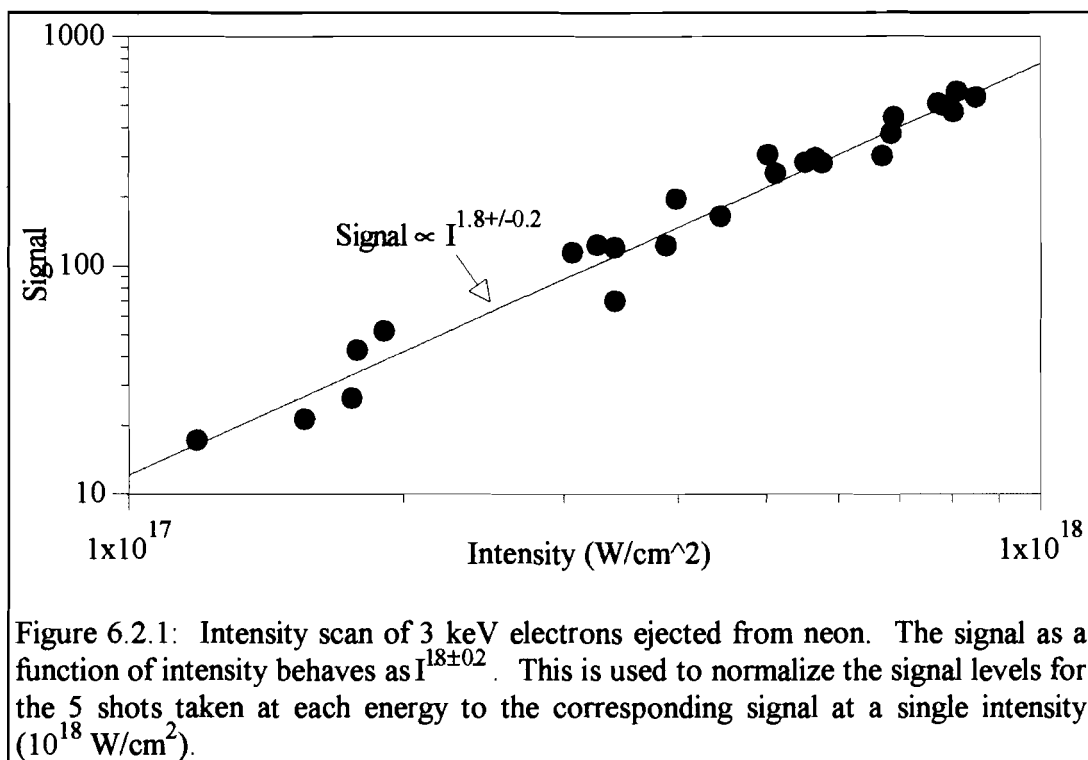
The number of electrons striking the scintillator (N_e) for each laser shot is calculated using equation (5.2.15),

$$N_e \approx 125 \frac{N_c}{E(\text{in keV})},$$

where N_c is the number of counts from the ADC and E is the energy setting of the spectrometer.

The laser fluctuates in intensity from shot-to-shot by as much as 50%. The number of electrons varies as a function of the intensity because of the change in the number of ionized atoms. As a result, the spectrometer's signal level must be normalized to eliminate these fluctuations and allow averaging of the five signal levels at each magnetic field setting.

The normalization is accomplished by examining the signal level as a function



of intensity and normalizing the signal level to a single intensity (10^{18} W/cm² was used for all of the data). An example of an intensity scan of 3 keV electrons ejected from neon is shown in Figure 6.2.1. The signal varies as $N_e \propto I_0^{1.8 \pm 0.2}$, where I_0 is the peak intensity of the laser pulse. This relation is due to the intensity dependence of the size of the focal volume.

The focal volume is the volume within the laser focus where the intensity exceeds the threshold intensity (intensity required for ionization) of the atom or ion at the peak of the laser pulse.¹ The intensity distribution of a Gaussian laser focus is given by

$$I(\vec{r}, t) = I_0 \left(\frac{w_0}{w(z)} \right)^2 \exp \left(-2 \left(\frac{r}{w(z)} \right)^2 \right) f(t), \quad (6.2.1)$$

where

$$w(z) \equiv w_0 \sqrt{1 + \left(\frac{z}{z_0} \right)^2}$$

and $f(t)$ describes the temporal envelope and is always ≤ 1 . The peak intensity reached at any position is given by equation (6.2.1) with $f(z, t)$ replaced by 1,

$$I_{\text{peak}}(\vec{r}, t) = I_0 \left(\frac{w_0}{w(z)} \right)^2 \exp \left(-2 \left(\frac{r}{w(z)} \right)^2 \right). \quad (6.2.2)$$

The maximum radius at which ionization can occur (the radius where the maximum intensity reached is the threshold intensity) is

$$r_{th} = w(z) \left\{ \ln \left[\left(\frac{I_0}{I_{th}} \left(\frac{w_0}{w(z)} \right)^2 \right)^{1/2} \right] \right\}^{1/2}, \quad (6.2.3)$$

where I_{th} is the threshold intensity. The maximum axial position at which ionization can occur is

$$z_{th} = z_0 \left(\frac{I_0}{I_{th}} - 1 \right)^{1/2}. \quad (6.2.4)$$

The volume enclosed by r_{th} and z_{th} is the focal volume,

$$V = \int_{-z_{th}}^{z_{th}} \pi r_{th}^2 dz \quad (6.2.5)$$

or

$$V = \frac{2\pi w_0^2 z_0}{9I_{th}^{3/2}} \left\{ (5I_{th} + I_0)(I_0 - I_{th})^{1/2} - 6I_{th}^{3/2} \tan^{-1} \left(\left(\frac{I_0 - I_{th}}{I_{th}} \right)^{1/2} \right) \right\}. \quad (6.2.6)$$

The focal volume as a function of I_{th}/I_0 is shown in Figure 6.2.2. Also plotted is the limit of equation (6.2.6) for $I_{th} \ll I_0$,

$$V = \frac{2\pi w_0^2 z_0}{9} \left(\frac{I_0}{I_{th}} \right)^{3/2}. \quad (6.2.7)$$

For $I_{th} < 0.4I_0$, equation (6.2.7) agrees well with equation (6.2.6). $I_{th} < 0.4I_0$ is valid for all of the electrons observed in these experiments. The number of electrons ionized from each charge state can

then be approximated by,

$$N \approx \frac{2\pi\rho w_0^2 z_0}{9} \left(\frac{I_0}{I_{th}} \right)^{3/2} \quad (6.2.8)$$

where ρ is the neon density.

This $I^{1.5}$ intensity dependence of the number of electrons ionized in the focus is in rough agreement with the measured $I^{1.8 \pm 0.2}$ intensity dependence.

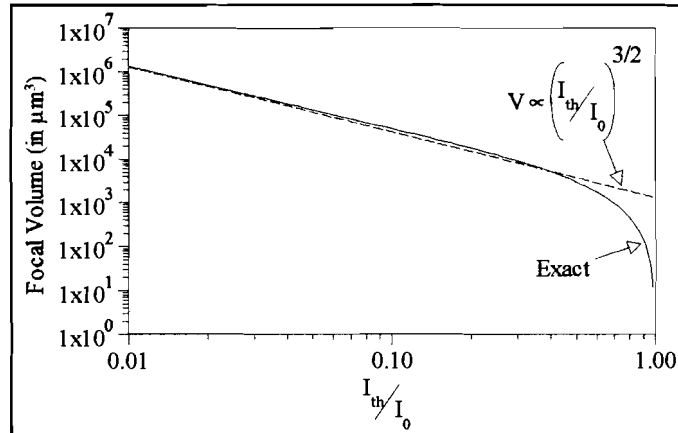


Figure 6.2.2: The size of the focal volume of a Gaussian laser profile as a function of the ratio of the threshold intensity to the peak intensity of the laser pulse. For $I_{th} < 0.4I_0$, the functional dependence of the focal volume is closely approximated by $(I_{th}/I_0)^{3/2}$.

The slight discrepancy is possibly the result of the non-Gaussian nature of the laser profile described in section 5.1, or an intensity dependence of the collection efficiency of the spectrometer.

Intensity scans at a large variety of electron energies (3, 7, 15, and 80 keV) have been performed, and all show this $I_0^{1.8 \pm 0.2}$ intensity dependence. By multiplying the number of electrons for each shot by $(I_{norm}/I_0)^{1.8 \pm 0.2}$, the number is normalized to the intensity I_{norm} (10^{18} W/cm² was used in the analysis). This eliminates the intensity fluctuations of the laser and allows the averaging of the five shots taken at each energy

setting. The uncertainty in the normalization exponent of ± 0.2 introduces a maximum error of $\pm 30\%$ in the normalized electron numbers.

Ejection energies of approximately $2\Phi_p$ are expected, where the ponderomotive potential is calculated at the threshold intensity of each charge state. This energy is expected from the conservation of canonical momentum in a circularly polarized field and the acceleration from the ponderomotive potential (see section 3.2). The BSI threshold intensities and corresponding ejection energies from the neon charge states studied in these experiments are shown in Table 3.

The energy spectrum of neon taken at 87.3° with respect to \vec{k} is shown in Figure 6.2.3. This figure shows the expected behavior of the energy spectrum. Peaks in the spectrum corresponding to different charge states (Ne^{3+} to Ne^{5+}) are observed with energies of approximately twice the ponderomotive

Ne	$I_{\text{thresh}}(\text{W}/\text{cm}^2)$	$2\Phi_p(\text{keV})$
3^+	1.4×10^{16}	3.0
4^+	4.4×10^{16}	9.1
5^+	8.0×10^{16}	17
6^+	1.4×10^{17}	29
7^+	3.0×10^{17}	62
8^+	4.0×10^{17}	83

Table 3: Ionization threshold intensities, I_{thresh} , and expected ejection energies, $2\Phi_p$, of the neon charge states studied in the experiments.

energy of each charge state's BSI threshold intensity. The electron energy spectra at all measured angles are shown in Appendix D. These spectra show electrons from Ne^{3+} up to Ne^{8+} and continued agreement with the predicted energies.

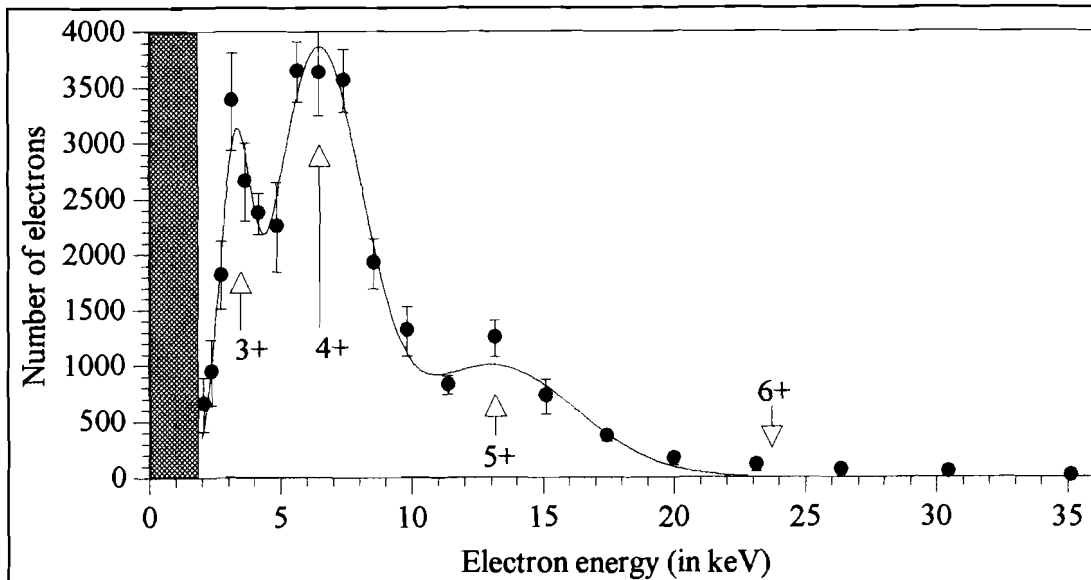
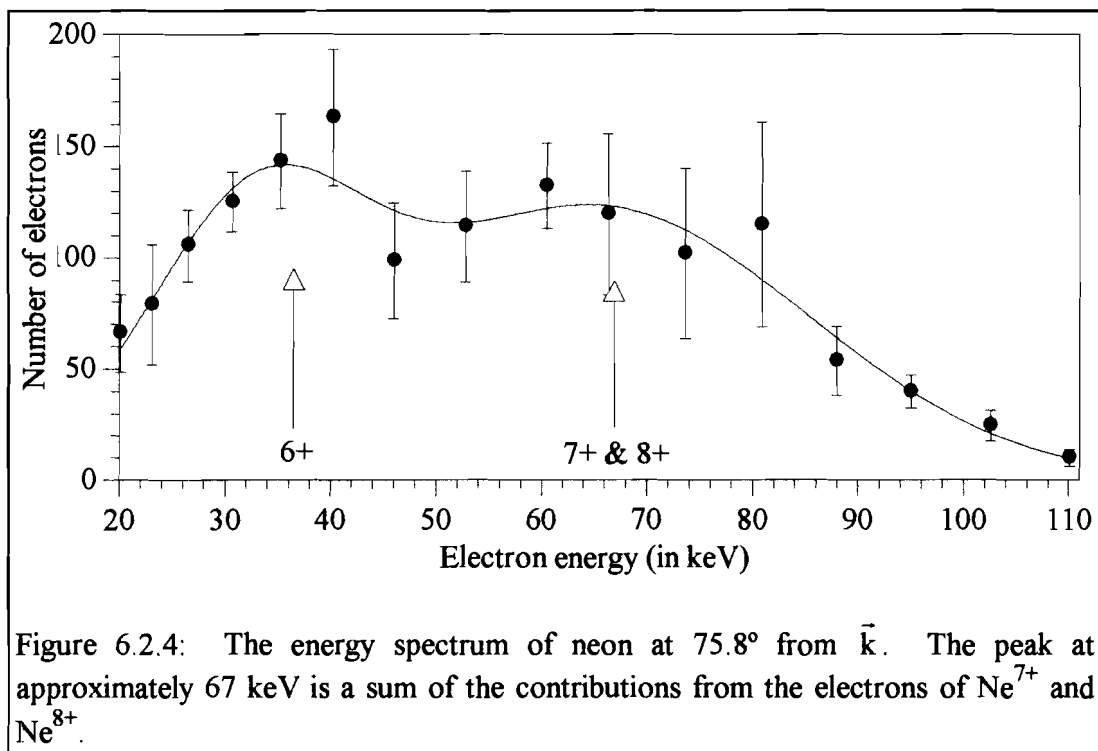


Figure 6.2.3: The electron energy spectrum of neon at 87.3° from \vec{k} . Three distinct peaks corresponding to Ne^{3+} , Ne^{4+} , and Ne^{5+} are shown by the positions of the arrows. The cross hatched area below 2 keV is not measurable with the spectrometer.

The energy distribution measured at 75.8° is shown in Figure 6.2.4. This spectrum illustrates the difficulties in extracting an angular distribution for each charge state. The peak at approximately 65 keV is a combination of electrons from Ne^{7+} and Ne^{8+} . The two peaks are not resolvable.

The following paragraph demonstrates the method used to determine the individual charge state's contributions. Figure 6.2.5 shows the electron energy distribution of neon at 78.8° , and Figure 6.2.6 shows the energy distribution at 69.9° . These spectra show a peak at 60 keV for 78.8° and a peak at 85 keV for 69.9° . In these spectra, the individual peaks of the 7^+ (60 keV) and the 8^+ (85 keV) charge states are visible. A Gaussian curve fit to these resolvable peaks is used to determine the energies and widths of each charge state's electron peak. The centroids and



widths of two Gaussians are then fixed at these energies and widths. The sum of the two Gaussians is then least-squares fit to the electron spectra at 75.8° with only the two peak heights as the fit parameters. The two peak heights give the contributions of the individual charge states.

This method is generalized to find the number of electrons contributed by all of the observed charge states at all angles. The width and energy of each charge state is determined from all clearly resolvable electron peaks. The same charge states are resolvable at a few different angles, allowing a few different values of each charge state's energies and widths to be determined. These are then averaged. The

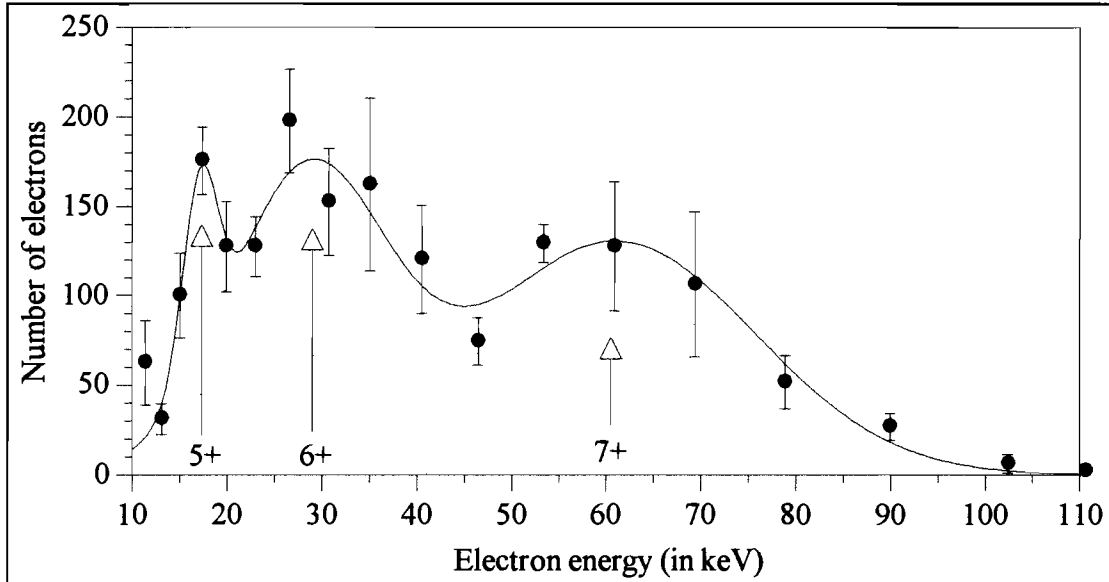


Figure 6.2.5: The energy spectrum of neon at 78.8° from \vec{k} . The peak at approximately 60 keV is almost entirely electrons from Ne^{7+} . This allows determination of the energy and width of the peak from the Ne^{7+} electrons.

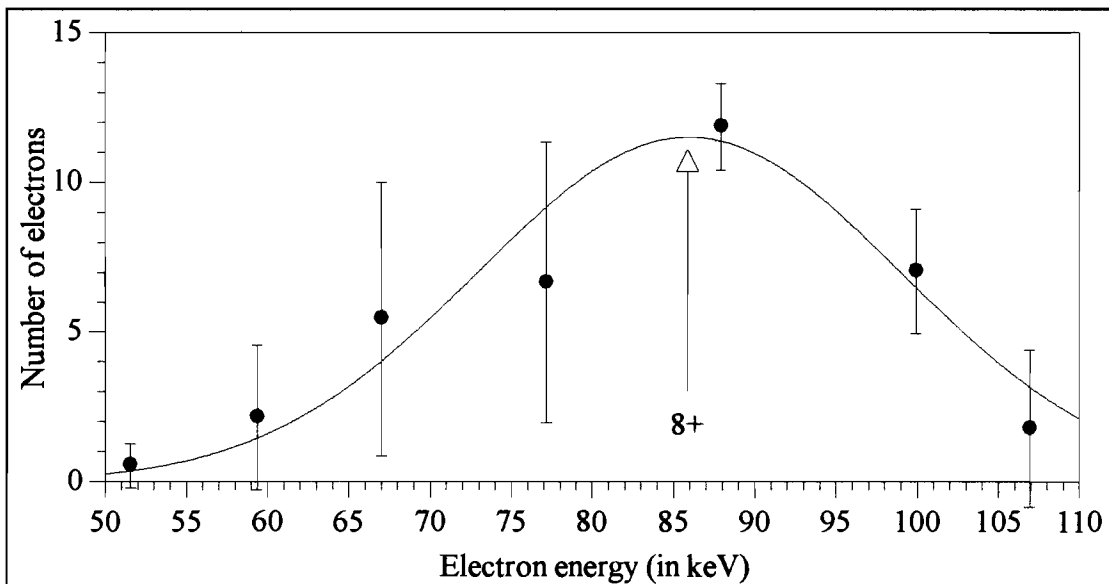


Figure 6.2.6: The energy spectrum of neon at 69.9° from \vec{k} . The peak at approximately 85 keV is almost entirely electrons from Ne^{8+} . This allows determination of the energy and width of the peak from the Ne^{8+} electrons.

Ne	I_{thresh}	$2\Phi_p$	$E_{\text{M.C.}}$ (in keV)	\bar{E}_n (in keV)	\bar{w}_n (in keV)
1 ⁺	1.7×10^{15}	360 eV	0.186 +/- 0.005	-	-
2 ⁺	5.6×10^{15}	1.2 keV	0.662 +/- 0.020	-	-
3 ⁺	1.4×10^{16}	3.0 keV	2.89 +/- 0.05	3.11 +/- 0.30	0.99 +/- 0.15
4 ⁺	4.4×10^{16}	9.1 keV	8.83 +/- 0.19	6.49 +/- 0.59	2.21 +/- 0.40
5 ⁺	8.0×10^{16}	17 keV	16.9 +/- 0.27	14.9 +/- 2.7	4.51 +/- 2.4
6 ⁺	1.4×10^{17}	29 keV	28.6 +/- 0.41	30.9 +/- 6.0	11.3 +/- 2.3
7 ⁺	3.0×10^{17}	62 keV	61.8 +/- 1.04	54.0 +/- 9.2	11.7 +/- 6.5
8 ⁺	4.0×10^{17}	83 keV	84.2 +/- 1.63	84.2 +/- 6.2	18.9 +/- 0.4
9 ⁺	2.0×10^{20}	41 MeV	-	-	-
10 ⁺	2.8×10^{20}	58 MeV	-	-	-

Table 4: A table of the expected and observed energies and widths of the electron peaks for neon: I_{thresh} is the BSI prediction of the threshold intensity in circular polarization, $2\Phi_p$ is twice the ponderomotive energy of the threshold intensity, and $E_{\text{M.C.}}$ is the predicted ejection energy from the Monte Carlo simulation. \bar{E}_n and \bar{w}_n are the energies and widths of the ejected electrons found from averaging the resolvable peaks in the experimental energy spectra. The positions with dashes represent quantities not measurable due to the limits of the spectrometer or laser.

parameters calculated with this method are shown in Table 4. The standard deviations of the energies and widths are typically $\pm 10\%$ and $\pm 30\%$ respectively.

The average $\Delta E/E$ FWHM of the peaks is 05 ± 01 . The width of these peaks is therefore not entirely due to the resolution of the spectrometer of $\Delta E/E \approx 03$. The increased width is most likely due to the ionization process. The BSI approximation assumes ionization occurs at a single intensity which results in monoenergetic electrons due to the dependence of ejected electron energy on the ionization threshold intensity. However, ionization is actually occurring over a range of intensities due to tunneling through the Coulomb barrier (see section 2.2). This range of ionization

intensities maps into a range of electron energies and increases the width of the electron peaks.

The average energies and widths are used in a sum of six Gaussian distributions,

$$N_e(E, \theta) = \sum_{n=3}^8 N_n(\theta) \text{Exp} \left(- \left(\frac{E - \bar{E}_n}{\bar{w}_n} \right)^2 \right) \quad (6.2.9)$$

where $N_n(\theta)$ is the number of electrons from Ne^{n+} at each angle, and \bar{E}_n and \bar{w}_n are the average energies and widths of the electrons from Ne^{n+} shown in Table 4. For each angle θ , the coefficients $N_n(\theta)$ are found by a least-squares fit to equation (6.2.9). The $N_n(\theta)$ give the number of electrons for each charge state and allow generation of the angular distributions, which are discussed in the next section.

6.3 The observed angular distributions of electrons ejected from neon

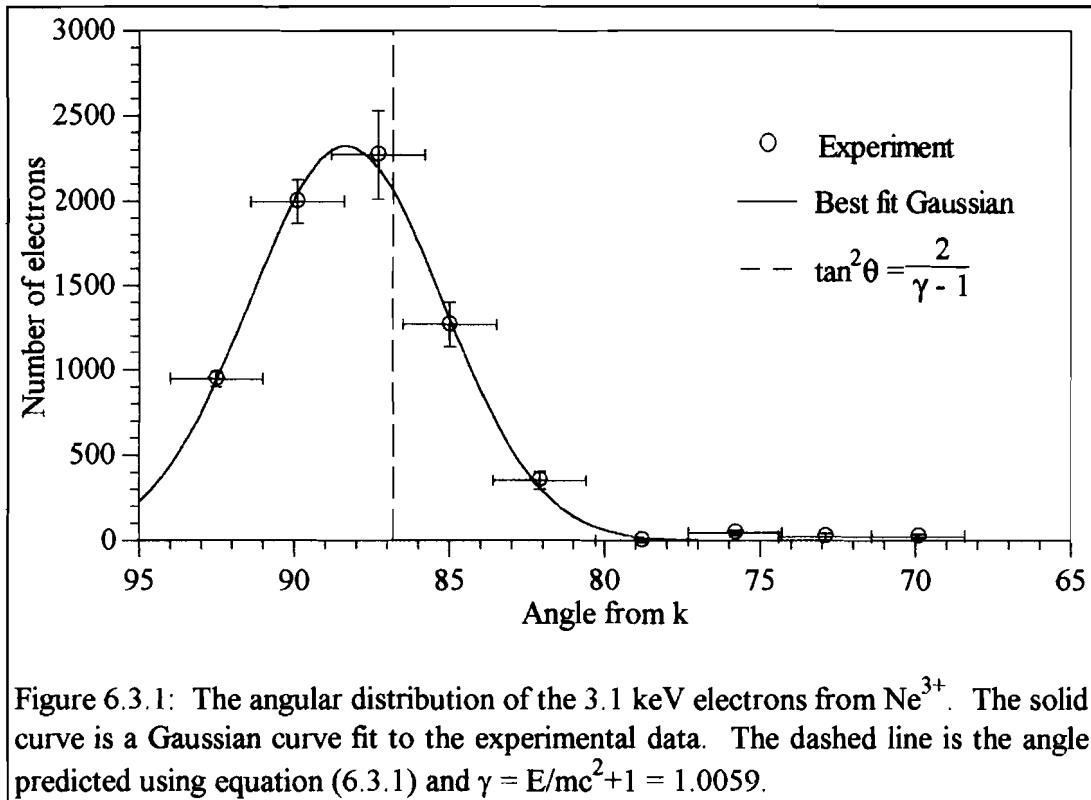
The angular distributions $N_n(\theta)$ of all observed electron peaks (from Ne^{3+} to Ne^{8+}) are shown in appendix E. The angular distributions show the effects of electron recoil due to high-intensity Compton scattering. As discussed in chapter 3, electron ejection from a low-intensity laser focus is described by the ponderomotive potential. Electron acceleration via the ponderomotive potential results in electron ejection at 90° to \vec{k} . The derivation of the ponderomotive potential, however, assumes Thomson scattering describes the electron's interaction with the field. At high intensities,

significant electron recoil due to high-intensity Compton scattering causes an additional forward component of electron momentum. The forward momentum causes the ejected electron distribution to be “pushed” forward into a cone centered on \vec{k} at high intensities. The angle of this cone is given by (see section 3.3)

$$\tan^2 \theta = \frac{2}{\gamma - 1}. \quad (6.3.1)$$

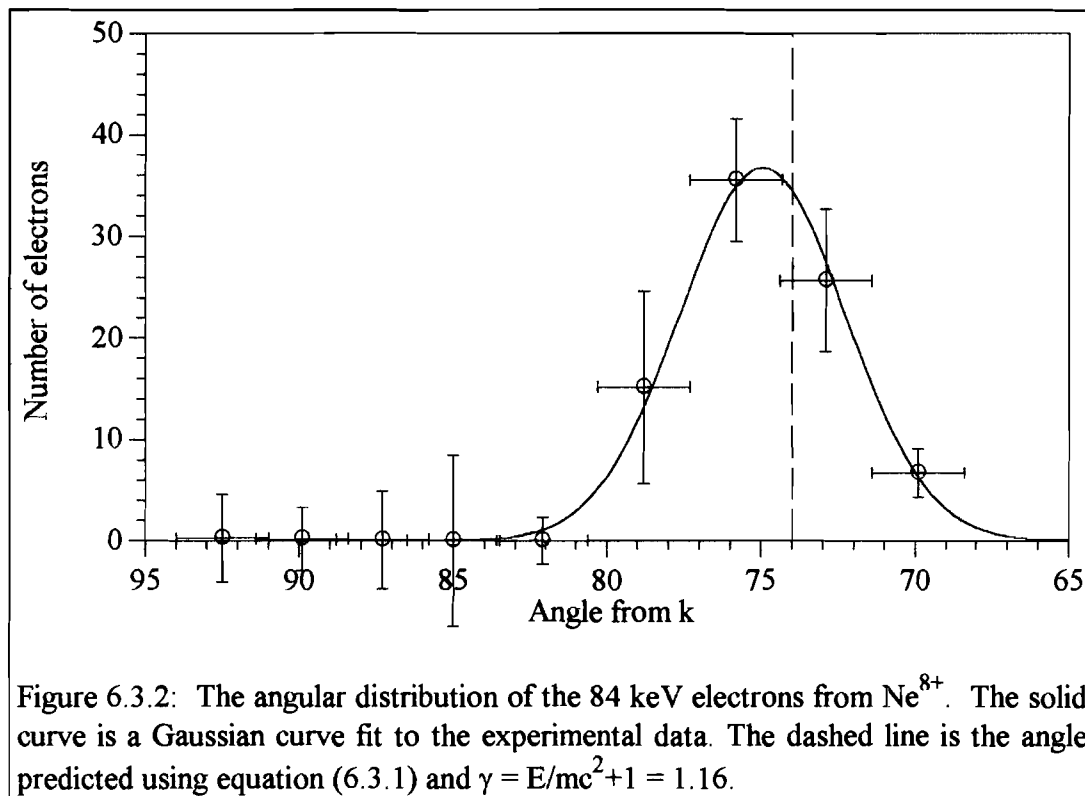
The angular distribution of electrons ejected at 3.1 keV following the creation of Ne^{3+} is shown in Figure 6.3.1. A peak is evident at 88° from \vec{k} . The solid line is a Gaussian curve fit to the data, and the dashed line is the angle predicted using equation (6.3.1) for 3.1 keV electrons.

The Ne^{3+} electrons show only a small forward shift in the angular distribution.



This is because the low energy and corresponding low intensity at which they are ionized results in minimal electron recoil and a correspondingly small forward momentum component. The predicted ejection angle of these electrons using equation (6.3.1) is 87° . This is within the 1.5° uncertainty of the observed ejection angle of 88° .

Figure 6.3.2 shows the angular distribution of electrons ejected at 84 keV following the creation of Ne^{8+} . A peak is evident at 75° from \vec{k} . These electrons are acquiring a large forward momentum component (approximately 25% of their total momentum). The forward momentum is caused by electron recoil due to absorption of momentum from the field or, equivalently, high-intensity Compton scattering. Equation (6.3.1) gives 74° from \vec{k} as the ejection angle of these electrons. This is in



good agreement with the observed angle of 75° .

Figure 6.3.3 shows the observed angle of the electron peaks associated with the ionization of the various charge states of neon versus electron energy (open circles). The solid curve shows the conservation of energy and momentum prediction of equation (6.3.1), and the solid circles represent the predicted positions of the peaks from the fully relativistic Monte Carlo simulation. The observed ejection angles are in excellent agreement with both predictions of electron recoil due to high-intensity Compton scattering (equation (6.3.1)) and the Monte Carlo simulation.

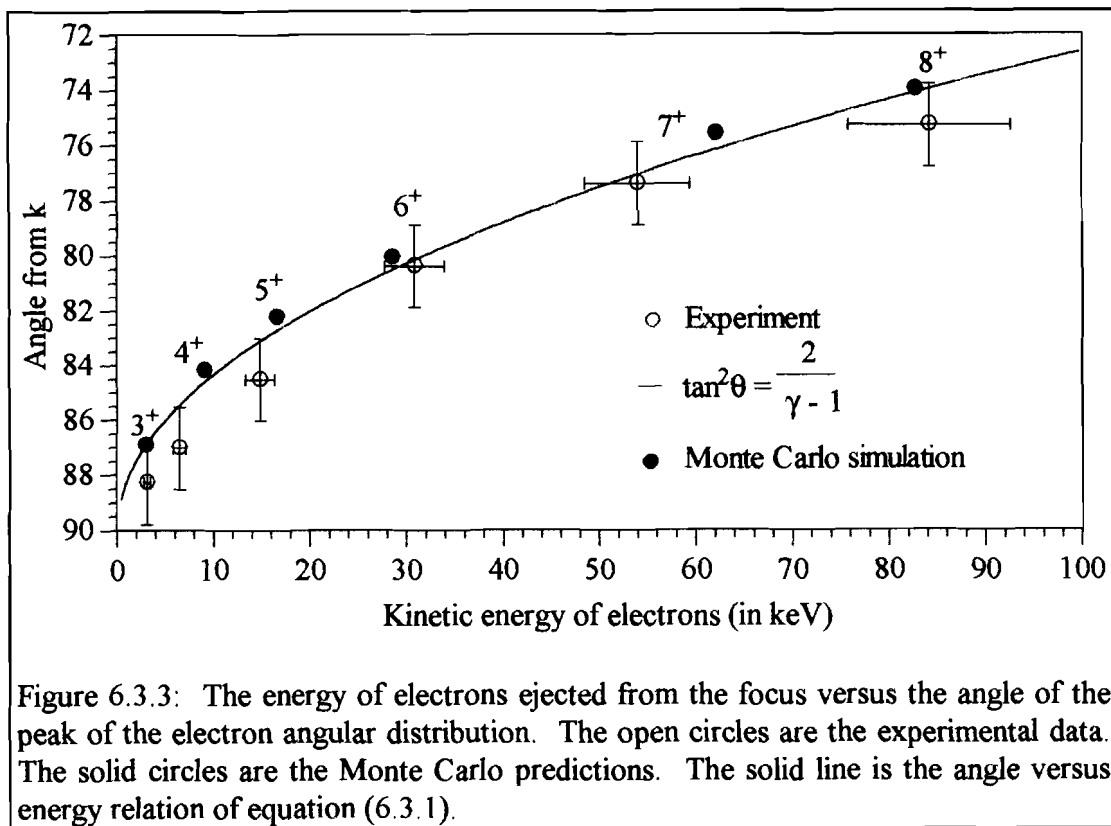


Figure 6.3.3: The energy of electrons ejected from the focus versus the angle of the peak of the electron angular distribution. The open circles are the experimental data. The solid circles are the Monte Carlo predictions. The solid line is the angle versus energy relation of equation (6.3.1).

¹ S. Augst, "Tunneling ionization of noble gas atoms using a high intensity laser at $1 \mu\text{m}$ wavelength," Ph. D. thesis, University of Rochester, 1991.

Chapter 7

Conclusions

Electrons produced from the ionization of neon and subsequently ejected from a high-intensity optical laser focus ($I \approx 10^{18} \text{ W/cm}^2$) have been investigated using an energy- and angular-resolving magnetic spectrometer. Electrons with a significant longitudinal momentum component were observed. These results were consistent with the predictions of high-intensity Compton scattering.

Electrons ionized in a laser focus are ejected from the focus with energies characteristic of their ionization threshold intensities. The 1.5-ps laser pulse duration allows complete conversion of the ponderomotive (quiver) energy of an electron to translational kinetic energy. Ionization with circular polarization also results in a nonzero initial canonical momentum, which gives the electron momentum in the plane of polarization of the laser. The combination of ponderomotive energy and conservation of canonical momentum results in electron ejection at twice the ponderomotive energy.

Electrons freed in the creation of Ne^{3+} to Ne^{8+} were observed in the experiments. The ejected energies were in good agreement with twice the

ponderomotive energy of the Barrier-Suppression-Ionization (BSI) threshold intensities of the various charge states (see Figure 7.1).

The ejected electron trajectories displayed a transition from the Thomson scattering regime to the high-intensity Compton scattering regime. The electrons ejected from the lowest charge states of neon (Ne^{3+}) interacted with relatively low

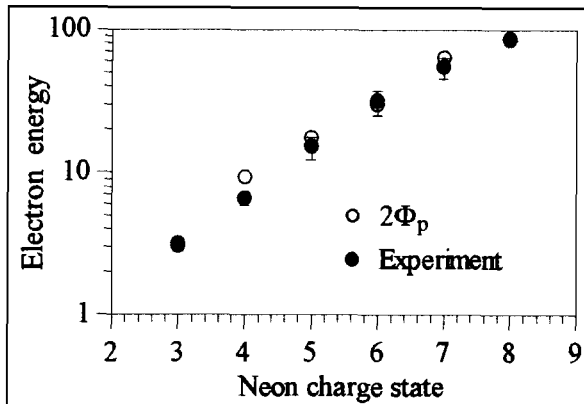


Figure 7.1: The energies of electrons from Ne^{3+} to Ne^{8+} in circular polarization. The open circles are the predicted energies (twice the ponderomotive potential of the BSI threshold intensities) and the solid circles are the observed energies.

laser intensities and displayed a small component of longitudinal momentum (approximately 3% of their total momentum). The highest charge state electrons observed (Ne^{8+}) showed a much larger component of momentum in the \vec{k} direction (approximately 25% of their total momentum). The higher charge state electrons' increased longitudinal momentum was due to field momentum or high-intensity Compton scattering effects.

Future work

The continuation of the experiments described in this thesis for higher electron energies has begun using krypton. As shown in Table 5, electrons ionized from Kr^{9+} to Kr^{18+} are predicted to gain energies from 58 keV to 870 keV based on the BSI threshold intensity. Observation of these electron energies will allow the testing of the predictions of this thesis

Kr	$I_{\text{thresh}}(\text{Circ.})$	$2\Phi_p$	θ_{eject}
9^+	$2.8 \times 10^{17} \text{ W/cm}^2$	58 keV	76.6°
10^+	4.6×10^{17}	95	73.0°
11^+	6.6×10^{17}	140	69.7°
12^+	9.2×10^{17}	190	66.7°
13^+	1.2×10^{18}	250	63.7°
14^+	1.7×10^{18}	350	59.7°
15^+	2.2×10^{18}	460	56.1°
16^+	2.8×10^{18}	580	53.0°
17^+	3.4×10^{18}	700	50.4°
18^+	4.2×10^{18}	870	47.3°

Table 5: Predicted BSI threshold intensities in circular polarization, $I_{\text{thresh}}(\text{Circ.})$, electron ejection energies, $2\Phi_p$, and ejection angle from \vec{k} , θ_{eject} , of a few charge states of Krypton. Shown are charge states for which the predicted ejection energies are near the electron rest mass, 511 keV.

in the regime where relativistic mass effects become important. Preliminary experiments in krypton have observed ejection energies and angles in good agreement with the previous predictions for up to Kr^{11+} . Intensities achievable with the current laser system should allow measurement of electrons from Kr^{18+} or electrons with energies of approximately 870 keV ($\gamma \approx 2.7$).

Other experiments will focus on the energy spectra of the ejected electrons. These contain information about the physics of the ionization process. Tunneling ionization and multiphoton ionization predict ionization to occur over a range of intensities with, a higher probability as the intensity increases. The spread in intensity

maps into a spread in the electron energy distribution due to the intensity dependence of the ponderomotive potential. Comparisons can be made between the experimentally observed widths of the electron peaks and the various theoretical predictions.

Finally, the experiments in this thesis have been performed with circular polarization exclusively. Studies using linear polarization should also be performed.

Appendix A

Monte Carlo simulation program of electron trajectories in a laser focus

The source code to solve for the electron trajectories following ionization in a laser focus is presented here. The program was written for Microsoft FORTRAN Powerstation, version 1.0 for MS-DOS and Windows operating systems. To maximize portability, FORTRAN 77 with DEC VAX FORTRAN extensions have been adhered to whenever possible. Only file access and random number generation statements need alteration for compilation with DEC VAX extensions.

```

$DECLARE
PROGRAM FOCAL_EXPLOSION_SIMULATION

*****
* THIS PROGRAM USES A MONTE CARLO SIMULATION TO CALCULATE *
* THE ELECTRONS EJECTED FROM A CIRCULARLY POLARIZED LASER FOCUSED INTO *
* A LOW DENSITY GAS. ATOMS ARE PLACED AT A RANDOM POSITION WITHIN *
* THE FOCAL VOLUME. THE TIME AT WHICH THE INTENSITY EXCEEDS THE THRESHOLD *
* INTENSITY OF THE CHARGE STATE BEING IONIZED IS CALCULATED AND THE *
* ELECTRON IS RELEASED INTO THE FIELD WITH ZERO INITIAL VELOCITY. THE *
* THE ELECTRON TRAJECTORY IS THEN CALCULATED USING THE LORENTZ FORCE OF *
* THE LASER FIELD. VELOCITIES ARE CALCULATED *
* IN UNITS OF OMEGA SO THAT POSITION AND VELOCITY ARE OF THE SAME *
* RELATIVE MAGNITUDE TO AVOID ROUND OFF ERROR. AFTER THE ELECTRON *
* ESCAPES THE LASER FOCUS, ITS POSITION, VELOCITY AND ENERGY ARE STORED *
* SO THAT OTHER PROGRAMS CAN CALCULATE ENERGY AND ANGULAR DISTRIBUTIONS *
* FROM THESE TRAJECTORIES. *
*****

*****
* VARIABLE DECLERATIONS *
*****

INTEGER NEQ, ARRTST, NUMINT, I, J, N, INITCHSTATE, IOCHECK
PARAMETER (NEQ=6, ARRTST=1000)
REAL*8 C, R0, M0, PI, ECOUL, EPS0
PARAMETER(C=2.99792458D8, R0=2.8179380D-15, EPS0=8.85418782D-12,
+ M0=511.0034D0, PI=3.14159265359D0, ECOUL=1.6021892D-19)
CHARACTER*14 FNAME, POLARIZ
CHARACTER*2 GAS
INTEGER NGAS, CHSTATE, NOK, NBAD, INDMIN, INDMAX, INDCURR
LOGICAL LINPOL, ERRFLAG
REAL*8 T, TEND, TOL, Y(NEQ), WZ, VSQR
REAL*8 INCREM, PHASE, INTENO, HMIN
REAL*8 COEF1, W0, Z0, K, OMEGA, GAMMA, H
REAL*8 ITHRESH, VX, VY, VZ
REAL*8 INTENSITY, R2, IRZ, TINDINT, SIGMAT
REAL*8 TINDPHASE
REAL*8 RMAX, VMAX, RQMAX, ZMAX, ZINIT, ARGMAX
REAL*8 EPINIT
REAL*8 NDENSE
REAL*8 PRESSURE, EPOND, ENERGY, THETAINIT, RINIT
REAL*8 IPEAK, PHIFREE, FOCALVOL
REAL*8 SCYC, EION(10, 40)
REAL SLITRES, PZ(1025), PTEMP, P
REAL VOUT(3, ARRTST), POSOUT(3, ARRTST)
INTEGER NUMTEST, FILENUM

EXTERNAL DERIVS, RKQS

COMMON /GLOB/ LINPOL, COEF1, W0, Z0, K, OMEGA, SIGMAT, GAMMA, ERRFLAG

C HELIUM IONIZATION POTENTIALS (eV)
DATA (EION(1, I), I=1, 40) /24.59, 54.42, 38*0.0/
C NEON IONIZATION POTENTIALS
DATA (EION(2, I), I=1, 40) /21.6, 41.0, 63.5, 97.1, 126.2, 158.0, 207.0,
+ 239.0, 1196.0, 1362.0, 30*0.0/

```

```

C   ARGON IONIZATION POTENTIALS
      DATA (EION(3,I), I=1,40) /15.8,27.6,40.7,59.8,75.0,91.0,124.0,
+    143.0,422.0,479.0,539.0,618.0,686.0,756.0,855.0,918.0,4121.0,
+    4426.0,22*0.0/
C   KRYPTON IONIZATION POTENTIALS
      DATA (EION(4,I), I=1,40) /14.0,24.4,37.0,52.5,64.7,78.5,111.0,
+    126.0,230.0,275.0,316.0,358.0,403.0,451.0,497.0,545.0,593.0,
+    642.0,794.0,833.0,878.0,939.0,989.0,1039.0,1151.0,1206.0,2953.0,
+    3056.0,3203.0,3381.0,3551.0,3712.0,3912.0,4105.0,17292.0,
+    17931.0,4*0.0/
C   XENON IONIZATION POTENTIALS
      DATA (EION(5,I), I=1,40) /12.1,21.2,32.1,47.6,59.0,72.0,98.0,
+    112.0,171.0,202.0,233.0,264.0,294.0,325.0,358.0,390.0,421.0,
+    452.0,573.0,608.0,643.0,678.0,726.0,762.0,853.0,891.0,1394.0,
+    1491.0,1587.0,1684.0,1781.0,1877.0,1987.0,2085.0,2183.0,2291.0,
+    2548.0,2637.0,2726.0,2814.0/

*****
*   BEGIN PROGRAM   *
*****

***** PREPARE RANDOM # GENERATOR FOR LATER USE:
      CALL SEED(-1)

      SLITRES=1.0

***** THIS OPENS THE FILE FOR INPUT WHERE ALL THE LASER AND GAS PARAMETERS
***** ARE GIVEN:
      OPEN(64,FILE='D:\FORTRAN\INPFILES\INPUT.DAT',IOSTAT=IOCHECK,
+    ERR=15,STATUS='OLD')

      GOTO 18

15   CONTINUE
*****IF REACH HERE THEN AN ERROR HAS OCCURED IN OPENING INPUT FILE*****
      IF (IOCHECK.EQ.6416) THEN
          STOP 'FILE INPUT.DAT DOES NOT EXIST!!!  ABORTING'
      ELSE
          WRITE(*,*)'UNKNOWN ERROR #',IOCHECK,' OCCURED, ABORTING.'
      ENDIF

18   CONTINUE
***** THESE READ STATEMENTS READ THE INPUT PARAMETERS TO BE USED IN THE PROGRAM.
***** INTENO = PEAK LASER INTENSITY(AT X=Y=Z=0 AND TIME=0)
***** GAS = CHARACTER VARIABLE CONTAINING GAS TO BE TESTED
***** CHSTATE = LOWEST CHARGE STATE TO BE CONSIDERED IN SIMULATION
***** W0 = 1/e^2 RADIUS OF LASER FOCUS AT BEAM WAIST
***** SIGMAT = FWHM OF LASER IN TIME
***** PRESSURE = PRESSURE IN TORR
***** TOL = THE RELATIVE ERROR TOLERANCE MAINTAINED IN ODEINT(DIFF EQN SOLVER)
***** NUMTEST=NUMBER OF ATOMS RANDOMLY PLACED WITHIN FOCUS
***** POLARIZ = CHARACTER VARIABLE SPECIFYING POLARIZATION OF LASER PULSE(CIRC OR LIN)

      READ(64,*)INTENO,GAS,CHSTATE,W0,SIGMAT,
+    PRESSURE,TOL,NUMTEST,POLARIZ
      CLOSE(64)

*****
***** THE FOLLOWING LINES INITIALIZE MANY PARAMETERS NEEDED LATER IN THE PROGRAM: *****
*****

      IF (NUMTEST.GT.ARRTEST) THEN
          WRITE(*,*) 'WITH THIS MANY ELECTRONS TESTED,'
          WRITE(*,*) 'THERE WILL BE PROBLEMS WITH ARRAY DIMENSTIONS!!!'
          STOP 'ABORTING'
      ENDIF

***** CONVERT GAS TO ARRAY #
      IF ((GAS.EQ.'HE').OR.(GAS.EQ.'He')) NGAS=1
      IF ((GAS.EQ.'NE').OR.(GAS.EQ.'Ne')) NGAS=2
      IF ((GAS.EQ.'AR').OR.(GAS.EQ.'Ar')) NGAS=3
      IF ((GAS.EQ.'KR').OR.(GAS.EQ.'Kr')) NGAS=4
      IF ((GAS.EQ.'XE').OR.(GAS.EQ.'Xe')) NGAS=5

***** THESE LINES DEFINE E0(CALLED COEF1 HERE) FOR CIRC OR LINEAR POL.
***** E0 IS THE PEAK ELECTRIC FIELD.
      IF ((POLARIZ(:1).EQ.'L').OR.(POLARIZ(:1).EQ.'l')) THEN
          LINPOL=.TRUE.

```

```

C      FOR LINEAR POLARIZATION USE:
      COEF1=DSQRT(2.0D0*INTENO*1.D4/(C*EPS0))
      ELSE
      IF ((POLARIZ(:1).NE.'C').AND.(POLARIZ(:1).NE.'c')) THEN
      STOP 'Polarization not specified, aborting...'
      ENDIF
      LINPOL=.FALSE.
C      FOR CIRCULAR POLARIZATION USE:
      COEF1=DSQRT(INTENO*1.E4/(C*EPS0))
      ENDIF

***** MINIMUM STEPSIZE ALLOWED
      HMIN = TOL/100.D0

***** SCYC = STEPS PER LASER CYCLE USED IN SOLVING DIFF EQN FOR LORENTZ FORCE
      SCYC=1.0D0

***** Z0 = CONFOCAL PARAMETER
      Z0=PI*W0**2/(1.053D-6)

***** K = WAVE NUMBER
      K=2.0D0*PI/1.053D-6

***** OMEGA = OMEGA
      OMEGA=K*C

***** INCREM = TIME INCREMENT USED IN SOLVING DIFFERENTIAL EQUATION
      INCREM=OMEGA*0.6191582391034D0/(SCYC*C/1.053D-6)

      INITCHSTATE=CHSTATE

***** OUTPUT TO LOG FILE:
      IF (LINPOL) THEN
      WRITE(*,*) 'LINEAR POLARIZATION: '
      ELSE
      WRITE(*,*) 'CIRCULAR POLARIZATION: '
      ENDIF
      WRITE(*,464) INTENO,GAS,CHSTATE,W0*1E6,SIGMAT*1E12,
+ PRESSURE,TOL*1E2
464  FORMAT(/' Peak intensity =',E13.6,' W/cm^2,',
+ /' Gas tested:',A2,'/ Lowest charge state:',I3
+ /' Beam waist =',F8.2,' microns,'/' Pulse width =',
+ F10.4,' psec,'/' Pressure =',E13.6,
+ ' torr,'/' Accurate to approximately',F10.4,' percent.'/)

      FILENUM=48
      FNAME=GAS//POLARIZ(1:3)//CHAR(FILENUM)//'.DAT'

449  CONTINUE
***** OPEN OUTPUT FILENAME.
      OPEN(65,FILE='D:\FORTRAN\OUTFILES\'//FNAME,ERR=451,
+ IOSTAT=IOCHECK,STATUS='NEW')
      GOTO 453

451  CONTINUE
*****IF REACH HERE THEN AN ERROR HAS OCCURED OPENING OUTPUT FILE*****
      IF ((IOCHECK.EQ.6415).AND.(FILENUM.LT.57)) THEN
      FILENUM=FILENUM+1
      FNAME=GAS//POLARIZ(1:3)//CHAR(FILENUM)//'.DAT'
      GOTO 449
      ELSE
      WRITE(*,*) 'UNABLE TO OPEN OUTPUT FILE, INPUT NEW NAME: '
      READ(*,'(A)') FNAME
      GOTO 449
      ENDIF

453  CONTINUE
***** THIS SECTION SENDS THE HEADER TO OUTPUT FILE.
      IF (LINPOL) THEN
      WRITE(65,*) 'LINEAR POLARIZATION: '
      ELSE
      WRITE(65,*) 'CIRCULAR POLARIZATION: '
      ENDIF
      WRITE(65,463) INTENO,GAS,INITCHSTATE,W0*1E6,SIGMAT*1E12,
+ PRESSURE,TOL*1E2,NUMTEST
463  FORMAT(/' Peak intensity =',E13.6,' W/cm^2,',
+ /' Gas tested:',A2,'/ Lowest charge state:',I3
+ /' Beam waist =',F8.2,' microns,'/' Pulse width =',

```

```

+   F10.4, ' psec, ',' Pressure =', E13.6,
+   ' torr, ',' Accurate to approximately', F10.4, ' percent. '/,
+   ' Number tested =', I5//)

*****
*****INITIALIZATION DONE ::: BEGIN MAIN LOOP*****
*****
***** THIS CONTINUE IS THE BEGINNING OF THE LOOP FOR EACH CHARGE STATE. FOLLOWING ****
***** THE COMPLETION OF THE IONIZATION OF NUMTEST ATOMS, THE PROGRAM RETURNS HERE ****
***** TO EXAMINE THE NEXT HIGHER CHARGE STATE.*****
*****
50  CONTINUE

***** THESE LINES DETERMINE THE BSI THRESHOLD INTENSITY FOR THE CURRENT CHARGE STATE AND GAS
IF (LINPOL) THEN
  ITHRESH=4.0E9*EION(NGAS,CHSTATE)**4/CHSTATE**2
ELSE
  ITHRESH=8.0E9*EION(NGAS,CHSTATE)**4/CHSTATE**2
ENDIF
C   WRITE(*,*) 'THRESHOLD INTENSITY =', ITHRESH

if ((ITHRESH.ge.inten0).OR.(ITHRESH.EQ.0.0D0)) then
  IF (CHSTATE.EQ.INITCHSTATE) THEN
    write(*,*) 'el problema, NO CHARGE STATES IONIZED!'
    goto 998
  ENDIF
  GOTO 950
endif

***** H = STEPSIZE TO BE USED BY ODEINT
H=INCREM

***** ZMAX = MAXIMUM Z VALUE WHERE ELECTRONS CAN POSSIBLY ESCAPE
ZMAX=Z0*DSQRT(INTEN0/ITHRESH-1.0D0)*.999999

***** THESE LINES CALCULATE THE FOCAL VOLUME FOR NORMALIZATION OF THE NUMBER OF
***** ELECTRONS TO THE PRESSURE SINCE NUMTEST IS ALWAYS THE NUMBER IONIZED IN THE
***** PROGRAM BUT THE ACTUAL NUMBER DEPENDS ON FOCAL VOLUME AND GAS PRESSURE.
PTEMP=0.0
DO 25 I=1,1025
  WZ=W0*DSQRT(1.0D0+(ZMAX*(I-513.)/(512.*Z0))**2)
  ARGMAX=.5D0*DLOG(INTEN0/ITHRESH*(W0/WZ)**2)
  RMAX=WZ*DSQRT(ARGMAX)
  PZ(I)=PI*RMAX**2*(ZMAX/512.)+PTEMP
  PTEMP=PZ(I)
25  CONTINUE

FOCALVOL=PZ(1025)
C   WRITE(*,*) 'FOCAL VOL =', FOCALVOL
DO 26 I=1,1025
  PZ(I)=PZ(I)/FOCALVOL
26  CONTINUE

NDENSE=3.5353D22*PRESSURE
NUMINT=NDENSE*FOCALVOL
WRITE(65,*) ' '
WRITE(65,*) 1.0E0*NUMINT/NUMTEST

*****

***** RMAX IS THE MAXIMUM RADIUS AT WHICH ATOMS CAN IONIZE
ARGMAX=.5D0*DLOG(INTEN0/ITHRESH)
RMAX=W0*DSQRT(ARGMAX)

WRITE(*,*) ' '
WRITE(*,*) ' '
WRITE(*,*) 'STARTING NEXT CHARGE STATE:', CHSTATE
WRITE(*,*) ' '
WRITE(*,*) 'Threshold intensity =', ITHRESH
WRITE(*,280) ZMAX/Z0, RMAX/W0, NUMTEST
280  FORMAT(/ ' Threshold focal volume to', F5.2, ' times the ',
+   ' confocal parameter', '/', ' and to', F5.2, ' times the ',
+   ' 1/e^2 point at the beam waist.', '/', ' Calculating for', I6,
+   ' electrons.'//)

***** THE MAIN LOOP WHERE NUMTEST ELECTRONS ARE PLACED AT RANDOM POSITIONS WITHIN THE

```

```

***** LASER FOCUS, IONIZED, AND PROPAGATED FROM THE FOCUS.
      DO 70 N=1, NUMTEST

***** P DETERMINES THE PLACEMENT OF THE ELECTRON IN Z. SINCE THE RMAX CHANGES AS A
***** FUNCTION OF Z, A WEIGHT IS APPLIED TO GIVE A HIGHER PROBABILITY OF PLACEMENT
***** WHERE RMAX IS LARGER.
      CALL RANDOM(P)
      INDMIN=1
      INDMAX=1025
      INDCURR=513
291  CONTINUE
      IF (PZ(INDCURR).EQ.P) THEN
          ZINIT=ZMAX*(INDCURR-513.)/512.
          GOTO 292
      ENDIF
      IF ((INDMAX-INDMIN).LE.1) THEN
          ZINIT=ZMAX*((INDMAX+INDMIN)/2.-513.)/512.
          GOTO 292
      ENDIF
      IF (PZ(INDCURR).LT.P) THEN
          INDMIN=INDCURR
      ELSE
          INDMAX=INDCURR
      ENDIF
      INDCURR=(INDMAX-INDMIN)/2+INDMIN
      GOTO 291
292  CONTINUE

***** THESE LINES PLACE THE ELECTRON AT A RANDOM RADIUS WITH A QUADRATIC WEIGHT.
      WZ=W0*DSQRT(1.0D0+(ZINIT/Z0)**2)
      ARGMAX=.5D0*DLOG(INTENO/ITHRESH*(W0/WZ)**2)
      RMAX=WZ*DSQRT(ARGMAX)

      CALL RANDOM(P)
      RINIT=RMAX*SQRT(P)

      CALL RANDOM(P)
      THETAINIT=2.*PI*P

***** THE INITIAL POSITIONS (X=Y(1), Y=Y(3), Z=Y(5)) AND VELOCITIES (VX=Y(2), VY=Y(4), VZ=Y(6))
      Y(1)=RINIT*COS(THETAINIT)
      Y(2)=0.0D0
      Y(3)=RINIT*SIN(THETAINIT)
      Y(4)=0.0D0
      Y(5)=ZINIT
      Y(6)=0.0D0

***** R2 = RADIUS FROM BEAM AXIS
      R2=(Y(1)**2+Y(3)**2)

***** WZ = 1/e^2 POINT OF INTENSITY IN RADIAL DIRECTION AT Y(5)
      WZ=W0*DSQRT(1.0D0+(Y(5)/Z0)**2)

***** IRZ = INVERSE OF RADIUS OF CURVATURE OF LASER BEAM AT Y(5) i.e. AT Z
      IRZ=Y(5)/(Y(5)**2+Z0**2)

***** TINDINT = PART OF INTENSITY EQN WHICH IS INDEPENDENT OF TIME
      TINDINT=INTENO*(W0/WZ)**2*DEXP(-2.0D0*(R2/WZ**2))

***** TINDPHASE = TIME INDEPENDENT PORTION OF PHASE( ARGUMENT IN COSINE)
      TINDPHASE=K*Y(5)-DATAN(Y(5)/Z0)+K*R2*IRZ/2.0D0

***** IPEAK = THE PEAK INTENSITY THAT THE ATOM WILL EXPERIENCE AT A Z POSITION OF Y(5)
      IPEAK=TINDINT

      IF (LINPOL) THEN
C      THESE STATEMENTS ARE FOR RELEASE AT I=ITHRESH AND PEAK OF COS() OF PULSE FOR LINEAR
C      POLARIZATION:
          PHIFREE=PI*DINT(SIGN(OMEGA*SIGMAT/2.0D0*DSQRT(DLOG
+          (IPEAK/ITHRESH)/DLOG(2.0D0))/PI-1, Y(5)))
          ELSE
C      THESE STATEMENTS ARE FOR RELEASE AT I=ITHRESH OF PULSE FOR CIRCULAR POLARIZATION:
          PHIFREE=DSIGN(OMEGA*SIGMAT/2.0D0*DSQRT(DLOG(IPEAK/
+          ITHRESH)/DLOG(2.0D0)), Y(5))
          ENDIF

***** T = THE TIME IN UNITS OF PHASE WHEN THE ATOM IS IONIZED

```

```

T=TINDPHASE-PHIFREE
PHASE=PHIFREE
INTENSITY=TINDINT*DEXP(-DLOG(2.0D0)*
+ ((PHASE/(OMEGA*SIGMAT/2.0D0))**2))

***** TEND IS THE TIME AT WHICH THE DIFF
***** EQUATION IS TO BE SOLVED GIVEN THE SOLUTION AT T.
TEND=T+INCREM

***** EPINIT IS THE PONDERMOTIVE POTENTIAL AT THE INTENSITY WHERE THE ELECTRON
***** IS IONIZED. IT IS USED FOR CHECKING TO SEE IF LASER PULSE INTENSITY
***** HAS SUFFICIENTLY DIMINISHED TO STOP AND ALSO FOR ERROR CHECKING.
EPINIT=1.0345D-16*INTENSITY
C WRITE(*,*)INTENSITY,EPINIT

***** VMAX AND RMAX ARE USED BY THE DIFF EQN SOLVER FOR MAINTAINING SOLUTION WITHIN
TOLERANCES (TOL):
VMAX=DSQRT(2.0D0*EPINIT/M0)/K
RQMAX=VMAX

C WRITE(*,*)'BEFORE'
***** THIS IS THE BEGINNING OF THE LOOP TO CALCULATE ELECTRON TRAJECTORY
***** BASED ON LORENTZ FORCE.
810 CONTINUE

***** ODEINTD IS A NUM. RECIPES ROUTINE TO CALCULATE THE SOLUTION TO A DIFF EQN
***** DERIVS IS THE SUBROUTINE WHICH CONTAINS THE LORENTZ FORCE EQN
C CALL DIVPRK (IDO,NEQ,SUBONE,T,TEND,TOL,PARAM,Y)
CALL ODEINTD(Y,6,T,TEND,TOL,H,HMIN,nok,nbad,DERIVS,
+ RKQS,RQMAX,VMAX)

VX=OMEGA*Y(2)
VY=OMEGA*Y(4)
VZ=OMEGA*Y(6)

***** ENERGY = ENERGY OF THE ELECTRON AT THE CURRENT TIME
VSQR=(VX**2+VY**2+VZ**2)/C**2
ENERGY=(1.0D0/DSQRT(1.0D0-VSQR))-1.0D0)*511.D0

***** R2 = DISTANCE OF ELECTRON FROM BEAM AXIS SQUARED
R2=Y(1)**2+Y(3)**2

***** IRZ = INVERSE OF RADIUS OF CURVATURE OF LASER BEAM
IRZ=Y(5)/(Y(5)**2+Z0**2)

***** WZ = 1/e^2 RADIUS OF LASER AT Y(5)
WZ=W0*SQRT(1.0D0+(Y(5)/Z0)**2)

***** INTENSITY = TIME DEPENDENT INTENSITY NOT INCLUDING OSCILLATORY TERM.
INTENSITY=INTENO*(W0/WZ)**2*DEXP(-2.0D0*(R2/WZ**2)-
+ DLOG(2.0D0)*((Y(5)*K-T-DATAN(Y(5)/Z0)+
+ R2*IRZ*K/2.0D0)/(OMEGA*SIGMAT/2.0D0))**2)

***** EPOND = PONDERMOTIVE POTENTIAL OF LASER AT CURRENT ELECTRON POSITION
EPOND=1.0345D-16*INTENSITY

C WRITE(*,*)EPINIT,EPOND,ENERGY

***** IF PONDERMOTIVE POTENTIAL OF LASER AT CURRENT ELECTRON POSITION IS
***** MUCH LESS THAN PONDERMOTIVE POTENTIAL AT IONIZATION INTENSITY THEN
***** ANY FURTHER CALCULATION OF ELECTRON TRAJECTORY WILL HAVE MINIMAL
***** CONSEQUENCES AND WE CAN STORE TRAJECTORIES AND EXIT CALCULATION.
***** !!!!!THIS COMPARISON BASED ON NON-RELATIVISTIC CALC
***** (i.e. EPOND=.5MV**2)!!!!!!
IF (EPOND.LT.(TOL**2*EPINIT)) THEN

VOUT(1,N)=VX
VOUT(2,N)=VY
VOUT(3,N)=VZ
POSOUT(1,N)=Y(1)
POSOUT(2,N)=Y(3)
POSOUT(3,N)=Y(5)

***** IF THE INTENSITY IS STILL OF SUFFICIENT MAGNITUDE, THEN CONTINUE
***** CALCULATING ITS TRAJECTORY.
ELSE
T=TEND
TEND=TEND+INCREM

```



```

        GOTO 810
    ENDIF

***** THESE LINES OUTPUT INFO TO THE LOG FILE TO KEEP UPDATED
    IF ((1.*N).EQ.(10.*INT(N/10.))) THEN
        WRITE(*,66)N
66      FORMAT(I4,I\X)
    ENDIF

70    CONTINUE

***** OUTPUT INFO FOR PREVIOUS CHARGE STATE TO OUTPUT FILE ****
    DO 77 I=1,NUMTEST
        WRITE(65,76)CHSTATE,(POSOUT(J,I),J=1,3),(VOUT(J,I),J=1,3),
+ (1.0D0/DSQRT(1.0D0-(VOUT(1,I)**2+VOUT(2,I)**2+VOUT(3,I)**2)/C**2)
+ -1.0D0)*511.D0
76      FORMAT(I2,6(2X,E10.3),F8.2)
77    CONTINUE

***** DONE WITH THIS CHARGE STATE SO CONTINUE ON TO THE NEXT HIGHER ONE
    CHSTATE=CHSTATE+1

***** START ALL OVER AGAIN WITH NEW CHARGE STATE AND THUS HIGHER ITHRESH
    GOTO 50

950   CONTINUE

998   CONTINUE

    END

*****
*****                               END OF MAIN PROGRAM                               *****
*****

    SUBROUTINE DERIVS(T,Y,YPRIME)

***** THIS SUBROUTINE IS THE RELATIVISTIC EQUATION OF MOTION OF AN ELECTRON
***** IN A LASER FIELD. IT IS USED BY ODEINTD TO CALCULATE ELECTRON TRAJ.

    INTEGER NEQ
    PARAMETER(NEQ=6)
    LOGICAL LINPOL,ERRFLAG
    REAL*8 C,M0,T,Y(NEQ),YPRIME(NEQ),GAMMA,ZCOEF1,ZCOEF2
    REAL*8 PI,E0,EPS0,K,OMEGA,W0,Z0,WZ,PHASE,IRZ
    REAL*8 EX0,EX,EY,EZ,BX,BY,BZ,BETADOTE,PHASEC,PHASES
    REAL*8 BETAX,BETAY,BETAZ,R2,VSQR
    REAL*8 COEF1,SIGMAT,COEFF

    PARAMETER(C=2.99792458D8,M0=9.109534D-31,PI=3.141593D0)
    PARAMETER(E0=1.6021892D-19,EPS0=8.85418782D-12)

    COMMON /GLOB/ LINPOL,COEF1,W0,Z0,K,OMEGA,SIGMAT,GAMMA,ERRFLAG

    WZ=W0*DSQRT(1.0D0+(Y(5)/Z0)**2)
    IRZ=Y(5)/(Y(5)**2+Z0**2)
    BETAX=Y(2)*K
    BETAY=Y(4)*K
    BETAZ=Y(6)*K
    R2=Y(1)**2+Y(3)**2
    VSQR=BETAX**2+BETAY**2+BETAZ**2
    GAMMA=1.0D0
    IF (VSQR.LT.1.0D0) THEN
        GAMMA=1.0D0/DSQRT(1.0D0-VSQR)
    ELSE
C      WRITE(*,*)'GAMMA AT DUMMY SETTING'
        GAMMA=9.99999D37
        ERRFLAG=.TRUE.
    ENDIF
    COEFF=- (E0/(M0*OMEGA**2))/GAMMA
    PHASE=K*Y(5)-T-DATAN(Y(5)/Z0)+K*R2*IRZ/2.0D0
    PHASEC=DCOS(PHASE)
    PHASES=DSIN(PHASE)
    EX0=COEF1*(W0/WZ)*DEXP(-(R2/WZ**2)-DLOG(2.0D0)/2.0D0*
+ ((PHASE/(OMEGA*SIGMAT/2.0D0))**2))

```

```

ZCOEF1=IRZ*EX0
ZCOEF2=EX0*2.0D0/(K*WZ**2)

IF (LINPOL) THEN
  EX=EX0*PHASEC
  EY=0.0D0
  EZ=(ZCOEF2*PHASES-ZCOEF1*PHASEC)*Y(1)
  BX=0.0D0
  BY=EX
  BZ=(ZCOEF2*PHASES-ZCOEF1*PHASEC)*Y(3)
ELSE
  EX=EX0*PHASEC
  EY=-EX0*PHASES
  EZ=ZCOEF1*(-Y(1)*PHASEC+Y(3)*PHASES)+ZCOEF2*
+   (Y(1)*PHASES+Y(3)*PHASEC)
  BX=-EY
  BY=EX
  BZ=ZCOEF1*(-Y(1)*PHASES-Y(3)*PHASEC)+ZCOEF2*
+   (-Y(1)*PHASEC+Y(3)*PHASES)
ENDIF

BETADOTE=BETAX*EX+BETAY*EY+BETAZ*EZ

YPRIME(1)=Y(2)
YPRIME(2)=COEFF*(EX+BETAY*BZ-BETAZ*BY-BETAX*BETADOTE)
YPRIME(3)=Y(4)
YPRIME(4)=COEFF*(EY+BETAZ*BX-BETAX*BZ-BETAY*BETADOTE)
YPRIME(5)=Y(6)
YPRIME(6)=COEFF*(EZ+BETAX*BY-BETAY*BX-BETAZ*BETADOTE)

RETURN
END

*****
***** THE FOLLOWING SUBROUTINES MAKE UP A DIFFERENTIAL EQUATION SOLVER AND ARE *****
***** FROM: *****
***** WILLIAM H. PRESS, SAUL A. TEUKOLSKY, WILLIAM T. VETTERLING, AND BRIAN P. *****
***** FLANNERY, NUMERICAL RECIPES IN FORTRAN 2ND ED(CAMBRIDGE, NEW YORK, 1992). *****
*****

SUBROUTINE odeintd(ystart,nvar,x1,x2,eps,h1,hmin,nok,nbad,derivs,
*rkqs,RQMAX,VMAX)
  INTEGER nbad,nok,nvar,KMAXX,MAXSTP,NMAX
  REAL*8 eps,h1,hmin,x1,x2,TINY,VMAX,RQMAX
  EXTERNAL derivs,rkqs
  PARAMETER (MAXSTP=10000,NMAX=6,KMAXX=200,TINY=1.D-30)
  INTEGER i,kmax,kount,nstp
  REAL*8 dxsav,h,hdid,hnext,x,xsav,dydx(NMAX),ystart(NMAX),
+ xp(KMAXX),y(NMAX),yp(NMAX,KMAXX),yscal(NMAX),XPREV
  COMMON /path/ kmax,kount,dxsav,xp,yp

  KMAXX=0
  x=x1
  XPREV=X1
  h=dsign(h1,x2-x1)
  nok=0
  nbad=0
  kount=0
  do 11 i=1,nvar
    y(i)=ystart(i)
  11 continue
  if (kmax.gt.0) xsav=x-2.D0*dxsav
  do 16 nstp=1,MAXSTP
    call derivs(x,y,dydx)
    do 12 i=1,nvar/2
      YSCAL(I)=DABS(Y(I))+DABS(H*DYDX(I))+TINY
      yscal(2*i)=VMAX
      yscal(2*i-1)=RQMAX
    12 continue
    if (kmax.gt.0) then
      if (DABS(x-xsav).gt.DABS(dxsav)) then
        if (kount.lt.kmax-1) then
          kount=kount+1
          xp(kount)=x
          do 13 i=1,nvar
            yp(i,kount)=y(i)
          13 continue
          xsav=x

```

```

        endif
    endif
endif
if((x+h-x2)*(x+h-x1).gt.0.D0) h=x2-x
call rkqs(y,dydx,nvar,x,h,eps,yscal,hdid,hnext,derivs)
if(hdid.eq.h)then
    nok=nok+1
else
    nbad=nbad+1
C    WRITE(*,*)'NBAD =',NBAD
endif
if((x-x2)*(x2-x1).ge.0.D0)then
    do 14 i=1,nvar
        ystart(i)=y(i)
14    continue
        if(kmax.ne.0)then
            kount=kount+1
            xp(kount)=x
            do 15 i=1,nvar
                yp(i,kount)=y(i)
15            continue
            endif
            return
        endif
        if(dABS(hnext).lt.hmin) pause
        **stepsize smaller than minimum in odeint'
        h=hnext
16    continue
        pause 'too many steps in odeint'
        return
    END
C (C) Copr. 1986-92 Numerical Recipes Software #(ks10R2-11j.
C*****

SUBROUTINE rkqs(y,dydx,n,x,htry,eps,yscal,hdid,hnext,derivs)
INTEGER n,NMAX
DOUBLE PRECISION eps,hdid,hnext,htry,x,dydx(n),y(n),yscal(n)
EXTERNAL derivs
PARAMETER (NMAX=6)
CU    USES derivs,rkck
INTEGER i
LOGICAL LINPOL,ERRFLAG
DOUBLE PRECISION errmax,h,xnew,yerr(NMAX),ytemp(NMAX),SAFETY,PGROW
*,PSHRNK,ERRCON
PARAMETER (SAFETY=0.9d0,PGROW=-.2d0,PSHRNK=-.25d0,ERRCON=1.89d-4)
REAL*8 COEF1,W0,Z0,K,OMEGA,SIGMAT,GAMMA
COMMON /GLOB/ LINPOL,COEF1,W0,Z0,K,OMEGA,SIGMAT,GAMMA,ERRFLAG
h=htry
1    ERRFLAG=.FALSE.
    call rkck(y,dydx,n,x,h,ytemp,yerr,derivs)
    errmax=0.d0
    do 11 i=1,n
        errmax=max(errmax,DABS(GAMMA*yerr(i)/yscal(i)))
11    continue
    errmax=errmax/eps
    if(errmax.gt.1.d0)then
C        IF (ERRFLAG) THEN
            WRITE(*,*)'ESCAPED ERROR TRAP!!'
            H=.1*H
        ELSE
            h=SAFETY*h*(errmax**PSHRNK)
        ENDIF
        xnew=x+h
        if(xnew.eq.x)pause 'stepsize underflow in rkqs'
        goto 1
    else
        IF (ERRFLAG) THEN
            STOP 'EXITTED WITH GAMMA SET TO DUMMY SETTING!!!'
        ENDIF
        if(errmax.gt.ERRCON)then
            hnext=SAFETY*h*(errmax**PGROW)
        else
            hnext=5.d0*h
        endif
        hdid=h
        x=x+h

```

```

        do 12 i=1,n
            y(i)=ytemp(i)
12       continue
            return
        endif
    END
C (C) Copr. 1986-92 Numerical Recipes Software #(ks10R2-11j).
*****

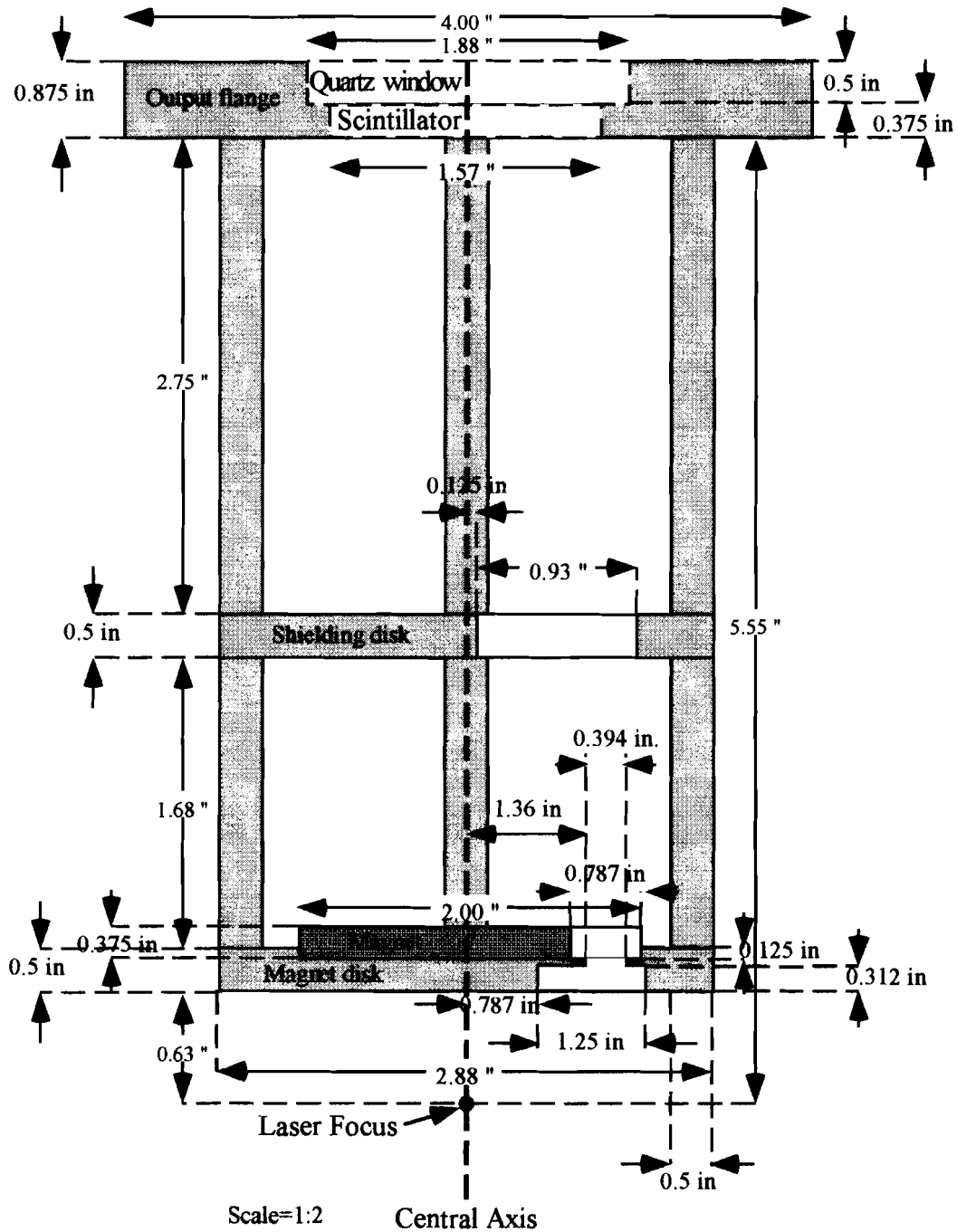
SUBROUTINE rkck(y,dydx,n,x,h,yout,yerr,derivs)
INTEGER n,NMAX
DOUBLE PRECISION h,x,dydx(n),y(n),yerr(n),yout(n)
EXTERNAL derivs
PARAMETER (NMAX=6)
CU     USES derivs
INTEGER i
DOUBLE PRECISION ak2(NMAX),ak3(NMAX),ak4(NMAX),ak5(NMAX),ak6(NMAX)
*
*ytemp(NMAX),A2,A3,A4,A5,A6,B21,B31,B32,B41,B42,B43,B51,B52,B53,
*B54,B61,B62,B63,B64,B65,C1,C3,C4,C6,DC1,DC3,DC4,DC5,DC6
PARAMETER (A2=.2d0,A3=.3d0,A4=.6d0,A5=1.d0,A6=.875d0,B21=.2d0,B31
*=3.d0/40.d0,
*B32=9.d0/40.d0,B41=.3d0,B42=-.9d0,B43=1.2d0,B51=-11.d0/54.d0,B52
*=2.5d0,
*B53=-70.d0/27.d0,B54=35.d0/27.d0,B61=1631.d0/55296.d0,B62=175.d0
*/512.d0,
*B63=575.d0/13824.d0,B64=44275.d0/110592.d0,B65=253.d0/4096.d0,C1
*=37.d0/378.d0,
*C3=250.d0/621.d0,C4=125.d0/594.d0,C6=512.d0/1771.d0,DC1=C1-2825.d0
*/27648.d0,
*DC3=C3-18575.d0/48384.d0,DC4=C4-13525.d0/55296.d0,DC5=-277.d0
*/14336.d0,
*DC6=C6-.25d0)

        do 11 i=1,n
            ytemp(i)=y(i)+B21*h*dydx(i)
11       continue
            call derivs(x+A2*h,ytemp,ak2)
            do 12 i=1,n
                ytemp(i)=y(i)+h*(B31*dydx(i)+B32*ak2(i))
12       continue
            call derivs(x+A3*h,ytemp,ak3)
            do 13 i=1,n
                ytemp(i)=y(i)+h*(B41*dydx(i)+B42*ak2(i)+B43*ak3(i))
13       continue
            call derivs(x+A4*h,ytemp,ak4)
            do 14 i=1,n
                ytemp(i)=y(i)+h*(B51*dydx(i)+B52*ak2(i)+B53*ak3(i)+B54*ak4(i))
14       continue
            call derivs(x+A5*h,ytemp,ak5)
            do 15 i=1,n
                ytemp(i)=y(i)+h*(B61*dydx(i)+B62*ak2(i)+B63*ak3(i)+B64*ak4(i)+
*B65*ak5(i))
15       continue
            call derivs(x+A6*h,ytemp,ak6)
            do 16 i=1,n
                yout(i)=y(i)+h*(C1*dydx(i)+C3*ak3(i)+C4*ak4(i)+C6*ak6(i))
16       continue
            do 17 i=1,n
                yerr(i)=h*(DC1*dydx(i)+DC3*ak3(i)+DC4*ak4(i)+DC5*ak5(i)+DC6*
*ak6(i))
17       continue
            return
        END
C (C) Copr. 1986-92 Numerical Recipes Software #(ks10R2-11j).

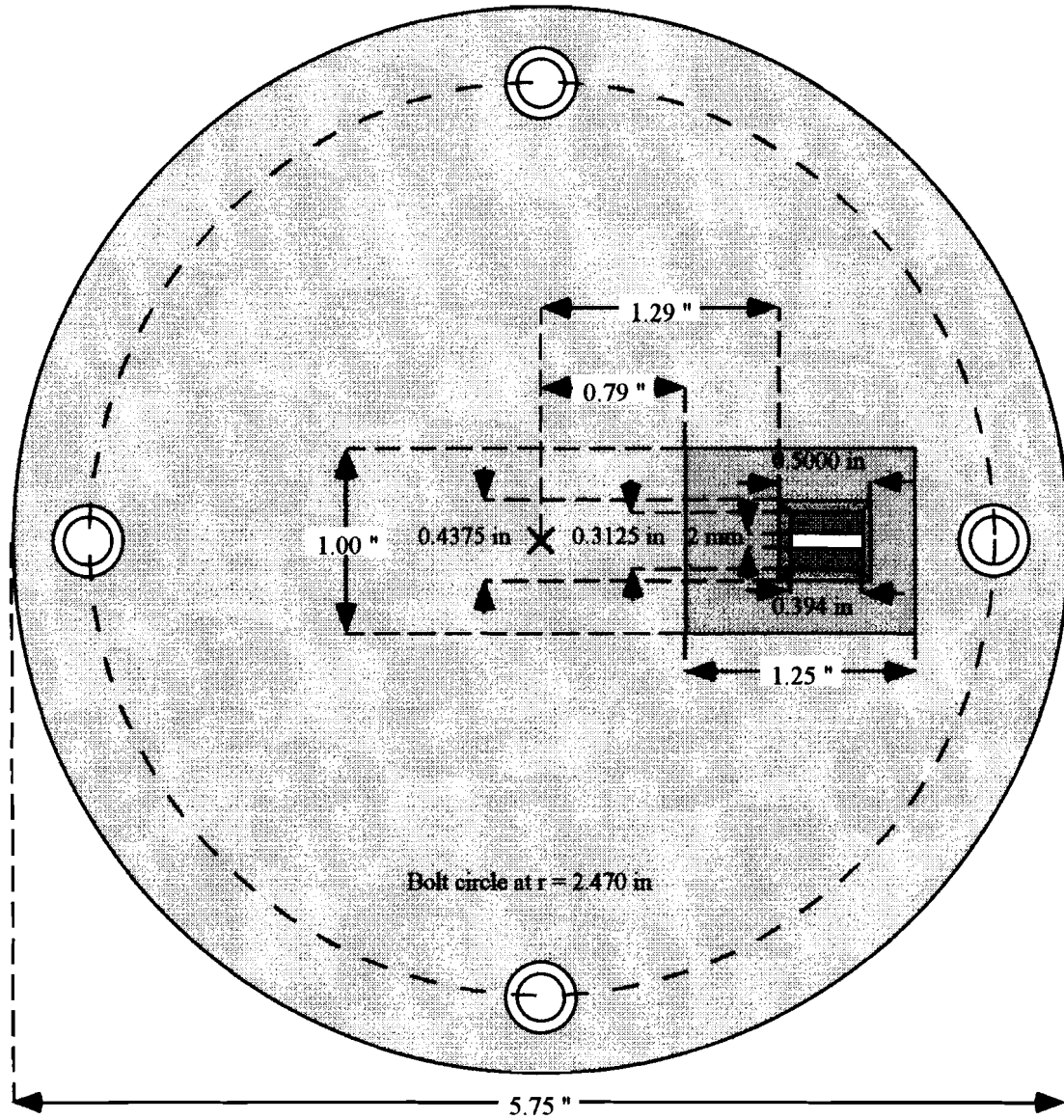
```

Appendix B
Schematics of the magnetic electron spectrometer

All materials are aluminum except the iron core of the magnet, screws which are non-magnetic stainless steel or brass, the quartz output window, and the plastic scintillator.

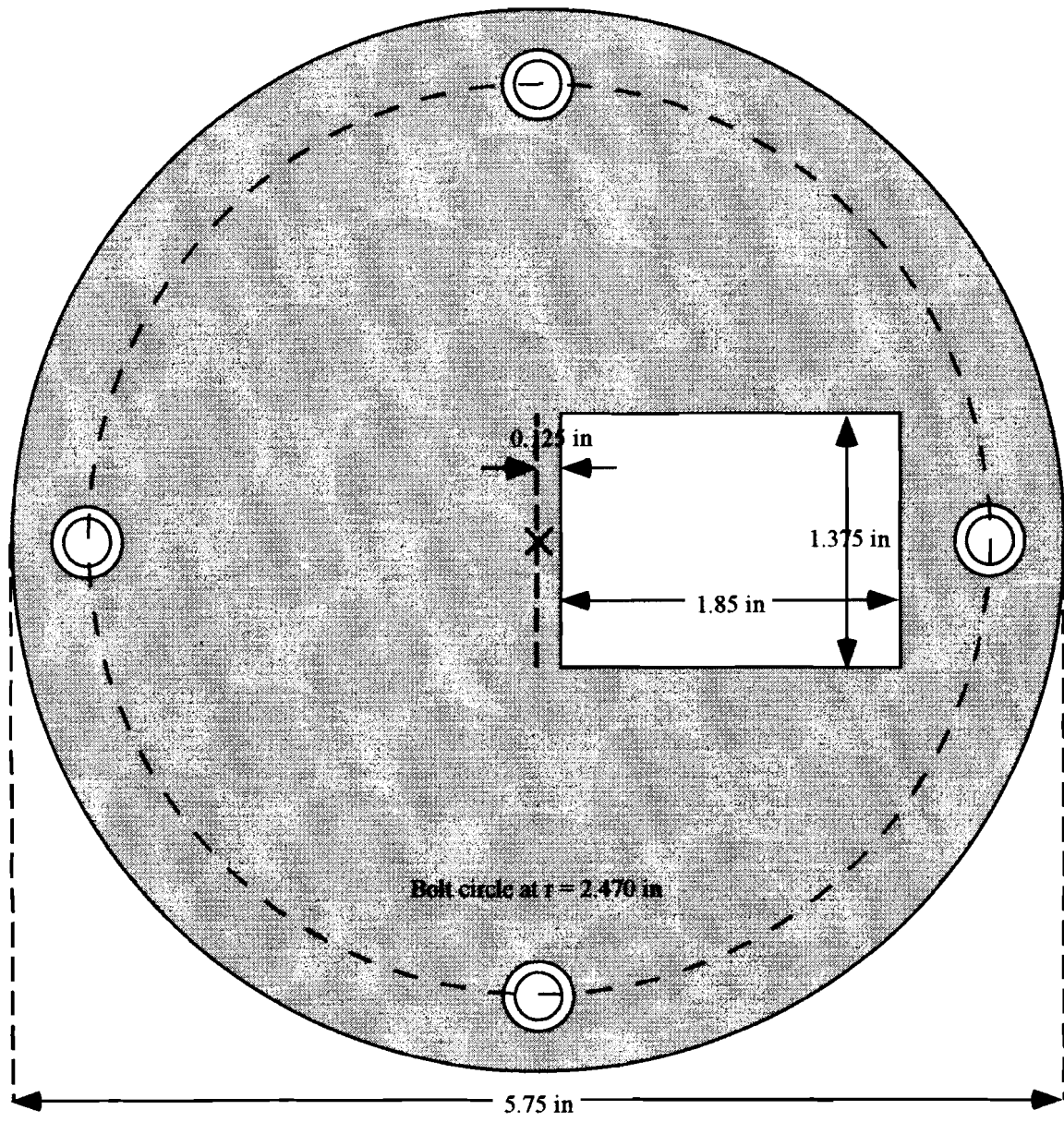


Bottom View of Magnet Disk:



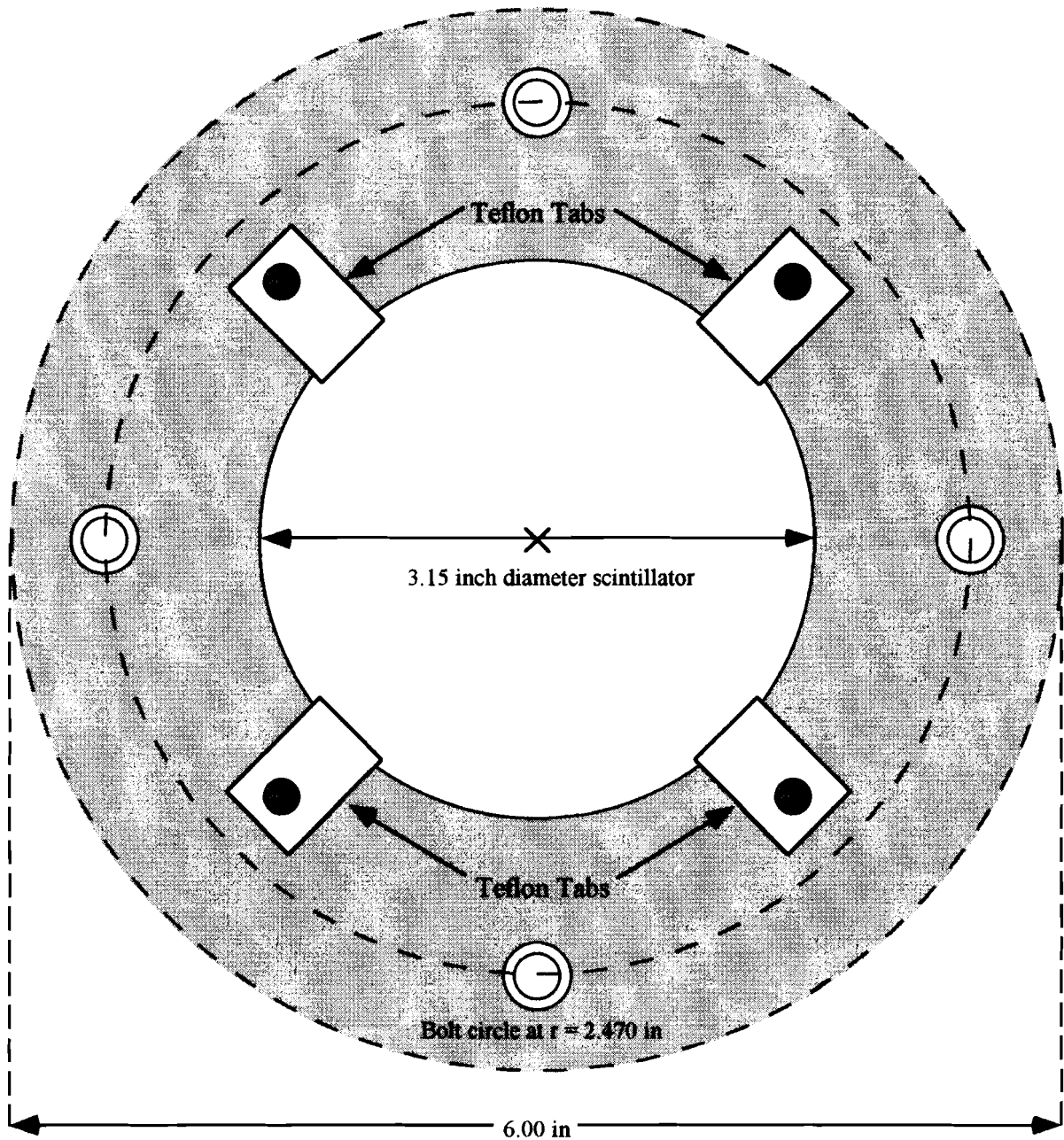
Scale=1:1

Shielding Disk:



Scale=1:1

Bottom View of Output Flange:



(View cut off by 6 inch port; Actual flange diameter is 8 inches)

Scale=1:1

Appendix C

Computer code for propagation of electrons through the spectrometer

The source code to propagate the electrons through the spectrometer is presented here. The program was written for Microsoft FORTRAN Powerstation, version 1.0 for MS-DOS and Windows operating systems. To maximize portability, FORTRAN 77 with DEC VAX FORTRAN extensions have been adhered to whenever possible. Only file access statements need alteration for compilation with DEC VAX extensions.

```

$DECLARE
PROGRAM ENERGY_DISTRIBUTION

*****
***** THIS PROGRAM USES THE EJECTED ELECTRON TRAJECTORIES FOUND IN THE MONTE CARLO *****
***** SIMULATION PROGRAM GIVEN IN APPENDIX A AND PROPAGATES THEM THROUGH THE *****
***** SPECTROMETER TO GIVE PREDICTIONS OF THE ELECTRON ENERGY DISTRIBUTIONS *****
***** AT A FIXED ANGLE. THE SAME PROGRAM IS USED TO CALCULATE PREDICTED ANGULAR *****
***** DISTRIBUTIONS AT A FIXED ENERGY BY SIMPLY CHANGING A FEW LINES TO SCAN *****
***** THROUGH ANGLE INSTEAD OF ENERGY. *****
*****

CHARACTER*12 FNAME
CHARACTER*16 HEAD2
CHARACTER*60 HEADER
INTEGER IOCHECK, NUMTEST, CHSTATE, CHDUM, MAXCHAR
INTEGER I, J, K, NOK, NBAD
REAL PI, POSIT(10, 3, 10000), VEL(10, 3, 10000), PNORM(10), C
PARAMETER (PI=3.14159265359E0, C=2.99792458E8)
REAL ANGLE, ANGSPC, MAXXSCINT, MAXZSCINT, SCINTPOS, MINYMASK, MAXYMASK
REAL MINYMAG, MAXYMAG, MIDMAG, MAXX1, MINXMASK, MAXXMASK, MAXZ
REAL MINXSHIELD, MAXXSHIELD, MINYSHIELD, MAXYSHIELD, MAXX2, BMAX
REAL Y(6), VTOT, T, TSTEP, ENUM, GAMMA, VMAX, RMAX, TEND, H
REAL HMIN, TOL, ENERGY, XP, YP, ZP, VX, VY, VZ, MINXMAG, MINPROP, VXY
REAL MINTPROP, ZATMAG, ENOBS, ENMAX

EXTERNAL DERIVS, RKQS

COMMON /GLOB/ GAMMA, BMAX

***** OPEN THE FILE CONTAINING THE ELECTRON TRAJECTORIES CALCULATED BY MONTE CARLO *****
***** SIMULATION PROGRAM OF APPENDIX A: *****
10 CONTINUE

WRITE(*,*) 'INPUT FILENAME CONTAINING ELECTRON TRAJECTORIES:'
READ(*, '(A)') FNAME

OPEN(64, FILE='D:\FORTRAN\OUTFILES\'//FNAME, IOSTAT=IOCHECK,
+ ERR=15, STATUS='OLD')

GOTO 20

15 CONTINUE
WRITE(*,*) 'THERE WAS AN ERROR OPENING ', FNAME
WRITE(*,*) 'MAKE SURE DATAFILE EXISTS AND IS IN DAT DIR'
WRITE(*,*) ' '
GOTO 10

20 CONTINUE

***** OPEN FILE TO SAVE ENERGY DISTRIBUTIONS: *****
WRITE(*,*) 'INPUT FILENAME FOR OUTPUT:'
READ(*, '(A)') FNAME
OPEN(65, FILE='D:\FORTRAN\OUTFILES\'//FNAME, IOSTAT=IOCHECK,
+ ERR=25, STATUS='NEW')

```

```

GOTO 30

25  CONTINUE
    WRITE(*,*) 'THERE WAS AN ERROR OPENING ', FNAME
    WRITE(*,*) 'THAT FILENAME PROBABLY ALREADY EXISTS'
    WRITE(*,*) ' '
    GOTO 20

30  CONTINUE

***** COPY THE HEADER INFORMATION CONTAINING EXPERIMENTAL CONDITIONS FROM THE ELECTRON
***** TRAJECTORY FILE TO THE FILE FOR OUTPUT IN THIS PROGRAM.
DO 40 I=1,9
    READ(64, '(A60)') HEADER
    WRITE(65, *) HEADER
40  CONTINUE

    READ(64, '(A16\')') HEAD2
    READ(64, *) NUMTEST
    CHSTATE=0
    ENMAX=0.0

***** THIS LOOP READS IN THE INITIAL TRAJECTORIES.
45  CONTINUE

    CHSTATE=CHSTATE+1
    READ(64, *, END=60) PNORM(CHSTATE)
    DO 50 I=1, NUMTEST
        READ(64, *) CHDUM, (POSIT(CHSTATE, J, I), J=1, 3),
+         (VEL(CHSTATE, J, I), J=1, 3), ENERGY
        IF (ENERGY.GT.ENMAX) THEN
            ENMAX=ENERGY
        ENDIF
50  CONTINUE

    GOTO 45

60  CONTINUE
    CLOSE(64)

    MAXCHAR=CHSTATE-1
    WRITE(*, *) MAXCHAR

***** INPUT ANGLE FROM BEAM AXIS WHERE ELECTRON DISTRIBUTION TO BE FOUND.
    WRITE(*, *) 'ENTER ANGLE TO OBSERVE'
    READ(*, *) ANGLE
    ANGLE=PI/180.*ANGLE

***** CONVERT THE ANGLE FROM BEAM AXIS TO THE ROTATION ANGLE OF THE SPECTROMETER.
    ANGSPEC=ACOS(COS(ANGLE)/COS(PI/4.))

***** THESE PARAMETERS DEFINE THE GEOMETRY OF THE SPECTROMETER AND ITS DISTANCE FROM
***** THE LASER FOCUS.
    MAXXSCINT=1.5E-2
    MAXZSCINT=3.7E-2
    SCINTPOS=28.19E-2
    MINYMASK=3.968E-2
    MAXYMASK=4.128E-2
    MINYMAG=MAXYMASK
    MAXYMAG=5.081E-2
    MIDMAG=4.604E-2
    MAXX1=15.0E-2
    MINXMASK=3.454E-2
    MAXXMASK=4.454E-2
    MAXZ=.11E-2
    MINXSHIELD=2.00E-2
    MAXXSHIELD=5.174E-2
    MINYSHIELD=3.175E-2
    MAXYSHIELD=3.968E-2
    MAXX2=6.668E-2
    MINXMAG=3.9544E-2

***** PARAMETERS USED FOR ACCURACY OF DIFFERENTIAL EQUATION SOLVER.
    TOL=2.5E-3
    HMIN=TOL/1.E10

***** ENOBS IS THE CENTRAL ENERGY OF OBSERVATION OF THE SPECTROMETER. THE ENERGY SCAN

```

```

***** BEGINS AT AN ENERGY OF 2 KEV.
        ENOBS=2.0

***** THIS LOOP IS THE MAIN LOOP WHICH SCANS IN ENERGY FROM 2 KEV TO 30% ABOVE THE MAXIMUM
***** ENERGY ELECTRON.
        175 CONTINUE

***** BMAX IS THE PEAK FIELD IN THE GAP OF THE MAGNET. THIS LINE CONVERTS ENERGY TO
***** CORRESPONDING MAGNETIC FIELD. THE CONVERSION WAS FOUND BY "CALIBRATING" THE CODE.
***** THE TRAJECTORIES OF ELECTRONS THROUGH THE SPECTROMETER WERE CALCULATED AND THE
***** ENERGIES OF THE ELECTRONS VERSUS THE REQUIRED MAGNETIC FIELD FOR PROPAGATION TO THE
***** SCINTILLATOR WAS FOUND.
        BMAX=1E-4*SQRT(ENOBS*(ENOBS/511.+1)/3.36E-4)

***** THIS LOOP SCANS THROUGH THE CHARGE STATES
        DO 200 J=1,MAXCHAR

***** THIS LOOP SCANS THROUGH ALL ELECTRONS IN ONE CHARGE STATE
        DO 100 K=1,NUMTEST
            VTOT=SQRT(VEL(J,1,K)**2+VEL(J,2,K)**2+VEL(J,3,K)**2)
            GAMMA=SQRT(1./(1.-(VTOT/C)**2))
            ENERGY=511.*(GAMMA-1.)

***** TO INCREASE THE SPEED OF THE CODE, IF AN ELECTRON'S ENERGY IS >50% OUTSIDE THE
***** OBSERVATION ENERGY OF THE SPECTROMETER, IT IS SKIPPED.
            IF (ABS(ENERGY-ENOBS).GT.(.5*ENOBS)) GOTO 888

***** THESE TWO IF-THEN-ELSES INCREASE THE STATISTICAL ACCURACY OF THE CODE.
***** ELECTRONS WHICH ARE NOT EJECTED IN THE FIRST QUADRANT, [+X,+Y] (WHERE THE
***** GAP IN THE SPECTROMETER WILL BE PLACED), WILL NEVER ENTER THE GAP. TO INCREASE THE
***** NUMBER OF ELECTRONS DETECTED TO BETTER THE STATISTICS, THE II-IV QUADRANTS ARE
***** MAPPED INTO THE FIRST QUADRANT. THIS REQUIRES THE NUMBER OF ELECTRONS DETECTED
***** LATER BE DIVIDED BY 4 SINCE 4 TIMES AS MANY ELECTRONS WILL BE COLLECTED AS SHOULD
***** BE. THESE IF-THEN-ELSES ARE ONLY VALID FOR CIRCULAR POLARIZATION SINCE LINEAR
***** POLARIZATION WILL BREAK THE SYMMETRY REQUIRED TO DO THIS.
            IF (POSIT(J,1,K).LT.0.0) THEN
                XP=-POSIT(J,1,K)
                VX=-VEL(J,1,K)
            ELSE
                XP=POSIT(J,1,K)
                VX=VEL(J,1,K)
            ENDIF

            IF (POSIT(J,2,K).LT.0.0) THEN
                YP=-POSIT(J,2,K)
                VY=-VEL(J,2,K)
            ELSE
                YP=POSIT(J,2,K)
                VY=VEL(J,2,K)
            ENDIF

            ZP=POSIT(J,3,K)
            VZ=VEL(J,3,K)

***** THESE LINES CONVERT THE ELECTRON TRAJECTORIES TO THE REFERENCE FRAME OF THE
***** SPECTROMETER. THE ROTATION OF THE SPECTROMETER CAN BE INVERSELY VIEWED AS A
***** ROTATION OF THE REST OF THE UNIVERSE RELATIVE TO THE SPECTROMETER. THESE LINES
***** PRODUCE THIS ROTATION AT AN ANGLE OF ANGSPEC WHICH WAS THE PREVIOUSLY CALCULATED
***** ANGLE OF ROTATION OF THE SPECTROMETER BASED ON THE USERS INPUT ANGLE FROM K.
            Y(1)=SIN(ANGSPEC)*XP+COS(ANGSPEC)*ZP
            Y(3)=YP
            Y(5)=-COS(ANGSPEC)*XP+SIN(ANGSPEC)*ZP
            Y(2)=SIN(ANGSPEC)*VX+COS(ANGSPEC)*VZ
            Y(4)=VY
            Y(6)=-COS(ANGSPEC)*VX+SIN(ANGSPEC)*VZ

***** AN ANALYSIS OF THE REQUIRED PROPAGATION DIRECTION OF THE ELECTRONS SHOWED THAT IF
***** THE ELECTRONS DID NOT TRAVEL AT 45°+/-5° FROM THE X AXIS, THERE WAS NO CHANCE OF *****
***** DETECTION. THE CURRENT ELECTRON IS THEREFORE SKIPPED IF ITS EJECTION ANGLE DOES NOT ***** LIE
***** WITHIN THIS RANGE.
            IF (ABS(ATAN(Y(4)/Y(2))-7854).GT.8.7266E-2) GOTO 888

***** MINPROP IS THE DISTANCE FROM THE FOCUS TO THE GAP. VXY IS THE ELECTRONS VELOCITY
***** IN THE X-Y PLANE. MINTPROP IS THE MINIMUM TIME IT TAKES THE ELECTRON TO PROPAGATE
***** TO THE GAP. NO Z COMPONENTS OF MAGNETIC FIELD ARE CONSIDERED IN THIS PROGRAM SO
***** WE CAN PROPAGATE THE ELECTRON FREELY IN THE Z DIRECTION (ZATMAG IS Z POSITION AT THE
***** MAGNET) AND DETERMINE IF IT STRIKES THE SPECTROMETER WITHOUT PROPAGATING THROUGH.
            MINPROP=SQRT(MINYMAG**2+MINXMAG**2)

```

```

VXY=SQRT(Y(2)**2+Y(4)**2)
MINTPROP=MINPROP/VXY
ZATMAG=Y(6)*MINTPROP+Y(5)
IF (SIGN(ZATMAG,Y(6)).GT.(1.1*MAXZ)) GOTO 888

***** TSTEP IS THE TIME STEP SIZE USED BY THE DIFFERENTIAL EQUATION SOLVER IN CALCULATED
***** THE ELECTRON TRAJECTORY. THE SMALLEST STRUCTURE OF THE MAGNET IS THE MASK BLOCKING
***** THE OUTSIDE PORTIONS OF THE C-MAGNET. THE TIME STEP MUST THEREFORE BE NO GREATER
***** THAN THE TIME IT TAKES THE ELECTRON TO PROPAGATE THROUGH THIS MASK OR THE CHECK
***** FOR SEEING IF THE ELECTRON STRUCK THE MASK WOULD BE IN ERROR.
TSTEP=(MAXYMASK-MINYMASK)/VTOT
H=TSTEP
T=0

***** RMAX AND VMAX ARE SCALE LENGTHS USED IN THE DIFFERENTIAL EQUATION SOLVER TO
***** DETERMINE THE ACCURACY OF THE SOLUTION REQUIRED.
VMAX=VTOT
RMAX=VMAX*TSTEP

***** THIS IS THE LOOP WHICH PROPAGATES THE ELECTRON FROM THE FOCUS USING THE
***** MAGNETIC FIELD DETERMINED FROM MEASUREMENTS WITH A HALL PROBE AND CURVE FITS
***** TO THE MEASURED FIELDS.
150 CONTINUE
TEND=T+TSTEP
CALL ODEINT(Y,6,T,TEND,TOL,H,HMIN,nok,nbad,DERIVS,
+ RKQS,RMAX,VMAX)
T=TEND

***** THESE IF-THENS CHECK TO SEE IF THE ELECTRON IS BLOCKED BY ANY PART OF THE
***** SPECTROMETER,GETS TURNED AROUND BY THE FIELD,OR MAKES IT THROUGH TO THE
***** SCINTILLATOR.
IF (Y(3).GE.SCINTPOS) GOTO 500
IF (Y(4).LT.0.0) GOTO 888
IF ((Y(3).LT.MINYSHIELD).AND.(ABS(Y(1)).GT.MAXX1).OR.
+ (Y(2).LT.0.0)) GOTO 888
IF ((Y(3).LT.MAXYSHIELD).AND.(Y(3).GE.MINYSHIELD)).AND.
+ (Y(1).LE.MINXSHIELD).OR.(Y(1).GE.MAXXSHIELD)) GOTO 888
IF ((Y(3).LT.MAXYMASK).AND.(Y(3).GE.MINYMASK)).AND.
+ ((Y(1).LE.MINXMASK).OR.(Y(1).GE.MAXXMASK)) GOTO 888
IF ((Y(3).LT.MAXYMAG).AND.(Y(3).GE.MINYMAG)).AND.
+ (ABS(Y(5)).GE.MAXZ)) THEN
GOTO 888
ENDIF
IF (Y(3).GE.MAXYMAG).AND.(ABS(Y(1)).GE.MAXX2)) GOTO 888
GOTO 150

***** IF THE CODE REACHES THIS POINT THEN THE ELECTRON HAS MADE IT THROUGH THE GAP TO
***** THE PLANE CONTAINING THE SCINTILLATOR. THE IF-THEN DETERMINES IF THE ELECTRON
***** STRIKES THE ACTIVE AREA OF THE SCINTILLATOR.
500 CONTINUE
IF ((ABS(Y(1)).LE.MAXXSCINT).AND.(ABS(Y(5)).LE.MAXZSCINT))
+ THEN
***** THIS ADDS A DETECTION TO THE NUMBER OF ELECTRONS DETECTED. PNORM(J)/4 IS
***** THE NORMALIZATION FACTOR TO THE PRESSURE AND THE SINGLE QUADRANT OF INTEREST.
***** ENERGY/ENOBS CORRECTS FOR ERROR INTRODUCED BECAUSE THE EXPERIMENTAL DATA DETERMINES
***** THE NUMBER OF ELECTRONS FROM THE NUMBER OF PHOTONS. IF THE ENERGY OF THE ELECTRON
***** IS LESS THAN THE ENERGY OF OBSERVATION THEN FEWER PHOTONS WILL BE CREATED WHICH
***** WILL APPEAR AS FEWER ELECTRONS.
ENUM=ENUM+PNORM(J)/4.*ENERGY/ENOBS
ENDIF

888 CONTINUE

100 CONTINUE
200 CONTINUE

***** OUTPUT TO DATA FILE AND LOG FILE
WRITE(65,*)ENOBS,ENUM
WRITE(*,*)'ENOBS=',ENOBS,'ENUM=',ENUM

***** INCREASE THE ENERGY BY 5%
ENOBS=ENOBS+.05*ENOBS
ENUM=0.0

***** CHECK TO SEE IF ENOBS IS >30% ABOVE MAXIMUM ENERGY ELECTRONS AND IF IS THEN
***** ALL DONE.
IF (ENOBS.LE.(ENMAX*1.3)) THEN
GOTO 175

```

```

      ENDIF
999  CONTINUE
      CLOSE(65)
      END

*****
*****
*****      END OF MAIN PROGRAM      *****
*****
*****

      SUBROUTINE DERIVS(T,Y,YPRIME)

***** THIS SUBROUTINE IS THE RELATIVISTIC EQUATION OF MOTION OF AN ELECTRON
***** IN A SPATIALLY VARYING, TIME INDEPENDENT MAGNETIC FIELD. IT IS USED BY ODEINTD
***** TO CALCULATE ELECTRON TRAJ.

      INTEGER NEQ
      PARAMETER(NEQ=6)
      REAL M0,Y(NEQ),YPRIME(NEQ),GAMMA
      REAL PI,EPS0,E0,C
      REAL BMAX,DUMMY,BZ
      REAL COEFF,BFIELD

      PARAMETER(C=2.99792458E8,M0=9.109534E-31,PI=3.141593E0)
      PARAMETER(E0=1.6021892E-19,EPS0=8.85418782E-12)

      COMMON /GLOB/ GAMMA,BMAX

      DUMMY=T
      COEFF=- (E0/M0)/GAMMA

***** THIS FUNCTIONAL CALL DETERMINES THE MAGNETIC FIELD AT THE ELECTRONS CURRENT
***** POSITION.
      BZ=BFIELD(Y(1),Y(3),BMAX)
      YPRIME(1)=Y(2)
      YPRIME(2)=COEFF*(Y(4)*BZ)
      YPRIME(3)=Y(4)
      YPRIME(4)=COEFF*(-Y(2)*BZ)
      YPRIME(5)=Y(6)
      YPRIME(6)=0.0

      RETURN
      END

*****
*****
      REAL FUNCTION BFIELD(X,Y,BMAX)

***** THIS FUNCTION DETERMINES THE FIELD AT THE ELECTRONS CURRENT POSITION. THE FIELD
***** IS GIVEN BY MEASUREMENTS WITH A HALL PROBE AND CURVE FITS TO THESE MEASUREMENTS.

      REAL X,Y,BMAX

      BFIELD=(.97/(1+(ABS(Y-4.604E-2)/.448E-2)**9.2)**(.266))*(1/(1.+
+ (ABS(X-3.9544E-2)/.9407E-2)**9.2)**(.266))+20./(650.*(1+
+ ((Y-4.604E-2)/3.3851E-2)**2))*BMAX

      RETURN
      END

*****
***** THE FOLLOWING SUBROUTINES MAKE UP A DIFFERENTIAL EQUATION SOLVER FROM: *****
***** WILLIAM H. PRESS, SAUL A. TEUKOLSKY, WILLIAM T. VETTERLING, AND BRIAN P. *****
***** FLANNERY, NUMERICAL RECIPES IN FORTRAN 2ND ED(CAMBRIDGE, NEW YORK, 1992). *****
*****

      SUBROUTINE odeint(ystart,nvar,x1,x2,eps,h1,hmin,nok,nbad,derivs,
+rkqs,RMAX,VMAX)
      INTEGER nbad,nok,nvar,KMAXX,MAXSTP,NMAX
      REAL eps,h1,hmin,x1,x2,ystart(nvar),TINY,RMAX,VMAX
      EXTERNAL derivs,rkqs
      PARAMETER (MAXSTP=10000,NMAX=50,KMAXX=200,TINY=1.e-30)
      INTEGER i,kmax,kount,nstp
      REAL dxsav,h,hdid,hnext,x,xsav,dydx(NMAX),xp(KMAXX),y(NMAX),

```

```

*yp(NMAX,KMAXX),yscal(NMAX)
COMMON /path/ kmax,kount,dxsav,yp,yp
x=x1
h=sign(h1,x2-x1)
nok=0
nbad=0
kount=0
do 11 i=1,nvar
  y(i)=ystart(i)
11 continue
if (kmax.gt.0) xsav=x-2.*dxsav
do 16 nstp=1,MAXSTP
  call derivs(x,y,dydx)
  do 12 i=1,nvar/2
    c   YSCAL(I)=DABS(Y(I))+DABS(H*DYDX(I))+TINY
      yscal(2*i)=VMAX
      yscal(2*i-1)=RMAX
12   continue
if (kmax.gt.0) then
  if (abs(x-xsav).gt.abs(dxsav)) then
    if (kount.lt.kmax-1) then
      kount=kount+1
      xp(kount)=x
      do 13 i=1,nvar
        yp(i,kount)=y(i)
13      continue
      xsav=x
    endif
  endif
endif
if ((x+h-x2)*(x+h-x1).gt.0.) h=x2-x
call rkqs(y,dydx,nvar,x,h,eps,yscal,hdid,hnext,derivs)
if (hdid.eq.h) then
  nok=nok+1
else
  nbad=nbad+1
endif
if ((x-x2)*(x2-x1).ge.0.) then
  do 14 i=1,nvar
    ystart(i)=y(i)
14   continue
if (kmax.ne.0) then
  kount=kount+1
  xp(kount)=x
  do 15 i=1,nvar
    yp(i,kount)=y(i)
15   continue
endif
return
endif
if (abs(hnext).lt.hmin) pause
*'stepsize smaller than minimum in odeint'
h=hnext
16 continue
pause 'too many steps in odeint'
return
END
C (C) Copr. 1986-92 Numerical Recipes Software #(ks10R2-11j.

```

```

SUBROUTINE rkqs(y,dydx,n,x,htry,eps,yscal,hdid,hnext,derivs)
INTEGER n,NMAX
REAL eps,hdid,hnext,htry,x,dydx(n),y(n),yscal(n)
EXTERNAL derivs
PARAMETER (NMAX=50)
CU  USES derivs,rkck
INTEGER i
REAL errmax,h,xnew,yerr(NMAX),ytemp(NMAX),SAFETY,PGROW,PSHRNK,
*ERRCON
PARAMETER (SAFETY=0.9,PGROW=-.2,PSHRNK=-.25,ERRCON=1.89e-4)
h=htry
1  call rkck(y,dydx,n,x,h,ytemp,yerr,derivs)
errmax=0.
do 11 i=1,n
  errmax=max(errmax,abs(yerr(i)/yscal(i)))
11 continue
errmax=errmax/eps
if (errmax.gt.1.) then

```

```

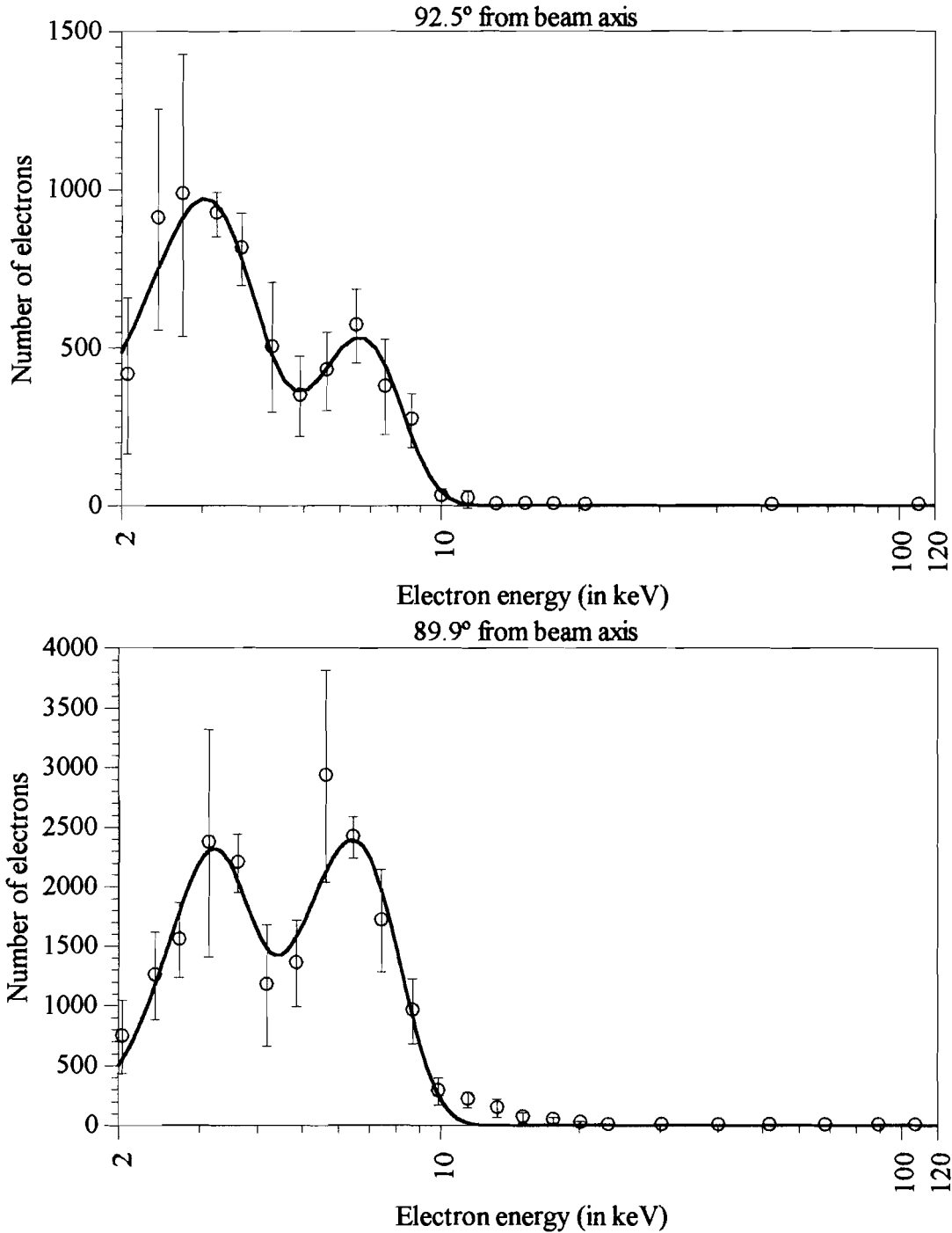
h=SAFETY*h*(errmax**PSHRNK)
if (h.lt.0.1*h) then
  h=.1*h
endif
xnew=x+h
if (xnew.eq.x) pause 'stepsize underflow in rkqs'
goto 1
else
  if (errmax.gt.ERRCON) then
    hnext=SAFETY*h*(errmax**PGROW)
  else
    hnext=5.*h
  endif
  hdid=h
  x=x+h
  do 12 i=1,n
    y(i)=ytemp(i)
12  continue
  return
endif
END
C (C) Copr. 1986-92 Numerical Recipes Software #(ks10R2-11j.

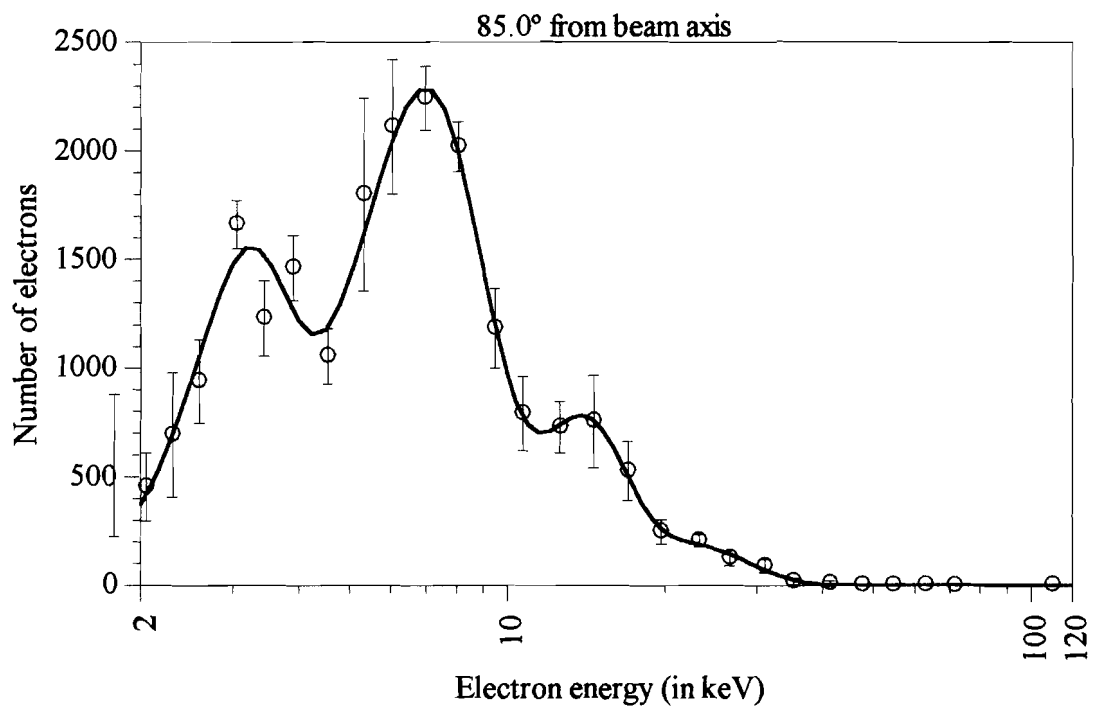
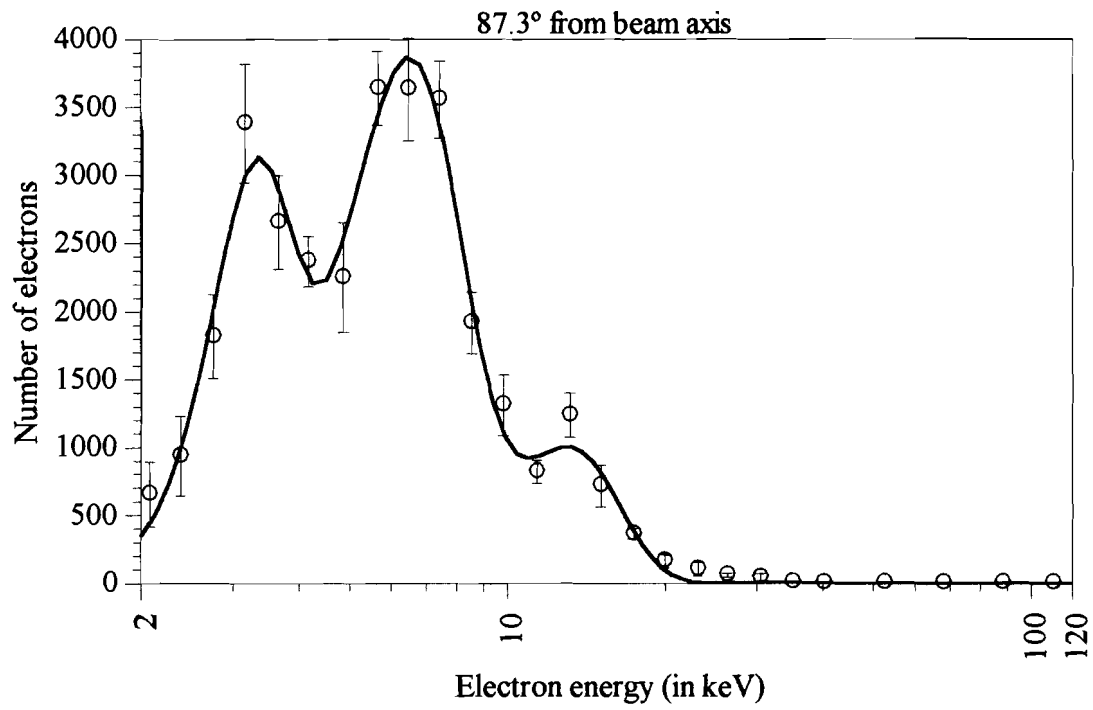
SUBROUTINE rkck(y,dydx,n,x,h,yout,yerr,derivs)
INTEGER n,NMAX
REAL h,x,dydx(n),y(n),yerr(n),yout(n)
EXTERNAL derivs
PARAMETER (NMAX=50)
CU USES derivs
INTEGER i
REAL ak2(NMAX),ak3(NMAX),ak4(NMAX),ak5(NMAX),ak6(NMAX),
*ytemp(NMAX),A2,A3,A4,A5,A6,B21,B31,B32,B41,B42,B43,B51,B52,B53,
*B54,B61,B62,B63,B64,B65,C1,C3,C4,C6,DC1,DC3,DC4,DC5,DC6
PARAMETER (A2=.2,A3=.3,A4=.6,A5=1.,A6=.875,B21=.2,B31=3./40.,
*B32=9./40.,B41=.3,B42=-.9,B43=1.2,B51=-11./54.,B52=2.5,
*B53=-70./27.,B54=35./27.,B61=1631./55296.,B62=175./512.,
*B63=575./13824.,B64=44275./110592.,B65=253./4096.,C1=37./378.,
*C3=250./621.,C4=125./594.,C6=512./1771.,DC1=C1-2825./27648.,
*DC3=C3-18575./48384.,DC4=C4-13525./55296.,DC5=-277./14336.,
*DC6=C6-.25)
do 11 i=1,n
  ytemp(i)=y(i)+B21*h*dydx(i)
11  continue
  call derivs(x+A2*h,ytemp,ak2)
  do 12 i=1,n
    ytemp(i)=y(i)+h*(B31*dydx(i)+B32*ak2(i))
12  continue
  call derivs(x+A3*h,ytemp,ak3)
  do 13 i=1,n
    ytemp(i)=y(i)+h*(B41*dydx(i)+B42*ak2(i)+B43*ak3(i))
13  continue
  call derivs(x+A4*h,ytemp,ak4)
  do 14 i=1,n
    ytemp(i)=y(i)+h*(B51*dydx(i)+B52*ak2(i)+B53*ak3(i)+B54*ak4(i))
14  continue
  call derivs(x+A5*h,ytemp,ak5)
  do 15 i=1,n
    ytemp(i)=y(i)+h*(B61*dydx(i)+B62*ak2(i)+B63*ak3(i)+B64*ak4(i)+
*B65*ak5(i))
15  continue
  call derivs(x+A6*h,ytemp,ak6)
  do 16 i=1,n
    yout(i)=y(i)+h*(C1*dydx(i)+C3*ak3(i)+C4*ak4(i)+C6*ak6(i))
16  continue
  do 17 i=1,n
    yerr(i)=h*(DC1*dydx(i)+DC3*ak3(i)+DC4*ak4(i)+DC5*ak5(i)+DC6*
*ak6(i))
17  continue
  return
END
C (C) Copr. 1986-92 Numerical Recipes Software #(ks10R2-11j.

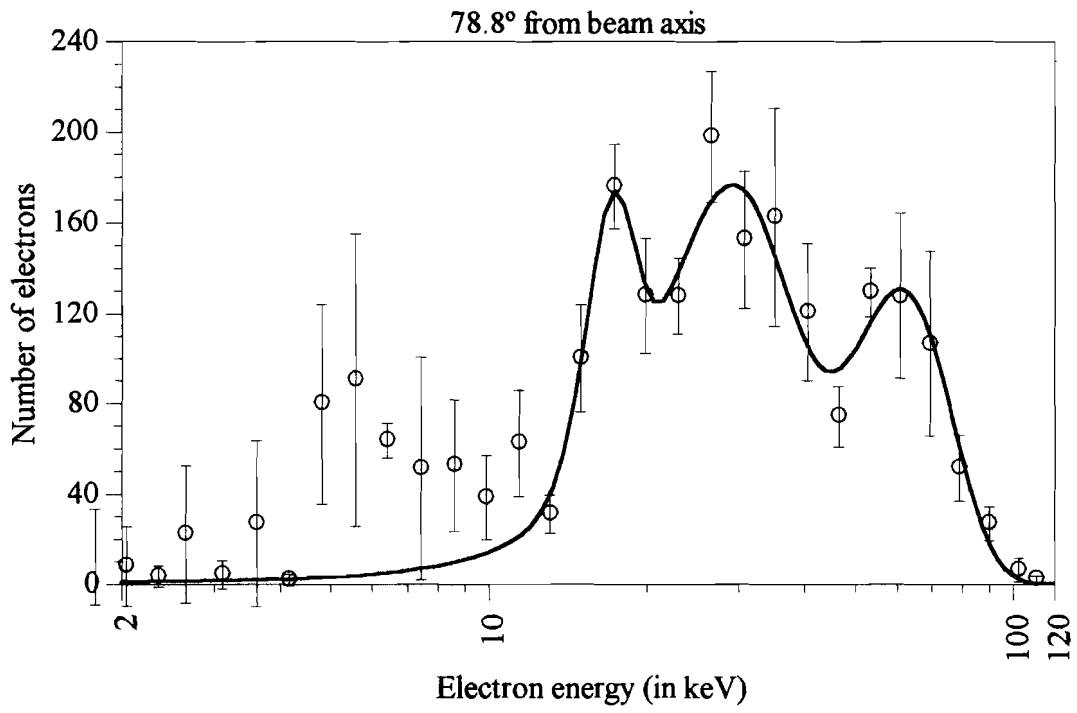
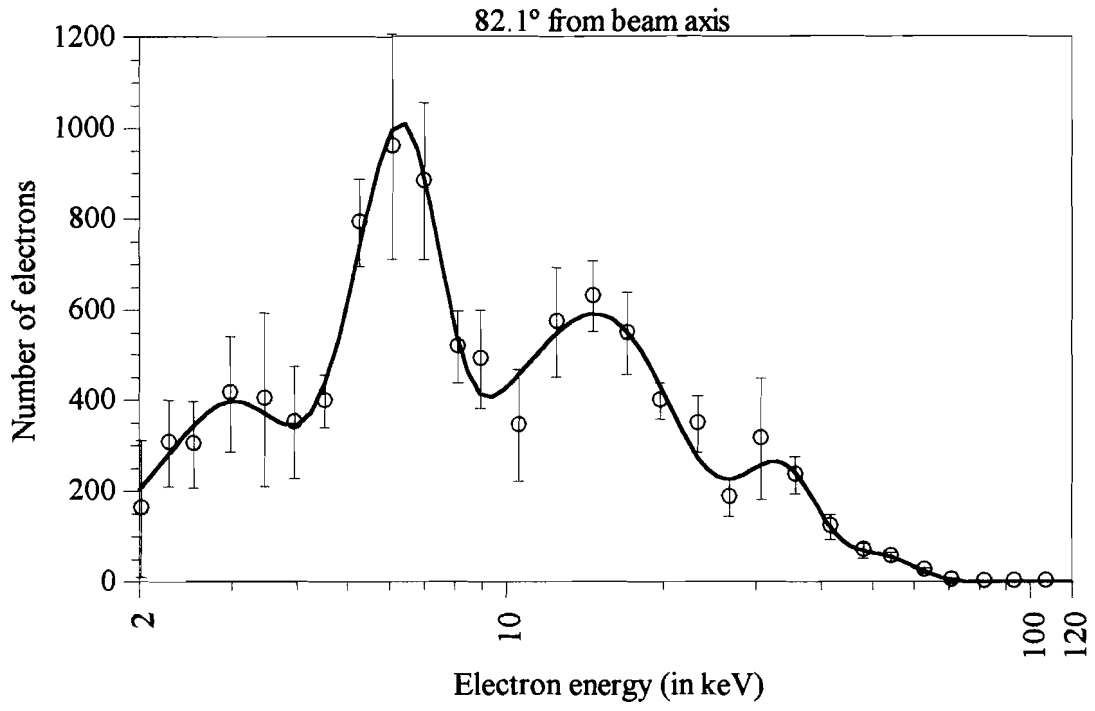
```

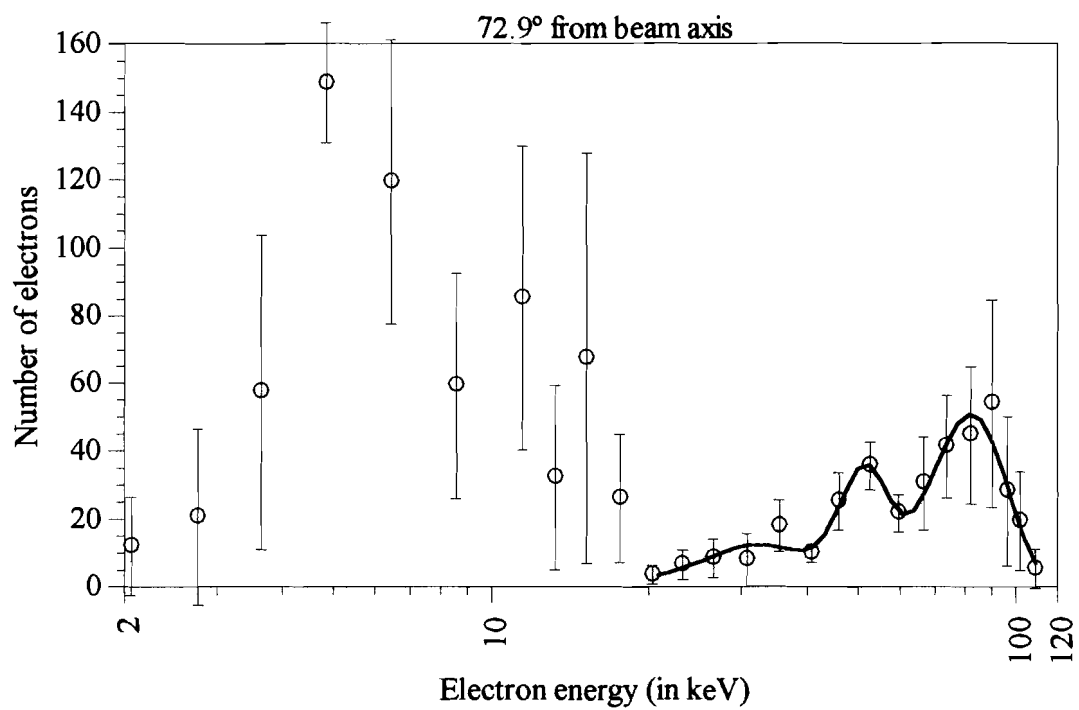
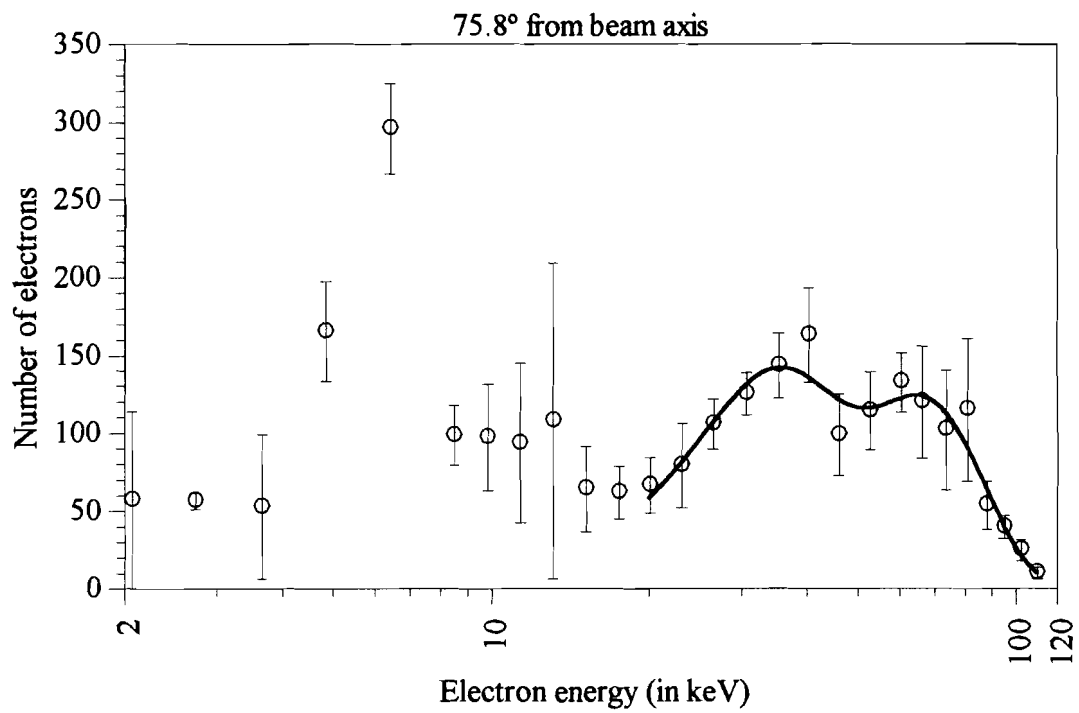
Appendix D
Energy spectra of Neon as a function of the angle from k

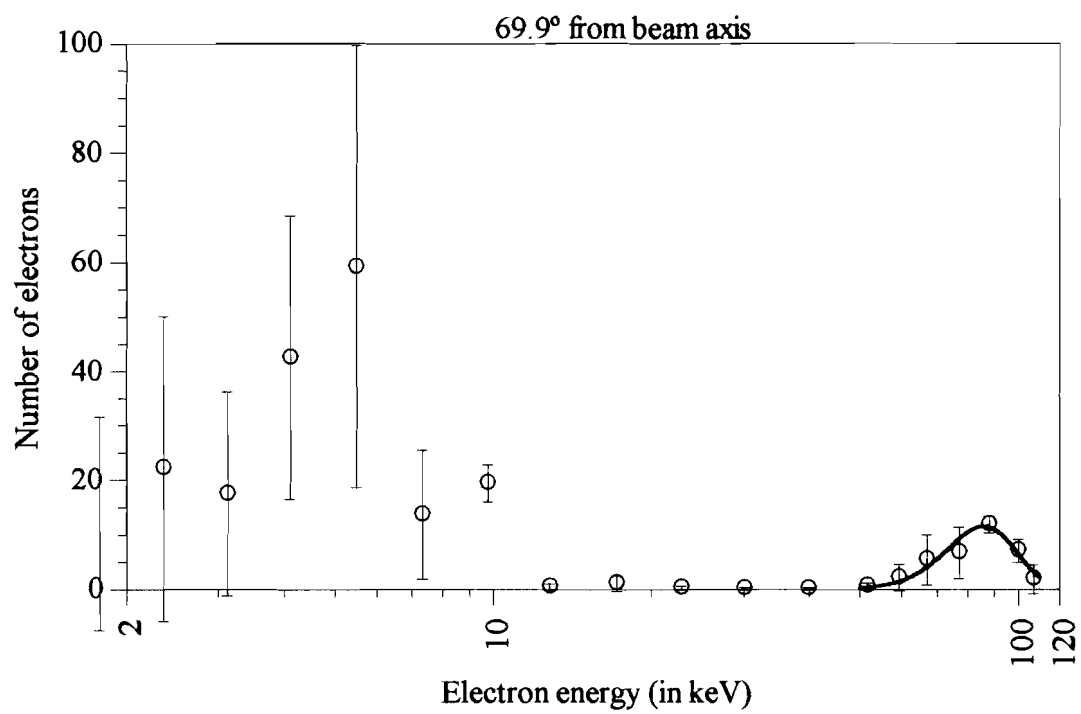
These spectra were generated via the methods described in section 6.2. Each point is an average of five shots after the electron number has been calculated from equation (5.2.8) and normalized by multiplying by $(I_{\text{norm}}/I_0)^{1.8}$ where $I_{\text{norm}}=10^{18}$ W/cm² and I_0 was the peak intensity of the laser shot.











Appendix E

Angular distributions of electrons from Neon relative to the laser beam axis

These angular distributions were generated through the techniques of curve fitting to the energy spectra described in section 6.2. The solid lines on each plot are Gaussian curve fits to the experimental data points and the dashed lines are the expected ejection angle calculated with equation (3.3.3).

